Localised Corrosion Studies of FSW Al-Li Alloys.

Microstructure Effect

Vishant Garg

TU Delft

Localised Corrosion Studies of FSW Al-Li Alloys.

Microstructure Effect

by

Vishant Garg

to obtain the degree of

Master of Science - Vehicle Engineering

in Mechanical Engineering

at the Delft University of Technology.

Student number: 4742265.

Project duration: March 1, 2018 – March 27, 2020.

Supervised by: Prof. Dr. Y. Gonzalez-Garcia.
Dr. Emmanouela Michailidou.

Thesis committee:

Prof. Dr. Y. Gonzalez-Garcia,	TU Delft, Committee Chair.
Dr. ir. I. Apachitei,	TU Delft, External Examiner.
Joost Van Dam,	TU Delft.

TU Delft

Abstract

Al-Li alloys were introduced for the use in aerospace applications due to its many advantages over steel such as its low density, good thermal and electrical conductivity and corrosion resistance of these alloys. The current generation of Al-Li alloys were developed to replace the currently used AA2024 alloy in commercial airframes, military and space applications. Traditional joining methods cannot be used to join dissimilar aluminium alloys. Thus, friction stir welding (FSW) was used to join the 2 dissimilar Al-Li alloys - AA2099 T83 and AA2060 T8E30 alloys. FSW causes several changes in the microstructure due to the rotational movement of the tool which results in localised plastic deformation and a thermal cycle in the alloys. This leads to 4 distinct zones in the alloys - the stir zone, thermo-mechanically affected zone, heat affected zone, and the base metal. The differences in microstructure is suggested to cause a change in the mechanical properties and localised corrosion behaviour of the alloys.

In this work, the localised corrosion behaviour of the friction stir welded Al-Li alloys were investigated. The effect of FSW on the microstructure and corrosion behaviour was also studied. Microstructural characterisation was done for both the alloys and their respective weld zones. Coarse constituent particles were found in all weld zones with a decreasing trend in average size towards the weld centre. Strengthening precipitates such as the T_1 phase particles were observed on the grain boundaries of the alloys. This had a decreasing trend of distribution density towards the weld centre with virtually no precipitates in the SZ. In order to assess the corrosion performance potentiodynamic polarisation, open circuit potential, linear polarisation resistance, and immersion tests were deployed. Furthermore scanning electron microscopy with energy dispersive X-ray spectroscopy was used to evaluate the morphology and chemical composition of the of the corroded surface. It was found that for the BM and HAZ regions of both alloys, the attack occurred mainly on the grain boundaries which were sites for the T_1 particles. These particles were suggested to be the controlling factor of localised corrosion behaviour in these regions due to their high electrochemical behaviour, which also resulted in almost no passivity in these regions. A large attack site was also observed on the surface of the matrix which was the site of hydrogen evolution during initial immersion time periods. Pits were also formed on the sites of coarse intermetallic particles. For the SZ regions the dominating attack was due to the coarse particles in the matrix.

The effect of anodising the surface and sol-gel coating of the surface on the corrosion behaviour was determined in this project. It was found that the anodised layer did enhance the corrosion performance of the alloys. The SZ of the anodised sample was found to be most prone to corrosion compared to the anodised base metals. The sol-gel coating on the surface was also found to increase the corrosion resistance of the surface due to its self healing properties thus protecting the surface of the alloys.

Keywords: Aluminium-Lithium alloys; Corrosion; AA2060 T8E30; AA2099 T83; Anodising; Hydrogen evolution; Passivity; Intergranular attack; Friction stir welding; Immersion tests; Potentiodynamic polarisation; Linear polarisation resistance; Scanning electron microscopy; energy dispersive X-ray spectroscopy; Sol-gel coating

Acknowledgement

I would like to give my thanks to the university - T.U.Delft for giving me the opportunity to be educated in one of the finest institutions of the world. My sincerest thanks to my supervisor Yaiza Gonzalez-Garcia for her steady supervision and guidance throughout the duration of the project. I would like to extend my deepest gratitude to my daily supervisor, Emina Michailidou for her everlasting support and advice in the project as well as in daily life. I would also like to thank the technical staff Sander van Asperen and Agnieszka Kooijman for their support and guidance in the laboratories and to Joost Van Dam for taking over as my daily supervisor at a moment's notice.

I would also like to thank my friends, especially Vishrut, Arsel, Achin, and Yannick for their constant help and support during this entire time. Last but not least, I would like to thank my parents and my family for everything they have done for me to get me here and also for being there for me.

Vishant Garg
Delft, March 2020

Contents

List of Figures

List of Tables

Abbreviations & Symbols

AS	Advancing side
BM	Base Metal
E_{corr}	Corrosion potential
E_{pit}	Pitting potential
EDS	Electron Dispersive X-ray Spectroscopy
FSW	Friction Stir Welding
HAZ	Heat Affected Zone
HV	Hardness Vickers
I_{corr}	Corrosion current density
IGA	Intergranular attack
ISGA	Inter-subgranular attack
LPR	Linear Polarisation Resistance
LSV	Linear Sweep Voltametery
OCP	Open Circuit Potential
RS	Retreating Side
SEM	Scanning Electron Microscopy
SKP	Scanning Kelvin Probe
SZ	Stir Zone
TMAZ	Thermo-mechanically Affected Zone

1

Introduction

Aluminium alloys have been used in the aerospace industry since the 1920's, when they began to replace wood [1, 12]. These alloys also became popular amongst auto-manufacturers to produce several parts and the bodies of their vehicles. In the last few decades, the usage of these aluminium alloys has steadily increased and in high end vehicles it has replaced steel and iron by almost 90 %. The advantages of these alloys over traditional iron-based alloys are lightweight, corrosion resistance, and very good thermal and electrical conductivity [2, 13, 14]. These factors and the fact that some of these alloys can be formed in a soft condition and heat treated to a temper comparable to that of structural steel, make them a very desirable material for use [15]. One of the most widely used aluminium alloys in aircraft manufacturing is the AA2024 alloy. It is a high strength and lightweight aluminium alloy. However, the new third generation Al-Cu-Li alloys, such as the AA2099 T83 and AA2060 T8E30 alloys, are investigated as a possible candidate to replace the AA2024 alloy in aerospace structures, due to their highly desirable combination of mechanical properties [16].

The third generation of Al-Li alloys were developed for various applications such as military, space, and also for commercial airframes [17]. These alloys show improved mechanical properties such as strength-to-weight ratio as compared to the traditional 2xxx and 7xxx series [16, 18]. Al-Li alloys have 3 major advantages that make them desirable to the transportation industry [19]. Firstly, lithium is one of the the lightest metallic element with a very low density equal to 534 kg m^{-3}. Therefore, alloying aluminium with lithium (density 2700 kg m^{-3}) lowers the density of the resultant alloy. As a matter of fact, for each 1 wt% Li added to Al, the density is reduced by 3% or approximately 80 kg m^{-3}. Further, lithium is the only metal when added to aluminium, increases elastic modulus by almost 6% or approximately 3 GPa per 1% Li added [18, 20, 21]. Thus, they possess high specific modulus and high specific strength. Finally, these alloys can be fabricated using existing production facilities since their behaviour during extrusion, forging, machining, and forming is very similar to that of conventional aluminium alloys. Despite these advantages, it is reported that these alloys are still susceptible to localised forms of corrosion, which is associated with the high reactivity of Li and the resultant Li-containing intermetallic phases [22].

The intermetallic particles in the aluminium alloy play a very important role with respect to material properties as well as corrosion behaviour of the alloy. A major strengthening precipitate is the T_1 (Al_2CuLi) phase. This T_1 precipitate nucleates on matrix dislocations and sub-grain boundaries [2, 23, 24]. Other such precipitates that may be found in these alloys are T_2 (Al_6CuLi_3), δ' (Al_3Li), S (Al_2CuMg), and other constituents depending on the alloying components and heat treatment received [20]. The T_1 phase is the most dominant one in the parent metal of the 3rd generation Al-Li alloys. It is also the phase of interest in terms of strengthening and corrosion resistance of these alloys [6, 23]. The formation of these precipitates has a detrimental effect on the corrosion resistance of the alloys, due to galvanic coupling between the aluminium matrix and these precipitates. Additionally, aluminium alloys are more likely to undergo localised corrosion, such as pitting and severe localised corrosion (SLC), as a result of defects on the passive protective film occurring near the secondary phase particles [25, 26].

During friction stir welding (FSW), the alloys undergo heavy plastic deformation, heat cycles, and recrystallisation. This causes numerous changes in the microstructure such as grain size and texture, composition of precipitates, added impurities, and redistribution of alloying elements. This leads to 4 characteristic zones in the weld sample - the stir zone (SZ), the thermo-mechanically affected zone (TMAZ), the heat affected zone (HAZ), and the base metal (BM) [27]. The metallurgical variations between the various zones in the friction welded joint can cause preferential corrosion susceptibilities and promote galvanically enhanced dissolution of the most active regions [3]. Reports in literature indicate that the corrosion susceptibilities of friction stir weldments of Al alloys are unpredictable [3]. A small change in temper conditions and/or welding parameters can significantly change the corrosion behaviour as well as the corrosion susceptibility of that alloy [28, 29]. This is why it is important to study the electrochemical behaviour of these zones and thus determine the localised corrosion behaviour of the welded alloys.

The most common form of corrosion attack in these aluminium alloys is pitting. This occurs in the presence of aggressive chloride ions [6, 25]. The other type of attack found in these alloys is called severe localised corrosion (SLC) and it was characterised by hydrogen gas evolution and corrosion rings around the attacked areas [13, 30]. The origin of SLC is related to the selective dissolution of the T_1 phase [24]. However, the type of attack on each alloy is different due to the difference in microstructures of each alloy and various precipitates found in them depending on the alloying elements. The exact nature of the attack is also not well defined in most literature. Although they have narrowed it down and proposed a few methods of the corrosive attack due to the strengthening and intermetallic phases, there is still a lot to be studied and to determine the exact process of the corrosion attack on Al-Li alloys.

1.1. Scope of the project

Since the Al-Li alloys were developed for aerospace applications, the localised corrosion behaviour of the alloy weld regions must be determined to find out whether they are suitable candidates for the replacement of the AA2024 alloy. Therefore, the main focus of this project is to investigate the changes caused in the microstructure of the AA2099 T83 and AA2060 T8E30 alloys due to joining by friction stir welding and how this affects the localised corrosion behaviour of the alloys. The types of corrosion attack on the weld zones and their mechanisms need to be evaluated. Lastly, the efficiency of protection methods such anodising and sol-gel coating on the corrosion behaviour of the alloys is to be studied.

1.2. Research Questions and Objectives

The main objectives of this research is to determine the localised corrosion behaviour of the FSW Al-Li alloys and the effect of anodising and sol-gel coating on the surface. To fulfil this, the following questions need to be answered:

- How does the friction stir welding process change the microstructural characteristics of the alloy?
- How does the change in microstructure at the various weld zones affect the electrochemical behaviour and kinetics of corrosion?
- What is the role of the intermetallic particles on the corrosion behaviour of the alloys?
- What are the types of corrosion attacks observed in the alloys weld regions?
- Does anodising of the surface enhance the corrosion protection for the alloys?
- Does the sol-gel coating on the surface increase the resistivity to corrosive attack?

This project has been divided into 2 parts based on the goals of the research. Part A, which includes chapters 4, 5, and 6, deals with the effect of FSW on the microstructure and localised corrosion behaviour of the alloys. Here, microstructure characterization of the weld zones were done on the as-received sample to investigate the differences between the weld zones in terms of average grain size,

grain morphology, the intermetallic particles found, and the average size and distribution of the intermetallic particles. Next, electrochemical tests were carried out to determine and quantify the kinetics of corrosion of each weld zone such as the passivity, pitting corrosion, nobility, and the rate of corrosion for the weld zones of the alloys. This was followed by in-situ immersion tests of these zones to show the localised corrosion behaviour and the microstructural features that control the corrosion behaviour of these alloys. Part B, which includes chapter 7, deals with the effect of anodising the surface and sol-gel coating applied on the surface on the localised corrosion behaviour of the alloy. Anodising and sol-gel coating on the surface of the sample were tested to determine whether they are effective in protecting the alloys from corrosion attacks and how effective they are in doing so as compared to the bare alloys.

2

Literature Review

Aluminium-Lithium alloys are described as the future of the aerospace industry. However,the lack of understanding provided by existing literature regarding the corrosion behaviour of AA2099 and AA2060 is one of the main challenges in making these alloys industrially applicable. To counter this roadblock, aluminium alloys of similar alloying elements, microstructures, and other features were studied to give an impression of these alloys. Most of these alloys were from the 2xxx series of Aluminium alloys, which have a major alloying element of Cu in them. Some of them include - AA2219, AA2198, AA2020, AA2050, and AA2024 alloys.

However, the corrosion attack on each alloy is different due to the difference in microstructures of each alloy and various precipitates found in them depending on the alloying elements. The exact nature of the attack is also not well defined in most literature. Although they have narrowed it down and proposed a few methods of the corrosive attack due to the strengthening and intermetallic phases, there is still a lot to be studied and to determine the exact process of the corrosion attack on Al-Li alloys.

Friction stir welding (FSW) is a recent and innovative solid state welding technique. It produces high integrity joints in difficult to weld materials such as aluminium, copper and magnesium. Since its invention, many manufacturers have adopted this method for producing lightweight structures where high strength, low weight, good toughness, and excellent fatigue life are required [31]. The friction stir welded alloy undergoes heavy plastic deformation, heat cycles, and recrystallisation. This causes numerous changes in the microstructure such as grain size and texture, composition of precipitates, added impurities, and redistribution of alloying elements. This leads to the formation of zones in the alloy depending on the deformation and thermal cycle undergone by that region. The metallurgical variations between the various zones in the friction welded joint can cause preferential corrosion susceptibilities and promote galvanically enhanced dissolution of the most active regions [3].

It was reported that the corrosion susceptibilities of friction stir weldments of Al alloys are unpredictable. A small change in temper conditions and/or welding parameters can significantly change the corrosion behaviour as well as the corrosion susceptibility of that alloy [28, 29]. The tool pin profile used in FSW strongly influences the change of microstructure in various zones of the weld. Hence, the tool pin profile also plays a very important role in the corrosion behaviour of a friction stir welded alloy [32].

In this chapter, the microstructure and corrosion behaviour of various Al-Li alloys are investigated to give an overview of what could be expected for the localised corrosion behaviour of friction stir welded AA2099 and AA2060 alloys. The various factors influencing the corrosion behaviour of the welded alloys have been also been studied to give an idea about the performance of the same.

2.1. Aluminium Alloys - Microstructure and Corrosion Behaviour

The first generation of the Al-Li alloys were introduced in 1958 with the first commercial alloy AA2020. This was withdrawn in the 1960's over concerns of its fracture toughness. The gas crisis in the 1970's and the potential threat of replacement of aluminium alloys by carbon fibre composites led to the development and research of the 2nd generation Al-Li alloys. This was to be the solution for a lightweight and cost effective material for the industry. However, these alloys weren't successful due to unacceptable degrees of property anisotropy, low short transverse properties, and thermal instability [1].

The 3rd generation Al-Li alloys were developed in the 80's and 90's. These alloys have a lithium content of less than 2% in them. They have overcome the major shortcomings of the previous generations and show improved mechanical and physical properties relative to the traditional 2xxx alloy series [1, 21]. A few of these 3rd generation alloys have been described below (Figure 2.1).

Alloy	Li	Cu	Mg	Ag	Zr	Mn	Zn
2195	1.0	4.0	0.4	0.4	0.11		
2196	1.75	2.9	0.5	0.4	0.11	0.35 max	0.35 max
2297	1.4	2.8	0.25 max		0.11	0.3	0.5 max
2397	1,4	2.8	0.25 max		0.11	0.3	0.10
2198	1.0	3.2	0.5	0.4	0.11	0.5 max	0.35 max
2099	1.8	2.7	0.3		0.09	0.3	0.7
2199	1.6	2.6	0.2		0.09	0.3	0.6
2050	1.0	3.6	0.4	0.4	0.11	0.35	0.25 max
2060	0.75	3.95	0.85	0.25	0.11	0.3	0.4
2055	1.15	3.7	0.4	0.4	0.11	0.3	0.5

Figure 2.1: Chemical Composition of 3rd - Generation Al-Li Alloys (wt%) [1]

2.1.1. AA2099

The AA2099 alloy, also known as the (AF/C 458), is one of the new 3rd generation Al-Li-Cu alloys that was introduced first in 2003 [33]. This alloy has been found to save up to 14% weight on major structural components of the aircraft wings. The AA2099 alloy has also been found to have a higher transverse ductility, excellent stress corrosion cracking resistance, and excellent toughness as compared to its predecessor in the 2nd generation, the AA2090 alloy [17]. The alloy has found widespread use in the aircraft industry since they can be commonly produced by extrusion with T8 as the final heat treatment temper [34].

2.1.2. AA2060

The AA2060 alloy is a relatively new Al-Li-Cu alloy introduced in 2011 by Alcoa Inc. [33].This alloy is said to provide exceptional mechanical properties such as low density, high stiffness, and high strength-to-weight ratio and therefore it has been developed for aerospace applications such as the fuselage panels, and upper and lower wing structures of jetliners [18, 35, 36]. The alloy in T8 temper provides significant gains in both strength and toughness due to the nucleation and growth of intermetallic hardening precipitates in the Al matrix.[1, 35].

Other alloys of the 3rd generation are AA2198, AA2050, AA2199, AA2195, and a few others. Most of these alloys have been developed for various components in an aircraft. The 2195 alloy has been used on the super lightweight tank of the Space Shuttle that was first flown in 1998 [1].

2.1.3. Microstructural Features

A key aspect of the microstructure is the intermetallic particles. The intermetallic particles in aluminium alloys can be divided into 3 main types:[37]

1. Coarse constituent and impurity particles (> 0.5 μm)
2. Dispersoids (100 - 500 nm)
3. Hardening precipitates (< 200 nm)

The intermetallic particles, hardening precipitates, and dispersoids present in the microstructure of Al-Li alloys have a detrimental effect on the corrosion behaviour of the alloy, as mentioned earlier. Hence, it is important to study these phases in the alloy and how they contribute to the corrosion of the alloys.

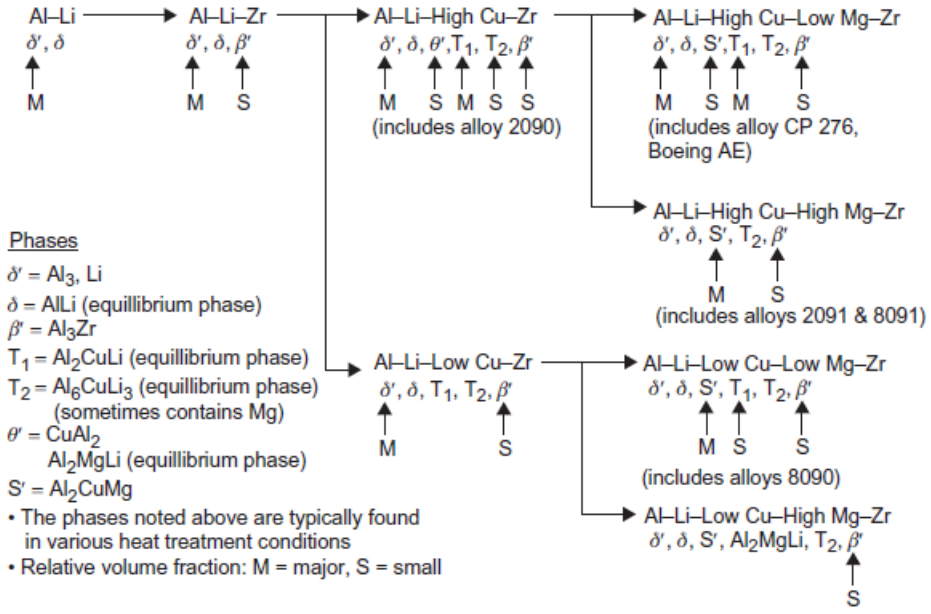

Figure 2.2: Schematic of the precipitate phases that form in Al-Li alloys [1]

Dispersoids

Dispersoids are nano to micron range sized second particles comprising elements that are highly insoluble in aluminium. These particles have a significant effect on recrystallisation, grain growth, and grain size control, which is why they are homogeneously dispersed in the alloy. The most common dispersoid formers are Cr, Ti, Zr, and Mn which are generally passive in the environments where Al is used, with the exception of Mn. There are basically 3 types of dispersoids present in aluminium alloys depending on the alloying elements: Al_6Mn, $Al_{20}Cu_2Mn_3$, and Al_3Zr particles [18, 38].

Y. Ma et al. [39] studied the distribution of intermetallics in AA2099 aluminium alloy extrusion. With the help of Transmission electron micrograph, they observed that rectangular or spherical dispersoids were randomly distributed within the alloy matrix. The rectangular and spherical shapes corresponded to long and short transverse faces of a rod-like shape. An EDS analysis was used to determine the elements in these dispersoids which found that these rectangular and spherical dispersoids contain Al, Mn, and Cu in them.

It is known that lithium is undetectable by EDS, thus they used EELS to determine whether these dispersoids contained lithium in them or not. The dispersoids were revealed as bright regions in the EELS map of lithium, thus confirming the presence of Li in them and also suggesting that they were rich

in Li. The dispersoids were found to be Al-Cu-Mn-Li intermetallics. An EDS scan of the light spheres in the microstructure of AA2099 also confirmed the presence of Zr in them. This suggested that the β' (Al_3Zr) phase was present in this alloy. This phase is the primary phase that pins the high angle grain boundaries and is therefore important in controlling and restricting recrystallisation and subsequent grain growth [1].

Coarse Constituent and Impurity Particles
Constituent particles are comparatively large and irregularly shaped (0.5 μm - 10 μm). These particles can be formed during alloy solidification and are not dissolved during subsequent thermo-mechanical processing. Processing mechanisms such as rolling and extrusion tend to break up and align these particles into bands within the alloy. Since these particles are rich in alloying elements , their electrochemical behaviour and hence corrosion behaviour is significantly different than that of the surrounding aluminium matrix. The most commonly found elements in the constituent particles are generally Cu, Fe, Si, Mg, and Mn. In high strength Al alloys, pitting occurs partly due to some fraction of the constituent particles present in the alloy [38]. Donatus et al.[23] found that constituent particles, with regard to corrosion, cause trenching of the surrounding aluminium matrix leading to observable cavities on the surface of the alloy.

The intermetallic particles in the AA2099 alloy were observed by performing SEM to generate a backscattered electron micrograph [39]. This revealed the particles were aligned to the extrusion direction. EDS analysis of the particles revealed that these particles contained Al, Fe, Mn, and Cu. However, the Cu concentration varies in these particles from 2.9 - 3.1 wt.%. The high-Cu-containing phase is located in the central region and low-Cu-containing phase in the peripheral region.

Campestrini et al. [40] had observed similar results in AA2024 alloy with intermetallic phases of different concentrations and also located in the central and periphery regions. Y. Ma. et al. [39] suggested that the copper atoms from the high Cu phase migrated to the low Cu phase by diffusion. The high Cu phase was formed during casting and the low Cu phase formed subsequently due to diffusion. These different types of constituent particles were dependent on the conditions of heat treatment and thermomechanical processing. This inhomogeneity of the intermetallic particles may cause a highly localised galvanic coupling between them and thus result in localised corrosion.

Precipitates
Precipitates are generally nanometers sized particles. They can be spherical shaped, needle-shaped, plates, and various other shapes depending on the elements found in the particles itself. They are formed by nucleation and growth from a supersaturated solid solution during natural or artificial ageing. When they are homogeneously dispersed, their effect on localised corrosion behaviour is difficult to evaluate. However, when they are concentrated on grain boundaries and sub-boundaries, they may affect intergranular corrosion (IGA) and stress corrosion cracking (SCC) susceptibility [38, 41].

As mentioned earlier, there are a number of hardening precipitates found in Al alloys such as T_1 (Al_2CuLi), T_2 (Al_6CuLi_3), δ' (Al_3Li), and θ' (Al_2Cu) phases [1, 42]. These can be present depending on the alloy composition and ageing conditions of that alloy. The precipitates play an important role in the mechanical behaviour of the alloy such as hardness, elasticity, and corrosion susceptibility.

The T_1 phase, needle like shaped, is the major strengthening phase of the third generation Al-Li alloys [20, 23]. T_1 nucleates on matrix dislocations and low-angle subgrain boundaries. Subgrain boundary precipitation can be heavy in unstretched alloys. However, stretching before heat treatment introduces dislocations which serve as additional nucleation sites for T_1 phase away from the boundaries and within the subgrains. Stretching allows a homogeneous distribution of the T_1 phase within the alloy. This in-turn has quite a beneficial effect on the strength, ductility, and toughness of the alloy [18]. The T_2 (Al_6CuLi_3) phase is typically found on high-angle grain boundaries after over-ageing.

The Metastable δ' (Al_3Li) phase is present only in slight quantities under normal ageing conditions [20]. This phase leads to an increased strength, however it has an negative effect on the corrosion

resistance of the alloy. Although it is generally homogeneously distributed in the matrix, it is not usually found in alloys containing Li less than 1.3%[43, 44]. The θ' (Al_2Cu) phase is the major strengthening phase in the first generation Al-Li alloys.

The T_1 phase is the phase of highest metallurgical interest in the new generation Al-Li alloys. It dictates the strength level of the alloy and also the localised corrosion resistance of the alloy [23]. According to Y. Ma et al. [39], needle-like precipitates were observed in the AA2099 alloy. Dark shadows were revealed around these precipitates, suggesting the presence of a strain field. The EELS mapping of Cu and Li revealed that these elements were in abundance and that the needle-like precipitates observed were in fact the T_1 phase precipitates. Although the T_1 phase is very beneficial for the mechanical properties of the Al-Cu-Li alloys, the effect it has on corrosion behaviour of the alloy is still controversial.

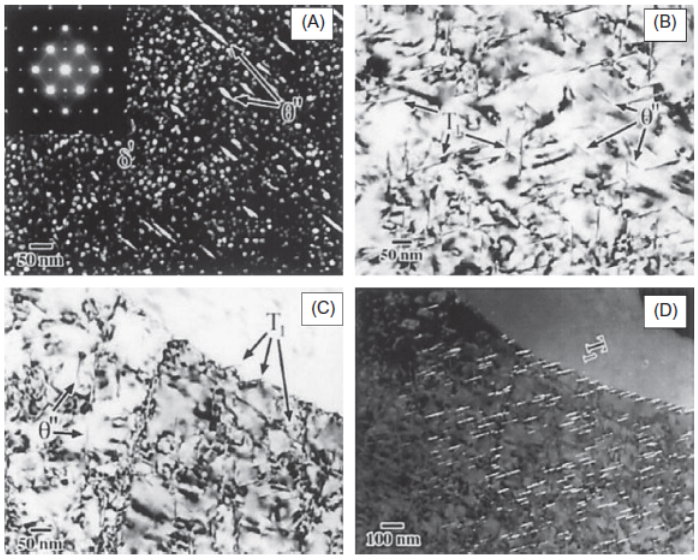

Figure 2.3: TEM micrographs of the hardening precipitates found in the Al-Cu-Li alloys (A) δ', (B) θ', (C and D)T_1 precipitates. [1]

2.2. Corrosion

2.2.1. Corrosion on base metal

Recent reports in literature have indicated that the Al-Cu-Li alloys are highly susceptible to localized corrosion. This is mainly characterised by selective attack or dissolution of certain grains and grain boundaries. However, the exact nature of the attack has not been confirmed despite a number of theories put forward by various researchers, as will be seen in this section. Therefore, it is important to evaluate and conclude the findings on the corrosion behaviour of these alloys.

The most common form of corrosive attack on Al alloys is said to be pitting [25]. However, pitting initiation and growth can occur due to various factors and reasons. One of the main reasons for the corrosive attack is claimed to be the T_1 phase in these alloys [2, 20, 24, 30, 34, 45]. The other type of localised corrosion found in these alloys is called severe localised corrosion (SLC). This type of corrosive attack is characterised by hydrogen (H_2) gas evolution and corrosion product rings around the attacked areas [30].

There have also been reports on intergranular attack (IGA) and inter-subgranular attack(ISGA) on these aluminium alloys due to electrochemically active precipitates nucleating on the grain and subgrain boundaries [12, 20]. However, it is still not clear why this attack is localised within certain areas and why certain grains are more susceptible to this type of corrosion compared to other grains.

2.2.2. Mechanisms of Corrosion Attack

Pitting

Evidence in the literature suggests that the constituent particles which contain aluminium, iron, copper, and manganese had caused pitting in the AA2099 alloy. This attack was also related to the distribution of these constituent particles in the alloy [30]. These intermetallics are said to be the initiation sites for pitting in Al-Li alloys. The particles are cathodic with respect to the aluminium matrix and promote the dissolution of the matrix. Thus, the corrosion attack occurred at the matrix surrounding these particles [32].

Severe Localised Corrosion

Y. Ma et al. [24] suggested that the origin of SLC in AA2099 alloy is related to the selective dissolution of the T_1 phase. The T_1 phase precipitates at the grain and subgrain boundaries and also dislocations within the grains which had undergone plastic deformation during forming processes. Due to high electrochemical activity of this phase, corrosion attack occurred preferentially in the more deformed grains. At the beginning of immersion in chloride environment, the T_1 phase is anodic to the alloy base, resulting in its anodic dissolution and corrosion. During this process, Li is dissolved and Cu enriches on its surface layer. This makes the potential of the T_1 phase move to a positive direction with immersion time. The corroded T_1 phase then becomes cathodic to the base metal, leading to the anodic dissolution and corrosion of the alloy base at the regions close to the precipitates [45].

Boundary Attack

Aluminium alloys are susceptible to 2 forms of boundary attack. The first type is the intergranular attack (IGA) which is the preferential dissolution of grain boundaries. The other type is inter-subgranular attack (ISGA). This is the preferential dissolution of subgrain boundaries. Theories for the mechanism of these types of attack have been put forward by various researchers [20, 46]. Two basic mechanisms are given below:

- Selective dissolution of active precipitates concentrated on boundaries.
- Selective dissolution of a precipitate free zone

A selective T_1 dissolution mechanism for IGA for AA2020 proposed that since the T_1 phase contained large amounts of lithium, it was more active than the matrix. Thus, galvanic cells formed once it was exposed to an aqueous solution. This resulted in large anodic current densities along the boundaries where the phase had precipitated, causing preferential boundary attack [47]. Therefore, in the AA2090 alloy, it is expected that the T_1 phase would be susceptible to preferential dissolution under free corrosion conditions.

Kumai et al.[46] suggested that the IGA in AA2090 was associated with the dissolution of Cu-depleted zones that formed adjacent to grain and subgrain boundaries due to precipitation of Cu rich phases.

2.2.3. Factors influencing the Corrosion Behaviour

Effect of Grain Orientation

Y. ma et al. [24], who studied the role of grain orientation on localised corrosion of AA2099, observed during immersion tests that not all grains corroded while exposed to similar corrosion conditions. Selective attack of grain boundaries and grain interiors was observed on the cross section of the specimen tens of micrometers beneath the exposed surface. Hence, they suggested that the selectively corroded grains were intrinsically different from other grains.

When the AA2099 alloy was cold stretched along the direction of extrusion, all grains were plastically deformed. However, the grains below the top surface experienced more plastic deformation than those at the top and the bottom faces. In doing so, there was an increase of dislocations in the grains and thus more subgrain boundaries/dislocations walls were formed. During artificial ageing T_1 phase

nucleated on the grain and subgrain boundaries and dislocations within grain interiors. This resulted in a heterogeneous distribution of the T_1 phase.

Once the sample was exposed to corrosive environment, localised corrosion preferentially developed in the more deformed grains. As this happens, galvanic coupling occurs between the excessive deformed grains and the deformed grains, which causes corrosion to mainly occur on the excessive deformed grains. Thereafter, localised corrosion propagated from these grains along the grain boundaries and dislocations.

Effect of Grain Size

The effect of grain size on the corrosion behaviour of aluminium alloys remains controversial. Most studies that relate grain size to corrosion suggest that as grain size decreases, the corrosion resistance of the alloy increase. This happens as the finer grains are more effective in forming a passive oxide layer for the aluminium alloy [48, 49].

Vincent Proton et al. [50] reported that the fine grained aluminium alloys were found to be less corrosion resistant than the coarse grained alloys. They suggested that the finer grains resulted in increased grain and subgrain boundaries where the T_1 phase nucleated. Since the T_1 phase is electrochemically more active than the base metal, it resulted in intergranular corrosion attack on the alloy.

Due to the contradiction in literature, the effect of grain size on corrosion cannot be confirmed. Moreover this effect is highly dependent on the alloy composition, its heat treatment, and the intermetallics found in the alloy.

2.3. Friction Stir Welded Al-Li Alloys

Friction Stir Welding (FSW) was invented by Wayne Thomas at TWI in 1991. It is one of the most promising methods for joining of lightweight metals due to its metallurgical advantages compared to the other conventional fusion welding methods [27]. This technique involves a non-consumable tool fitted with a specially designed pin and shoulder. This tool rotates at very high speeds, plunging into adjacent edges of the metal pieces in which a suitable weld joint forms between the work pieces.

2.3.1. Friction Stir Welding Process

In FSW, the welding starts by bringing the work pieces into contact and proceeds with the frictional heating of the rotating tool which is pressed at their interface causing local plastic deformation. As the tool moves forward along the joint line, it stirs and forges the material from its front face to its trailing face where it finally cools down and turns into a solid state weld joint [2].

Tool Pin

The tool used in FSW has 2 distinct parts, the shoulder and the pin. It is designed to serve 3 main functions [5]:

1. Generate the frictional heat that softens, without melting, the work material around the pin.
2. Control the material flow to produce a defect-free weld.
3. Confine the hot material below the shoulder.

The shoulder is responsible for generating heat and containing the plasticised material in the weld zone, while the pin mixes the softened material of the components which then forms a joint [51]. The tool pin profile greatly affects the material flow behaviour, which in-turn causes change in microstructure of the welded joint. Cylindrical and plain tapered tool pins do not always give the best of welds. They cause ineffective mixing of the weld zone and can lead to wormholes at the base of the weld. Tools which are tapered and have threads can lead to flaw free welds. These tools have a larger surface

area which causes more frictional heat and they also exert a downward force which improves the flow of the softer material. The pin angle too plays an important role in the welded joint. The wider the angle between the conical surface of the pin and its axis, a more uniform temperature distribution is achieved [31].

Thus, the microstructure of the welded zone greatly depends on the tool pin profile and angle, and can be used to achieve the desired weld by modulating these parameters or by choosing the correct tool pin for the joining process.

Zones of FSW

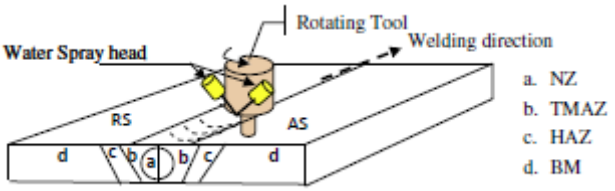

Figure 2.4: Schematic diagram of the FSW experimental set-up and the various zones formed in the material [2].

As mentioned earlier, generally four distinct zones appear in FSW aluminium alloys, as seen in Figure 2.4, and each of them has certain characteristics. These zones are:

1. Stir zone (SZ)
2. Heat-affected zone (HAZ)
3. Thermo-mechanically affected zone (TMAZ)
4. Base material (BM)

The stir zone, or the weld nugget, is formed due to recrystallisation caused by severe plastic deformation. It is the region that roughly corresponds to the path of the pin during welding. The grain size of the material in this zone is very small compared to that of the base metal. The microstructure of this zone has constituents of both the metals involved in the welding process. A feature of this zone is the occurrence of several concentric rings which has been called ”onion-ring stucture”.

The TMAZ can be found on both sides of the stir zone. It is created by plastic deformation of the base metals during the welding process. Here, the strain and temperature are lower than the SZ and thus the effect of welding on the microstructure is comparatively less. The microstructure of the TMAZ is unmistakeably of its parent metal, even though it is deformed and rotated, unlike that of the SZ.

The HAZ is formed due to weld thermal cycle in all welding processes. This region is subjected to a thermal cycle but it undergoes no plastic deformation. The temperatures are lower here than the TMAZ but they have a huge effect on the microstructure and thus the mechanical properties and electrochemical behaviour of the zone [31].

The Base metal is the area of the material that has not been affected by the welding process at all. The microstructure and mechanical properties of this zone remains the same.

Why FSW?

The FSW process is widely used in various industries today even though it is a relatively new process. Some of them include shipbuilding, aviation, power generation, and defence industries. It is also used for making critical components of structures in these industries such as wings and fuselages of aircrafts, fuel tanks for spacecrafts, and engine and chassis cradles in vehicles due to excellent mechanical properties obtained by this process.

All the applications of friction stir welded components stated above is possible due to numerous advantages it has over traditional fusion welding methods. They are as follows:[31, 52]

- It is energy efficient and environment friendly.
- It can be used to join metals that are not possible with conventional welding methods.
- It can also be used to join dissimilar metals together.
- Problems such as liquation, cracking, porosity, and spatter do not arise in the weld.
- No filler metal required here.
- No arc or fumes due to FSW.
- Low distortion and shrinkage of the weld.
- It can be operated in all positions.
- The process is suitable for underwater welding.
- It is suitable for automation and can be adaptable for robotic use.
- Excellent mechanical properties are achieved in fatigue, tensile, and bending tests.

Although FSW claims defect free welds of high strength, there are certain flows associated with the friction stir processing. The most common flaws include voids, lack of penetration, joint line remnants, and surface flash. The key parameters that must be controlled to avoid these flaws are tool geometry, tool rotation and transverse speed, tool plunge depth, and tool pressure [53].

2.3.2. Microstructure of Welded Zones

When the Al-Li alloys are welded together by FSW, a number of microstructural changes occur in the materials. These changes are different in every zone of the welded alloy. Factors such as heat, plastic deformation of the grains,and tool pin profile affect the welded zones in a significant manner.

As FSW occurs, each rotation of the tool results in the extrusion of semi-cylindrical layers of the material. These layers cool down faster than each subsequent layer formed. This results in a structure which is known as ”Onion Rings” in the direction of the weld. This phenomenon was also reported for AA2219 and AA2050 alloys [5, 50].

During FSW, namely 4 zones are observed in the joint. They are SZ, HAZ, TMAZ, and BM, as mentioned earlier. These zones are not always well defined but can be estimated by the distance from the centre of the joint. The stir zone, which is formed where the tool penetrates the joint, shows an asymmetrical basin shape with fine grain structure and dense dislocations. This is seen in Figure 2.5.

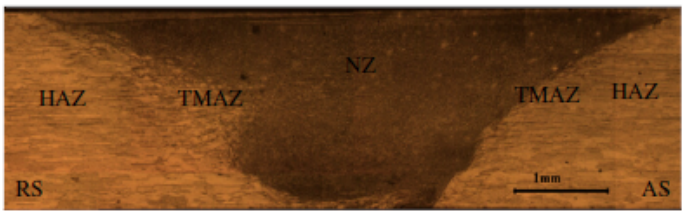

Figure 2.5: Optical image of the cross-section of friction stir welded AA2060 alloy [2].

B. Cai et al. [2] studied the microstructure of friction stir weld of the AA2060 alloy. The base metal consisted of pancaked grain structure, thin and elongated along the rolling direction. This does not change due to welding as the base metal is not affected by either heat or by deformation due to the tool during the welding process. The HAZ showed similar grain morphology to the base metal. It is distinguished from the base metal by observing how the grain size and shape alter between the HAZ and BM. However, fine recrystallised grains were observed in the stir zone. The recrystallisation was

due to friction stir heating and severe plastic flow during welding. This behaviour was observed by other researchers as well [54, 55]. The grains inside TMAZ were distorted by the strain induced by severe stirring motion of the tool. These grains were also fine compared to that of the HAZ or the BM.

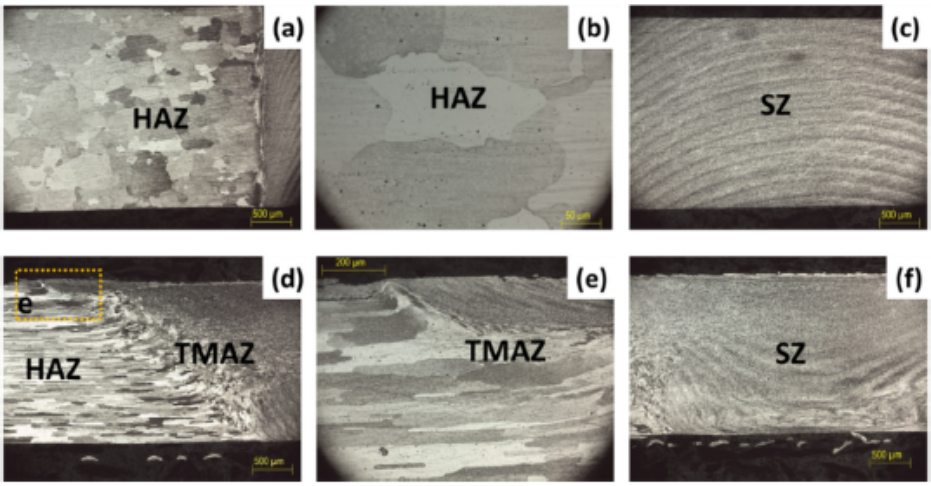

Figure 2.6: Optical Micrographs of the surface and cross-section of AA2198 friction stir weldment [3]

A. Fattah-alhosseini et al. [4], who studied the effect on microstructure and corrosion behaviour of the nugget zone in dissimilar FSW AA5083 and AA1050, reported similar findings of the microstructure. They observed that the stir zone showed very fine recrystallisation on both sides. Here, the AA5083 was positioned on the advancing side (AS) and the AA1050 alloy was placed on the retreating side (RS) to obtain a stronger joint. They also observed that the shape of the weld was basin shaped in the stir zone, which extended from the bottom to the top surface of the sheet (Figure 2.7). This occurred due to the friction which was produced by the shoulder of the tool and the top surface of the base metals during the process.

The basin shape of the weld was much more irregular here, as compared to the welding of similar alloys. This is observed in Figure 2.7. The irregular shape was due to the alloys have different concentrating alloys and microstructural properties. This allows us to identify the zones of the FSW joint easily.

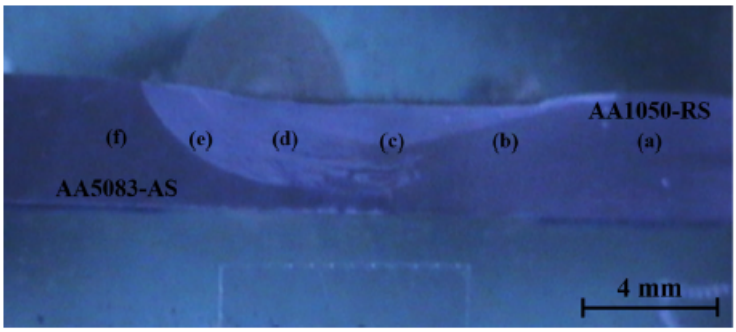

Figure 2.7: Cross section of the dissimilar FSW joint of AA1050 and AA5083 [4]

Another feature observed from Figure 2.7 is the difference of the weld joint in the advancing and retreating side. This can be explained by the material flow due to the tool pin during the process. As it is known, when the tool pin rotates, localised plastic deformation occurs which softens the material. Ch. Venkata Rao et al. [32] mentioned that one of the important characteristics of FSW is the different relative speeds of plastic material on AS and RS. However, this causes an irregular temperature distribution, as the temperature in the advancing side is more than that of the retreating side as explained

by P. Cavaliere et al. [54]. Since the temperature is higher on the AS, a larger region undergoes recrystallisation and forms finer grains whereas this area in the RS is smaller. This is also the reason why the TMAZ/SZ interface on the AS is sharper than that on the RS. The material flow during FSW also plays an important role in the microstructure and shape of the welded joint.

Dispersiods that were aligned along the rolling direction in the base metal were stirred and distributed uniformly in the stir zone. The serious stirring deformation causes the flow of material and redistribution of particles and possibly breaks off large dispersions [2]. These dispersiods settle on grain boundaries and prevent grain growth during FSW process due to elements like Zr which are used as grain refiners.

The distribution of coarse particles is same in the BM and the HAZ. The particles in the SZ and the TMAZ are mainly Cu-Fe rich intermetallic particles, as reported by Donatus et al. [6] for the AA2198 alloy. A few particles containing Si were also observed, which were fragmented and better distributed in the SZ. The intermetallic particles found are either pinned on the grain boundaries or located within fine grains. The hardening precipitates found in the base metal such as the primary T_1 phase or the secondary phases such as the δ', and the θ' phase are dissolved in the SZ and the TMAZ during the FSW process [2, 6]. The dissolution of strengthening precipitates occur due to the heat applied during the welding process and the recrystallisation of the grains in these zones.

Effect of Grain Size

The influence of FSW parameters on passivation properties of AA5052 were studied by Hariri et al. [51]. They reported that under optimum welding conditions, passivation of the FSW processed alloy improves. They have claimed that the fine grained structure of SZ in these FSW processed aluminium alloys facilitates the nucleations and growth of passive films.

Effect of Pin Geometry

Tool pin profile plays an important role in material flow and therefore it regulates the welding parameters of the FSW process. The contours that are observed in the weld are dependent on the tool design.

Ch. Venkata Rao et al. [32], who studied the effect of tool profile on microstructure of AA2219 weld, used a triangular and a conical tool profile to evaluate which of the 2 tools would result in a better weld and microstructural properties. They observed that the triangular tool pin resulted in very fine grain distribution as compared to the conical tool. In the weld made using triangular tool, the SZ and TMAZ) experienced higher temperatures and turbulent material flow resulting in severe plastic deformation. This caused very fine grains to form in the stir zone due to dynamic recrystallisation. They also mentioned that due to the higher temperatures produced by the triangular tool pin, there was a higher rate of dissolution of the hardening precipitates in the AA2219 alloy.

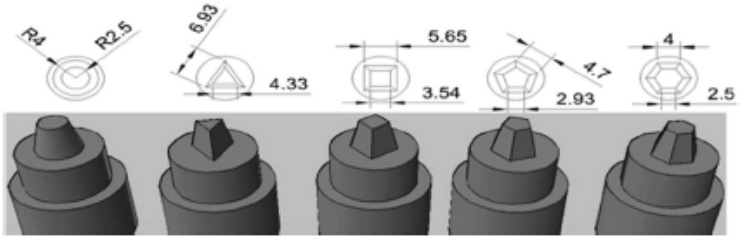

Figure 2.8: Geometry of various tool pin profiles [5]

G. Rambabu et al. [5], also reported similar findings regarding the tool pin profile. They tested 5 various types of tool pins to understand its effect on the welded joint. These tool pin profiles are given in Figure 2.8. They observed that the weld which was made by the hexagon tool resulted in very fine

grain distribution, as compared to the other tool pins.

Hence, it was concluded that the shape of the weld stir zone was dependant on the tool shape and tool geometry. Taper screw thread pin weld was reported to have the highest weld joint efficiency (75%) compared to the cylindrical tool pin profile [56].

2.3.3. Mechanical Properties

The FSW process causes various changes in the mechanical properties of the welded region. Overall, FSW leads to a joint region that is not necessarily superior to its parent alloys, but rather exhibiting middling properties with regard to its mechanical properties [4].

Micro-Hardness

Most age hardenable Al alloys typically exhibit a 'W'shape micro-hardness profile across the surface of their friction stir weldments [2, 6]. This is observed in Figure 2.9 given below for the AA2060 alloy.

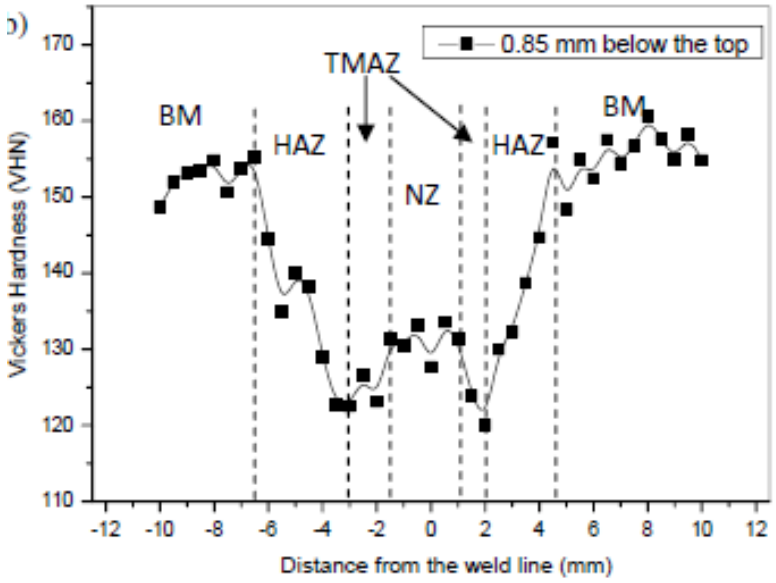

Figure 2.9: Micro-hardness profile on a cross-section of AA2060 weld [2]

The highest micro-hardness values are usually recorded in the peak aged base metal. This is because the strengthening precipitates such as T_1 phase, which contribute to the hardness, are still found in this zone after welding. The values decreases in the HAZ due to increasing coarsening and dissolution of the strengthening precipitates. This decreases continues until the boundary between the HAZ and the TMAZ is reached. The micro-hardness values of the stir zone can be either lower or higher than that of the TMAZ. This is dependant on the precipitation sequence of the alloy and the contribution of the grain boundaries to dislocation movement [6].

Reports in literature indicate that the lowest micro-hardness value is recorded in the interface or boundary of the HAZ and the TMAZ [2, 6, 55]. As mentioned above, this correlates to the change in amount of T_1 phase found in these regions. In Al-Cu-Li alloys, the micro-hardness variations across the FSW weld has been attributed to the evolution of the precipitates, which include dissolution, coarsening, and re-precipitation of the precipitates arising during the thermo-mechanical welding process and the subsequent cooling and ageing of the weld [2].

2.4. Corrosion on FSW metal

The corrosion behaviour of a friction stir welded aluminium alloy is of utmost importance if it is to replace the current generation of alloys. However, there is not enough literature on this topic. The research that does exist is contradicting and hence the corrosion attack on these alloys cannot be determined from them.

Bousquet et al. [57], who studied the corrosion sensitivity of an AA2024-T3 friction stir weld, reported that the HAZ is the zone most sensitive to corrosion. This was due to the coarse intermetallic compounds and precipitates that acted as anodic sites, which made the zone susceptible to both pitting and intergranular corrosion. On the other hand, Donatus et al. [6] reported that for the AA2198 alloy, the base metal was the most susceptible to corrosion. They attributed this to the concentration of the T_1 phase which was present in this zone. In the other zones the T_1 precipitate had dissolved due to heat treatment, however the base metal remained unaffected by it. Thus, the selective dissolution of the precipitates led to corrosion in the base metal.

These inconsistencies in the literature can be attributed to various factors such as artificial ageing of the alloy, anodising of the Al alloy, and even the alloying composition. However, there are a lot of factors which may affect the corrosion attack but aren't known yet. This is why it is necessary to study and evaluate the corrosion behaviour and the factors influencing them for friction stir welded Al-Li alloys.

2.4.1. Corrosion Susceptibility of Welded Alloys

In the study of corrosion resistance of friction stir weldment of AA2198 alloy by Donatus et al. [6], it was observed that all the severe localised corrosion (SLC) areas were found in the BM region of the weldment, as shown in Figure 2.10. Current density maps from SVET showed that the SZ had the least current density values. This proved that for the 2198 alloy, the SZ was the most resistant to corrosion. However, they did notice that over time, the current density values evened out across the entire surface of the alloy. This decrease in current density values was a result of the formation of intense corrosion products over the pit surfaces. For the other regions, oxide/hydroxide or chloride films formed over the entire weldment. This resulted in similar value for current density. Although, they suggested that corrosion still occurred in the alloy but beneath the surface.

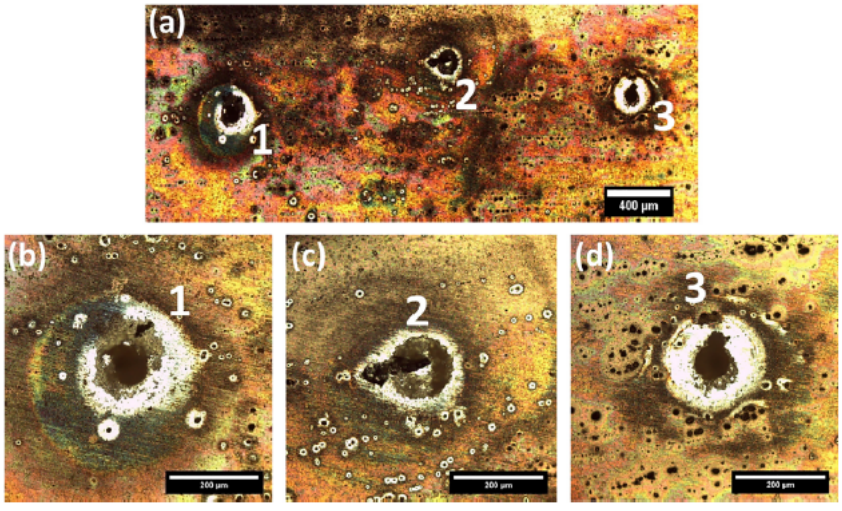

Figure 2.10: Optical micrographs of the severe localized corrosion sites in AA2198 alloy [6]

It was observed that the corrosion attack differed for every type of solution used for the immersion tests. The above test was conducted in 0.1M NaCl solution. The corrosion morphologies for 3.5% NaCl solution was somewhat different. Strange filiform-like corrosive attacks were obeserved in the SZ and some parts of TMAZ of the weldment in this solution. This is seen in the optical and SEM micrographs

shown below in Figure 2.11. It was suggested that this attack was due to the clustering of active elements in the region due to diffusion since these regions experience high temperatures. In exfoliation (EXCO) solution, the attack appeared to be related to the coarse second phase particles in the SZ. Intergranular corrosion was observed in the HAZ for both solutions. This was due to the precipitates in the grain boundary regions of this phase.

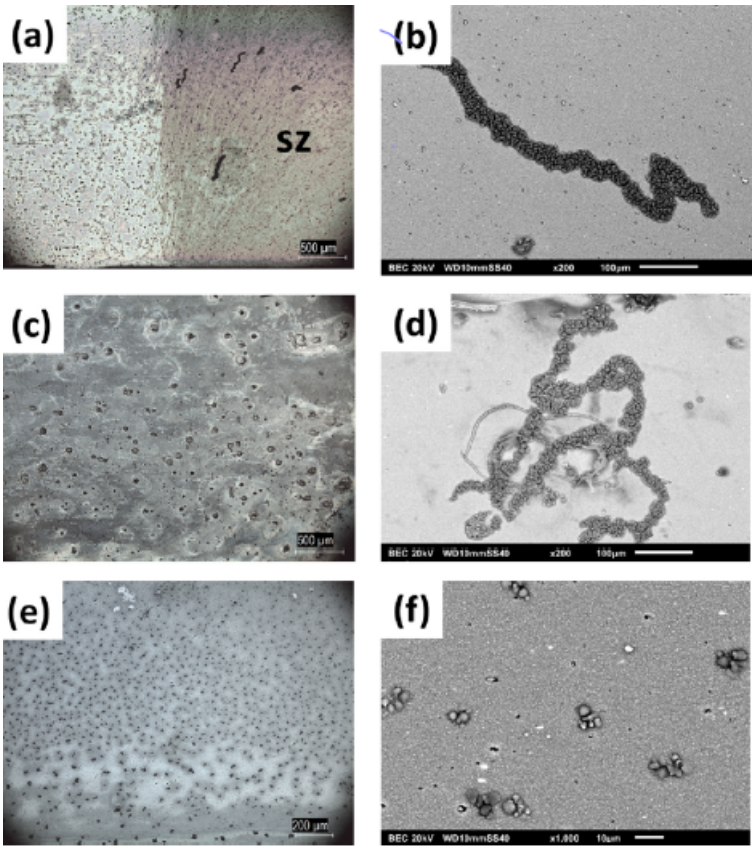

Figure 2.11: Optical and SEM micrographs of the SZ surface of AA2198-T851 friction stir weldment after 24 h immersion test in (a) & (b) 3.5% NaCl solution, (c) &(d) acidified 3.5% NaCl solution, and (e) & (f) EXCO solution [6]

The base metal experienced pitting in all three solutions, although the area, depth and amount of pits varied for all solutions. Hydrogen evolution was intense across the entire surface of the base metal. The BM was also galvanically coupled with cathodic regions such as HAZ, TMAZ, and the SZ which led to macro-corrosion in the region as well. Ch Venkata Rao et al. [32] reported similar findings on the study of AA2219 alloy weld. The stir zone of the weld was completely protected from corrosion damage as it had turned into a cathode. They suggested that the dissolution of precipitates in the weld stir zone and the coarsening of precipitates in the HAZ/TMAZ regions were the factors responsible for improved corrosion resistance in these regions.

2.4.2. Hydrogen (H_2) gas evolution

In the study of friction stir weldment of AA2198 alloy by Donatus et al. [6], the authors reported that in EXCO solution there was an intense evolution of hydrogen gas in the base metal region, which led to corrosion products. Upon further study, it was observed that these corrosion products formed were high in chloride concentration. This was not seen in other regions of the weldment nor in other solutions. The H_2 evolution was from the SLC sites in the base metal at its free corrosion potential, which confirmed that the BM region was highly susceptible to corrosion. This was attributed to the presence of high volume fraction of the T_1 precipitates.

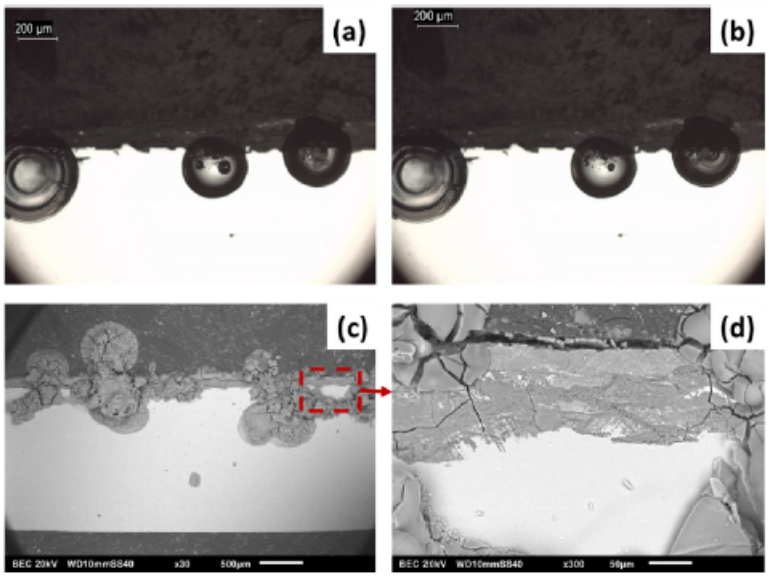

Figure 2.12: Cross-sectional Optical micrographs of the BM of AA2198 alloy weldment showing (a) Hydrogen gas evolution, (b) generation of liquid corrosion products, (c,d) SEM micrograph showing the corrosion products after solidification [6]

As it is known, the T_1 phase is more active than the Al matrix, which creates a galvanic cell between them. The T_1 phase dissolves by losing its Al and Li components, leaving a Cu rich particle behind. This particle now acts as a cathodic particle and starts dissolving the adjacent Al matrix. As the matrix dissolves with time, Cu is released into the electrolyte. This released Cu attains its free corrosion potential away from the bulk and becomes ionized. The formed Cu ions are later deposited at micro-cathodic sites. The Al ions formed from the dissolution of the active phases and the matrix react with H_2O to produce H^+ ions, which then combine by accepting electrons to produce H_2 bubbles [6].

2.4.3. Effect of Anodising

Anodising is the most widely used method for the protection of Al alloys against corrosion. In this process a passive porous oxide layer is made to form on the aluminium alloy which is then sealed by boiling in deionised water. However, anodising of weldments leads to the formation of different thickness of oxide layers on the various zones.

In the study of anodising behaviour of AA2198 friction stir weldment by Donatus et al. [3], it was observed that anodising significantly improved the corrosion resistance of the SZ and the BM. This could be seen from the significant decrease in current density values and increase in corrosion potential, as shown in Figure 2.13. Despite this, the corrosion rate of the BM in the anodic arm was still more than that of SZ.

The main issue with anodising was the varying oxide growth rates at the different regions of the weldment. It was observed that the rate of porous oxide layer formation was more on the weldment than on the BM. Thus, from the BM to SZ, the range of thickness increased for the oxide layer. This was explained by the volume fraction of the T_1 phase in these regions. The highest concentration was in BM and the lowest in the SZ where most of these precipitates had dissolved due to the high temperatures during welding. It was observed that the regions which have less T_1, had a higher content of Li in the solid solution. Thus, it was proposed by Donatus et al. [3] that the higher Li content in solid solution, the higher the oxidation rate of the region during anodising. This was in agreement with the experimental data, as the Li content in solid solution increased from the BM to HAZ/TMAZ to SZ, the same occurred with the oxide layer thickness.

The variations in the oxide layer thickness resulted in a reversed micro-hardness profile of the anodised alloy surface when compared to an bare alloy surface. The maximum micro-hardness values

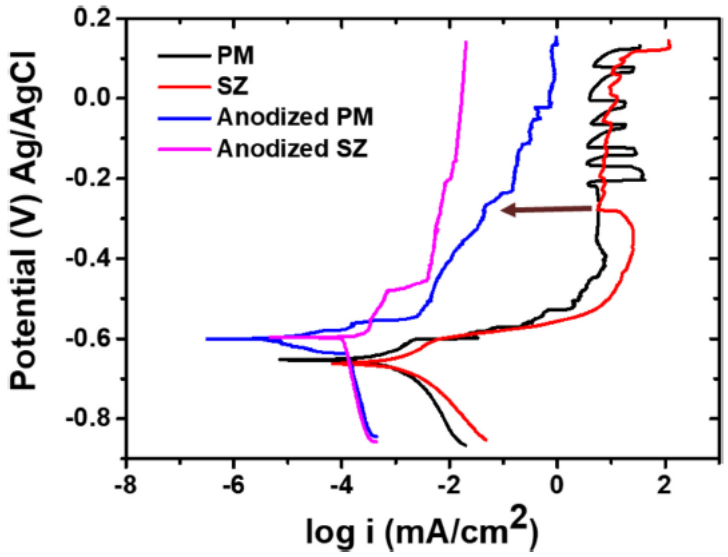

Figure 2.13: Potentiodynamic Polarisation curves of anodised and un-anodised PM and SZ regions of AA2198 alloy in 3.5% NaCl solution [3]

were observed in the SZ followed by the TMAZ/HAZ, while the lowest values were recorded in the base metal region.

2.4.4. Effect of Tool Pin Profile

Ch Venkata Rao et al. [32], who studied the pitting corrosion resistance of the AA2219 alloy friction stir welds, reported that comparatively uniform pitting corrosion resistance was observed throughout the cross section of the alloy for both tool profiles used - conical and triangular. However, pit density of the weld stir zone for conical tool profile was higher than that of triangular profile because a higher temperature was obtained in the stir zone for latter tool profile. The higher temperature resulted in proper dissolution/coarsening of the strengthening precipitates in the stir zone. Thus, the volume fraction of precipitates involved in pitting of the sample were less in the triangular profile than the conical profile, which gave a better result for the pitting corrosion resistance of the sample welded by a triangular tool profile.

A similar finding was reported by G. Ramababu et al. [5], who reported that for the AA2219 alloy, the joint fabricated using a hexagonal tool profile exhibited superior corrosion properties as compared to joints made by other tool pin profiles, due to its larger surface area.

2.5. Conclusion

The purpose of the current study was to evaluate the electrochemical and corrosion behaviour of friction stir welded 3rd generation Al-Li alloys and its microstructural behaviour. However, this goal cannot be achieved without further research in this topic. This chapter has compiled various trends of localised corrosion on base Al-Li alloys as well as on friction stir welded Al-Li alloys which helps in determining the localised corrosion behaviour on FSW AA2099 and AA2060 alloys. However, it was observed that even the smallest of factors such as tool pin profile or grain orientation can alter the behaviour of the alloys mechanically and electrochemically.

There have been a lot of contradictions regarding the corrosion behaviour and the factors influencing it. The role of the strengthening precipitate T_1 in the localised corrosion of these alloys needs to be evaluated. Most of the literature places this precipitate at the heart of the corrosion mechanisms in their work. However, all theories that they have put up regarding the dissolution or selective dissolution of

this precipitate is just conjecture at this point. Another gap in literature is the role of coarse constituent impurity particles in the Al-Li alloys. Some argue that these particles are the stepping stone to localised corrosion while others argue that it is the T_1 precipitate. The type of corrosive attack on these alloys also differ. This depends on factors such as type of solution used for the immersion tests, the heat treatment received by the alloy, and also the composition of the alloy. Further work needs to be done to establish what sort of corrosion attack would the AA2099 and AA2060 alloys experience.

The effect of anodising the Al-Li alloy (AA2198) does look promising in terms of corrosion resistance of the alloy, as seen by the work of Donatus et al. [3]. However, to apply this for practical uses, the effect of anodising AA2099 and AA2060 alloys needs to be studied to give an idea of whether this would actually benefit the corrosion resistance or not. Additionally, the effect it would have on the microstructure and mechanical properties of the alloy must be determined.

This study has shown the gaps present in current literature and the research work needed to be done to get a complete picture of the localised corrosion behaviour on the AA2099 and AA2060 FSW alloys and its effect on microstructure. A natural progression of this work is to first analyse the type and mechanism of corrosion attack on these welded alloys. This would be followed by the role of intermetallic particles in the mechanism of the corrosive attack. Lastly, the effect of anodising the surface of the alloys needs to be investigated. This would present the possibility to evaluate whether these alloy are fit to replace the current generation of alloys used for aerospace applications.

3

Experimental Details & Methodology

3.1. Specifications of the FSW samples

Commercially produced friction stir welded samples of Z-shaped extrusion of AA2099 T83 and cold rolled sheet of AA2060 T8E30 were provided by Arconic, Figure 3.1. The chemical composition of the 2 alloys is given in the Table 3.1. The samples received were of 3 types – as received sample, anodised sample, and sol-gel coated sample. A rotational speed of 1200 rpm and a welding speed of 250 mm/min in force control mode with an axial force of 6.25 kN was applied to weld the samples using friction stir welding [11].

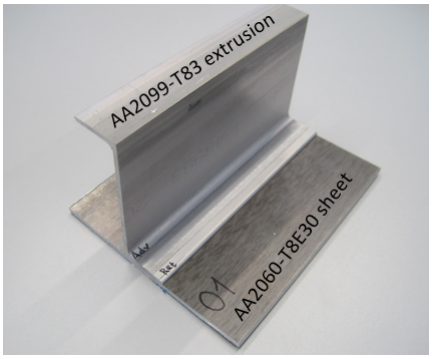

Figure 3.1: Friction stir welded sample of Z-shaped extrusion of AA2099 T83 and cold rolled sheet of AA2060 T8E30 alloys.

Table 3.1: Chemical composition of the base metals of the AA2060 T8E30 and AA2099 T83 alloys, wt % [11]

Alloy	Al	Si	Fe	Cu	Mn	Mg	Zn	Ti	Ag	Li	Zr
2060	Bulk	0.07	0.07	3.4-4.5	0.1-0.5	0.6-1.1	0.3-0.5	0.1	0.05-0.5	0.6-0.9	0.05-0.15
2099	Bulk	0.05	0.07	2.4-3.0	0.1-0.5	0.1-0.5	0.4-1	0.1	-	1.6-2.0	0.05-0.12

The anodised sample was produced by the thin film sulphuric acid anodising (TFSAA) method. The anodising bath had a sulphuric acid concentration of 43 g/L. The anodizing voltage used was 15 V, and was reached by a maximum ramping up from zero at 5 V/min. The total immersion time in the anodising bath was 24-26 minutes and the sample was sealed by boiling in deionized water [58].

The sol-gel, or solution gelation, coating used on the surface of the sample was 3M Surface Pre-Treatment AC - 131. This is a silicane based non-chromated coating for use on aluminium, steel, and titanium alloys. It effectively improves adhesion between the metallic surface and the epoxy or polyurethane-based organic coatings. It was applied by spraying after mild alkaline cleaning and de-oxidizing of the metallic surface to obtain a layer of thickness between 1 - 2 μm [58].

3.2. Sample preparation

The sample preparation was different for the as-received samples and for the anodised and sol-gel coated samples. The anodised and sol-gel BM samples were cut into square coupons of 20 mm x 20 mm using a guillotine. The SZ of the samples were also cut into samples of 20 mm x 20 mm using a Streurs cutting machine. They were rinsed in distilled water, followed by ethanol and dried using compressed air. Extra care was taken to make sure the surface treatments were not damaged while preparing the samples.

Sections of the as-received sample were cut perpendicular to the welding direction using a Streurs cutting machine to obtain cross-sectional samples of the entire welded region in 4.5 mm x 23.5 mm rectangular coupons. The samples were either mounted in Kemet Acrylic CLB cold-curing conductive epoxy resin for microstructure evaluation, micro-hardness testing, and immersion testing, or in Struers ClaroCit cold-curing non-conductive epoxy resin for the electrochemical tests. They were then mechanically polished sequentially from 180 – 4000 grit Struers silicon carbide abrasive papers using distilled water as a lubricant, followed by 3μ and 1μ diamond pastes to obtain a mirror finish surface. The samples were then rinsed with distilled water, followed by ethanol and dried using compressed air.

The as-received samples used for microstructure evaluation and immersion testing were etched using Keller's reagent (1 mL HF + 2.5 mL HNO_3 +1.5 mL HCl + 95 mL H_2O) for 10 seconds, giving the sample a matte finish surface. The etched samples were rinsed using distilled water followed by ethanol to remove excess etching solution and then dried using compressed air.

3.3. Microstructure Evaluation

Microstructural characterization was performed using VHX 5000 Keyence digital Microscope, Leica DM-LM Optical Microscope, and Joel JSM IT100 Scanning Electron Microscope (SEM) fitted with Energy Dispersive X-ray Spectroscopy (EDS) to evaluate elemental analysis of the specimen. The samples used for microstructure characterization were polished and etched as described in the section earlier.

3.4. SEM & EDS

3.4.1. Theory

In scanning electron microscopy (SEM), an electron gun is used to emit a beam of electrons at an acceleration range between 1 keV and 30 keV. The surface of the sample used is penetrated by the beams of electrons at a region called interaction volume and depending on the depth different signals can be detected. At the regions close to the surface, secondary electrons are emitted which possess energies of less than 50 eV. These are a result of the inelastic collision and scattering of incident electrons with specimen electrons [59]. This is seen in Figure 3.2. Backscattered electrons are a result of an elastic collision and scattering event between incident electrons and specimen electrons. They can be generated further from the surface of the material and possess energies of more than 50 eV [59].

Electron dispersive x-ray spectroscopy (EDS) provides elemental information of the material under analysis by analysing the x-ray signals emitted from the sample. The x-ray signal is a result of recombination interactions between free electrons and positive electron holes that are generated within the material. The x ray signal can originate from further down into the surface of the sample [9]. It is important to note that lithium cannot be detected by EDS due to its low atomic mass [60].

3.4.2. Sample Preparation for SEM

The samples were mechanically polished sequentially from 180 – 4000 grit silicon carbide abrasive papers using distilled water as a lubricant, followed by 3μ and 1μ diamond pastes to obtain a mirror finish surface. The samples were then rinsed with distilled water, followed by ethanol and dried using compressed air. The samples were then degassed in vacuum chamber till a pressure of $1.0x10^{-1}$ mbar was reached. The samples were then removed and mounted on the SEM specimen holder using

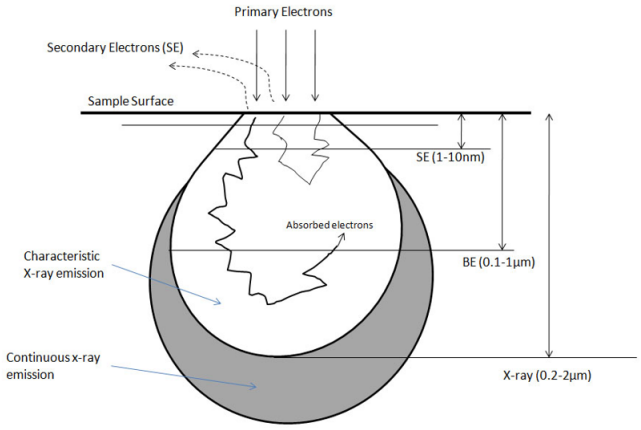

Figure 3.2: Schematic diagram of the signal detection regions within the interaction volume [7].

a Nisshin EM carbon conductive double sided tape.

3.4.3. Image Analysis

The microstructure images obtained from SEM were analysed in Adobe Photoshop CC 2019 to determine average grain size and area. This was done by first calibrating the image to scale. Next, a specific population of primary grains were selected from the image and the measurements of grain area, perimeter, width and height were recorded. An mean value of the measurements were obtained along with their standard deviation and standard error.

The evaluation of average intermetallic size and population density of the intermetallic particles were done using ImageJ software. The scale of the image was adjusted followed by cropping out the borders of the image. The threshold of the image was adjusted to record the distribution of both the coarse constituent particles (represented as bright spots under SEM) and hardening precipitates and dispersoids (represented as dark spots under SEM). This resulted in measurements of total number of intermetallics, population density, and average area and perimeter of the intermetallic particles.

3.5. Micro-hardness Testing

3.5.1. Theory

The vickers micro-hardness measurements were carried out using a Struers DuraScan micro-hardness testing machine. In this method, an indentation is made on the surface of the sample using a diamond indenter tip in the form of a right pyramid with a square base and an angle of 136 degrees between opposite faces subjected to a load. The full load is applied for a time period of 10 -15 seconds. Once an indent is formed, Figure 3.3, the 2 diagonals of the indentation are measured using a microscope and their average is calculated. The vickers micro-hardness is calculated by dividing the load by the square mm area of indentation. It is given by the equation as follows:

$$HV = \frac{2F\sin\frac{136}{2}}{d^2} \tag{3.1}$$

where,
F = load in kgf,
d = Mean of the two diagonals d1 and d2 in mm,
HV = Vickers micro-hardness.

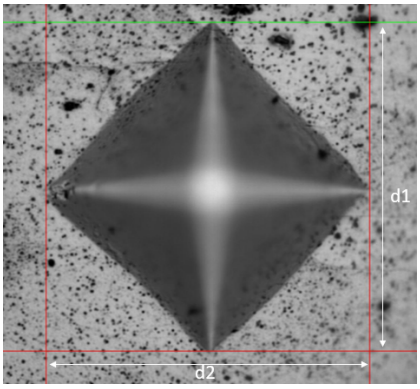

Figure 3.3: Indent formed by the diamond tip indenter of the Vickers Micro-hardness tester.

3.5.2. Experimental Set-up

The polished sample as described earlier was placed on the specimen stage. A load of 0.5 kgF was applied for a dwell time of 10 seconds. An edge distance of 0.5 mm and a distance of 10 D (D = diameter of tip) was applied between every 2 consecutive indentations to avoid any discrepancies in the measurements. The average mean of the recorded measurements were calculated with the standard deviation and standard error.

3.6. Electrochemical Testing

The electrochemical experiments were conducted using a 3-electrode electrochemical cell connected to a Biologic Science Instruments VSP-300 Potentiostat. The sample was used as the working electrode, a platinum plate mesh as a counter electrode, and a Ag/AgCl (saturated KCl) as a reference electrode, as seen in Figure 3.4.

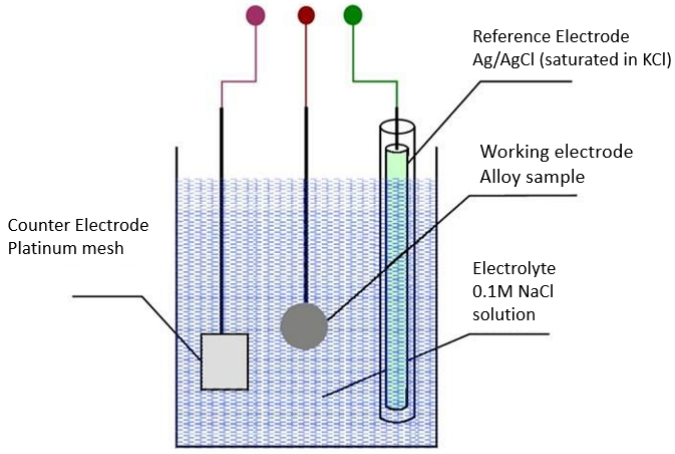

Figure 3.4: Schematic diagram of the electrochemical cell used [8].

3.6.1. Sample preparation for Electrochemical Tests

The samples were mounted in non-conductive cold curing resin with a copper wire attached to the rear surface of the sample to connect with the potentiostat. The samples were then polished to 1 μ finish. Since the weld regions were very narrow in width, the sample was masked with a non-conductive tape on which a defect of 1mm in diameter and exposed surface area of 0.00785 cm^2 was made using a biopsy needle to isolate the zones from each other. The samples were then connected to the electrochemical cell using copper (Cu) adhesive tape. The software used for conducting the electrochemical

tests was EC-lab V11.21.

For the anodised and sol-gel samples, the base metals and stir zone were cut into square coupons of 20 mm x 20 mm. Subsequently, they were rinsed in distilled water, followed by ethanol and dried using compressed air. Extra care was taken to make sure the surface treatments were not damaged while preparing the samples. The exposed region was a circle of 3 mm diameter and a surface area of 0.283 cm^2.

3.6.2. OCP & LPR Monitoring

The open circuit potential (OCP) and linear polarisation resistance (LPR) was monitored over a total experimental period of 24 hours in a freshly prepared 0.1M NaCl aqueous solution of near neutral pH at room temperature and in contact with the room atmosphere. The OCP was measured at 1 hour intervals. At the end of each time interval the linear polarisation resistance was measured with a sweep rate of dE/dt = 0.167 mV/s between a range of ± 10 mV vs OCP. An R_P fit was applied to the results one loop at a time to obtain the resistance of the sample as a function of time. This polarisation resistance R_P was determined by taking the inverse of the slope of the current density vs. potential curve at the free corrosion potential, as seen in the equation 3.2. The experiments were repeated 3 times to assure the reproducibility of results.

$$R_P = \frac{1}{\frac{dI}{dE}} \tag{3.2}$$

3.6.3. Potentiodynamic Polarisation

Potentiodynamic polarisation tests were performed by linear sweep voltametery. The anodic and cathodic polarisation were performed separately on the samples since reports in literature have shown that prior cathodic polarisation induces pitting on the sample surface[61]. This experiment was conducted in a freshly prepared 0.1M NaCl aqueous solution of near neutral pH at room temperature and in contact with the room atmosphere. The samples were kept at OCP condition 2 hours prior to potentiodynamic polarisation to reach steady state. A sweep rate of dE/dt = 0.167 mV/s was applied between -0.050 V and 1 V vs OCP for anodic polarisation and between 0.050 V and -1 V vs OCP for cathodic polarisation. Once the polarisation curves were obtained, a Tafel fit was applied to the anodic polarisation curves to obtain the corrosion potential (E_{corr}) and corrosion current density (I_{corr}) of the sample. The experiments were repeated 3 times to assure the reproducibility of results.

3.7. In-situ Immersion Testing

The in-situ immersion test was based on the novel technique by Sullivan et. al. to reveal the localised corrosion mechanism and preferential phase attack in the microstructure of the sample [62]. In-situ immersion tests were carried out over a total experimental period of 24 hours in a freshly prepared 0.1M NaCl aqueous solution of near neutral pH at room temperature and in contact with the room atmosphere. All the chemicals used were of analytical grade and provided by Sigma-Aldrich Chemical Company.

3.7.1. Sample preparation for In-situ Immersion Testing

The polished and etched samples, as described earlier, were masked with thick PTFE tape (3M Ltd) exposing a circular area of 0.5 mm diameter of the selected weld zone using a Welltech Rapid-Core biopsy needle. The remaining exposed areas were also masked with PTFE tape to make sure that the rest of the sample did not come in contact with the electrolyte during the experiment. The samples were then secured inside a petri dish using PTFE tape.

3.7.2. Experimental Set-up and Apparatus

The experimental set up and apparatus used for the in-situ immersion tests are shown in the Figure 3.5(a). An optical microscope (Leica DM-LM) with a movable stage and fitted with a Lumen*era* Infinity I

camera was used as the main experimental apparatus. A built-in protective cap with a thin microscope slide glued on its one end was used as a cover for the microscope lens. This was done to prevent the contamination of the microscope lens from the electrolyte and preserve the good resolution and focus of the image [9].

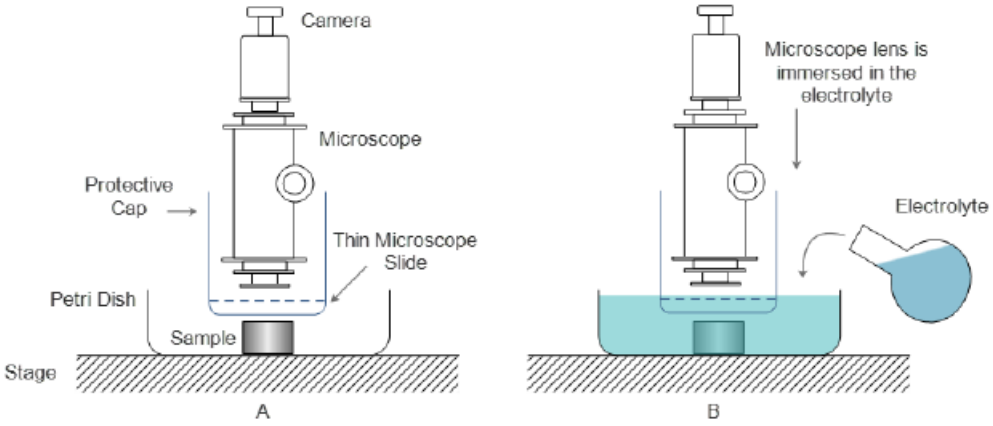

Figure 3.5: Schematic diagram of the In-situ Immersion test technique (a)Experiment set-up ,(b) Submersion of sample in the electrolyte during the experiment [9].

The petri dish containing the sample was then placed under the objective lens of the optical microscope. The focus and light intensity were adjusted on the exposed area of the sample. The petri dish was filled with 250 ml of freshly prepared 0.1 M NaCl aqueous solution as the electrolyte and the focus was adjusted to obtain a clear image through the electrolyte, as seen in Figure 3.5(b). Air bubbles which appeared on the sample's surface was removed by a pipette. Digital images were taken by the Infinity Analyze software every minute for 24 hours using the time lapse function of the camera that was attached on the microscope lens.

At the end of the experiment, the optical microscope images were imported to Adobe Photoshop CC 2019 for further analysis. The samples were desmutted in a solution of 30 % HNO_3 to remove the corrosion products from the surface and were then studied under the SEM. The SEM images were also further analysed in Adobe Photoshop CC 2019.

3.7.3. Image Analysis

The images obtained from the experiment were analysed in Adobe Photoshop CC 2019. The image analysis was performed by first calibrating the scale of the image as required. Once the scale was calibrated, the attack site area, pit areas, and corrosion ring radius were measured using the magnetic lasso tool and were recorded. The SEM images of the desmutted samples were also analysed here by first calibrating the image to scale. The attack site areas and pit areas were measured again to verify the recorded values.

3.8. Scanning Kelvin Probe

The Scanning Kelvin Probe (SKP) is a non-destructive, non-contact method for testing the condition of the surface of conductor, semi-conductor, and dielectric samples. It is an extremely sensitive analytical tool which measures the changes in difference of contact potential between a reference material and a sample under study which depend upon changes in the electron work function (EWF) of the material under investigation. The EWF is defined as the amount of energy needed to release electrons from the surface of the material [63].

3.8.1. Theory

The SKP operates by creating a parallel-plate capacitor between an electrically conductive probe vibrating perpendicularly and the sample surface, as seen in Figure 3.6. When external electrical contact between the probe and sample takes place by the application of a backing potential V_b, the Fermi levels of the probe and sample surfaces start to equalize, resulting in a charge flow which in turn generates a contact potential difference V_{CPD}. The V_{CPD} then aids us in calculating the work function, surface potential, or Fermi levels of the sample surface, since they are related.

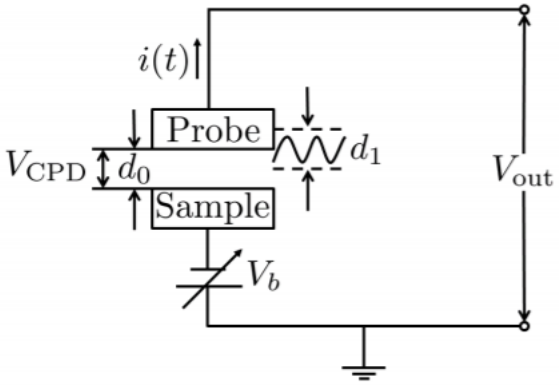

Figure 3.6: Schematic diagram of the principle of operation of a Kelvin Probe [10].

The work function of a surface is defined as the potential energy of an electron between the vacuum level and the Fermi level and is given by

$$\Phi = -e\phi - \epsilon_F \tag{3.3}$$

where, Φ is the work function of the surface, $-e$ is the elementary charge, ϕ is the electrostatic potential in vacuum, and ϵ_F is the Fermi level of the material. Thus,$-e\phi$ is the energy of an electron at rest in vacuum [10].

3.8.2. Sample preparation for SKP

The cold-cured conductive mounted sample was finely polished and etched with Keller's reagent, after which it was rinsed using ethanol followed by distilled water. The sample was then dried using compressed air. The Gold (Au) probe tip used for this experiment was calibrated with the specimen stage and the sample was then placed on the stage in the relative humidity chamber. The probe was brought close to the region under inspection and kept at a height of at least 1 mm above the sample surface to avoid collision of the probe with the sample. Once this was done, the step size and total area to be scanned was selected and the experiment was initiated.

4

The Effect of Friction Stir Welding on the Microstructure & Mechanical Properties

4.1. Introduction

The microstructure of the Al-Li alloys change drastically when welded by FSW, forming different regions based on the plastic deformation and thermal cycle each region has undergone [5, 31, 53]. Therefore, it is necessary to study the microstructural behaviour and the distribution of intermetallic particles in the welded regions of the sample to understand the localised corrosion behaviour of the alloys. In this chapter, the microstructural characteristics such as the average grain area, chemical composition and average size of the intermetallic particles were studied and evaluated along with the micro-hardness of the corresponding weld zones to determine the relation between them.

4.2. Materials and Experimental Methods

The samples used for the microstructure evaluation were obtained from the as received welded sample of the Z-shaped extrusion of AA2099-T83 and cold rolled sheet of AA2060-T8E30 provided by Arconic. The sample preparation for microstructure characterisation and micro-hardness measurements have been explained in chapter 3. The microstructure characterisation techniques used are also given in chapter 3.

4.3. Results

4.3.1. Microstructure Characterisation

Figure 4.1 is an image of the weld joint cross-section seen under a Keyence Microscope. The AA2099 T83 alloy is located on the top and used as the stringer, whereas the AA2060 T8E30 alloy, which is located at the bottom, is used as the skin. The two alloys are welded in the centre using FSW, which causes the formation of different zones based on the mechanical deformation and thermal cycles each zone undergoes.

As it is observed, the weld joint can be distinguished into 4 main zones. These are the stir zone (SZ), the thermo-mechanically affected zone (TMAZ), the heat affected zone (HAZ), and the base metal (BM). The SZ is 5 mm in width for the AA2060 T8E30 alloy but it is much larger at the top, which is 12 mm width in the AA2099 T83 alloy. The TMAZ is a very thin zone all around the SZ. The width of this zone is between 0.3 - 1 mm. The next zone is the HAZ, which is located on the outer region of the TMAZ. The HAZ does not have a definite boundary, since the effect of heat dissipation after welding could be transmitted to a larger area. Thus, this region would be approximately between 2.5 - 4 mm in width. The last region is the BM, which is located on either ends after the HAZ, since it remains unaffected by the welding process. The welded zones are not always well defined, but can be also be estimated by other factors such as hardness and grain size of the zones. They are discussed below.

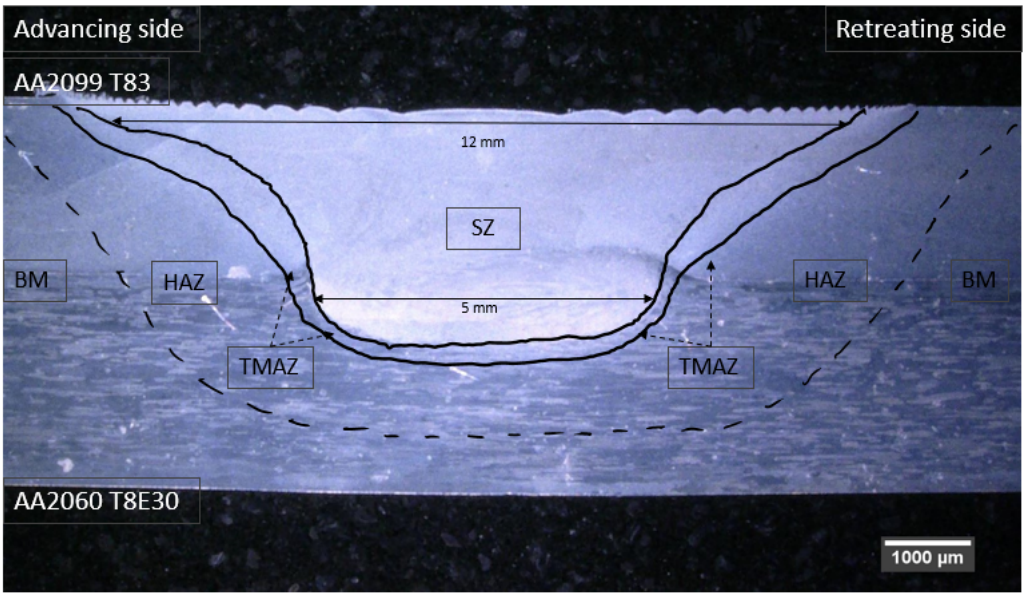

Figure 4.1: Keyence image of weld joint

Microstructure characteristics of the AA2099 T83 alloy weld zones
The BM is the region where the metal has not been affected by plastic deformation or heat caused due to the welding process. In the Figure 4.2(a), the typical microstructure of the BM of AA2099 T83 alloy is observed. From this image, various microstructural features of the alloy are revealed such as the grain boundaries, the coarse constituent particles, hardening precipitates and dispersoids.

An EDS scan on the sample revealed that the bright/ lighter spots on the surface represent heavier elements, which would be copper (Cu) and/or iron (Fe) particles in this case along with trace elements such as manganese (Mn), magnesium (Mg), and silicon (Si). These particles are coarse constituent particles in the matrix of the alloy [30, 60]. When the particles are just Cu-rich, they have a concentration of around 65 - 75%, whereas if the particles have other elements, the concentration of Cu in the particles are around 5 - 10% .

The dark spots on the other hand, represent elements that are lighter than the matrix. These include the dispersoids and the hardening precipitates of the alloy. The hardening precipitates are located mainly at dislocations and grain boundaries, whereas the dispersoids have a more homogeneous distribution all over the matrix. An EDS scan revealed that these hardening precipitates are rich in Al-Cu, with the concentration of Cu between 5 - 7%. Another feature that is observed from the image is the grain boundaries of this alloy. The grains of the BM of AA2099 T83 alloy are quite small in size, with an average area of 46.35 ± 11.09 μm^2.

The HAZ is the region of the weld joint that lies between the BM and the TMAZ on both sides of the weld, i.e. on the advancing side as well as the retreating side, as observed in Figure 4.2(b),(c). Although this region does not undergo any plastic deformation, it is subjected to a thermal cycle. This region of the weld shows some similarities with the microstructure of the BM regarding the grain morphology. However, they can be distinguished from each other by observing the differences between the average grain area. Another important observation is that the HAZ on the advancing and retreating sides are not completely similar to each other. This is due to the effect of the tool rotation and its subsequent effects such as material flow, and thermal dissipation [54]. These zones can also be differentiated by the shape and average area of the grains.

The average grain area of the HAZ-AS is 57.54 ± 7.63 μm^2 whereas that for the HAZ-RS is 41.22 ± 5.29 μm^2. The grains on the AS are elongated and more oval in shape. The grains on the RS, on the other hand, are similar to the BM in terms of shape and orientation. It has also been observed that the

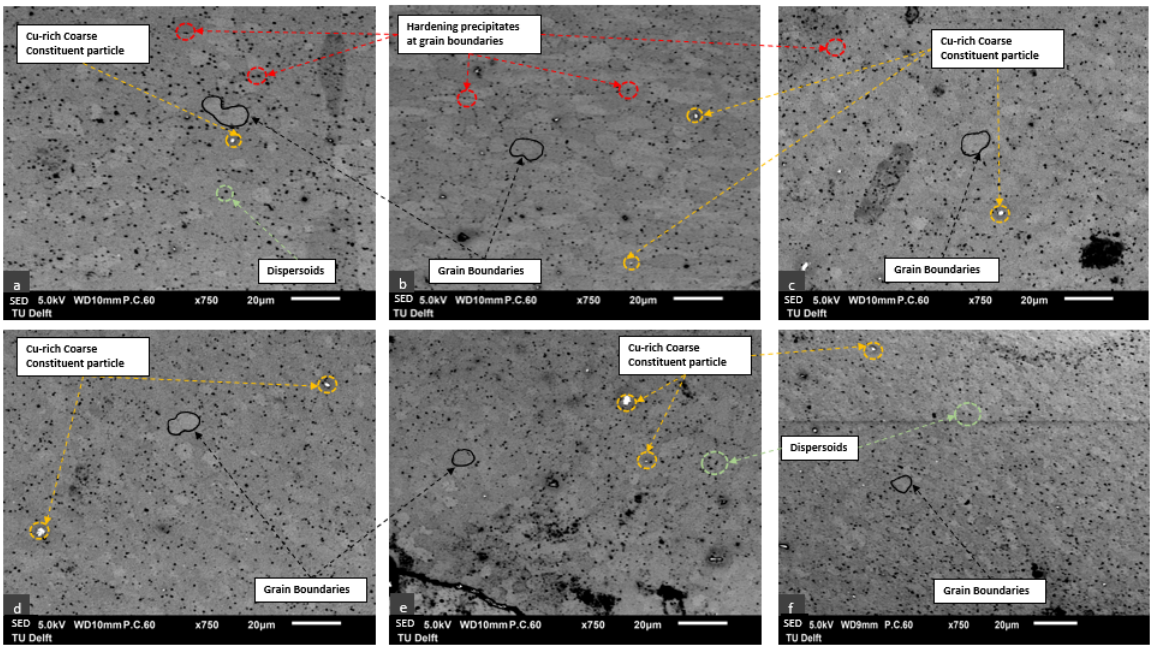

Figure 4.2: SEM images of microstructure of AA2099 T83 alloy (a) BM, (b) HAZ-AS, (c) HAZ-RS, (d) TMAZ-AS, (e) TMAZ-RS, (f) SZ.

coarse constituent particles and hardening precipitates are smaller in size in the HAZ-AS compared to the RS. The retreating side also has a higher density of these intermetallic particles.

TMAZ is a fine transition zone between SZ and HAZ,on both sides of the weld joint (Figure 4.2(d, e)). The grains inside the TMAZ were distorted by the strain induced by severe stirring motion of the tool pin during the welding process [2]. This zone is also affected by the heat generated from the welding process. However, the microstructure of the TMAZ is unmistakeably of its parent metal, even though it is rotated and highly deformed. The grains in this zone are clearly smaller than both the HAZ and the BM, with an average grain area of the TMAZ-AS as 32.18 ± 5.09 μm^2 and that for the TMAZ-RS as 19.17 ± 2.13 μm^2. The RS, as is seen from Figure 4.2, has a significant amount of coarse constituent particles (lighter spots) on its surface, as compared to the AS. The dispersoids are the largest in size and number in the RS and then the AS, due to its proximity to the SZ.

The Stir Zone (SZ) is located right at the centre of the weld joint (Figure 4.2(f)). It is the region that roughly corresponds to the path of the tool pin during welding. It undergoes maximum localised plastic deformation and temperature change during FSW [57]. Due to these reasons, the average grain area of the material in this zone is very small compared to that of the BM. The microstructure of this zone has constituents of both the alloys involved in the FSW due to material flow in the welding process.

The average grain area of the SZ is 17.72 ± 2.65 μm^2, which is the smallest amongst all the other zones. This is due to recrystallisation of the grains due to the heat from FSW. The coarse particles here are large in size, however few in number. The presence of Si in the amount of 2 - 7% was revealed with an EDS scan on these coarse particles. The dispersoids, on the other hand, is found in excess in the SZ, to control the grain size after recrystallisation. The population and average size of the intermetallics are further discussed in the next few sections.

Microstructure characteristics of the AA2060 T8E30 alloy weld zones

The BM of the AA2060 T8E30 alloy is seen in the SEM image in Figure 4.3(a). This image is the typical microstructure of the cold rolled alloy. The grains here are large in size and flat in shape. The average grain area of the BM is 52792.46 ± 12490.95 μm^2, which is a huge difference as compared to that of the AA2099 T83 alloy.

The coarse constituent particles here are densely distributed in the matrix and are also large in size. These coarse particles are Cu-rich intermetallics with traces of Mg and Fe in a few of them. The hardening precipitates are located on grain boundaries and dislocations in the alloy. They are small in size, but are distributed in large numbers on the alloy and have a high concentration of Cu in the range of 5-12%. There are also few dispersoids in the matrix of the alloy. These are larger in size compared to the hardening precipitates.

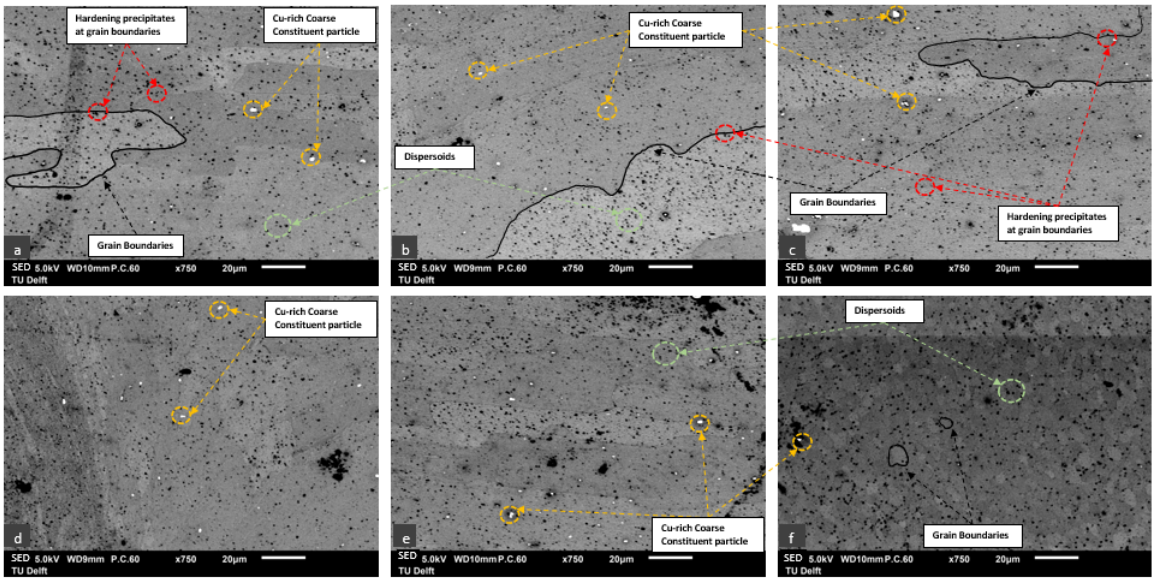

Figure 4.3: SEM images of microstructure of AA2060 T8E30 alloy (a) BM, (b) HAZ-AS, (c) HAZ-RS, (d) TMAZ-AS, (e) TMAZ-RS, (f) SZ.

The HAZ region in this alloy is quite a large region (Figure 4.1), and the microstructure can be seen in Figure 4.3(b, c). The grains have similar structure to the BM, however they are upto 60% smaller in size. The average grain area of the HAZ-AS is 20179.79 ± 5301.80 μm^2 and that of the RS is 18471.35 ± 3689.75 μm^2, which is considerably less than that of the BM. The heavier coarse particles are similarly sized in both the AS and the RS, however they have a larger distribution in the AS as compared to the RS. The dispersoids and hardening precipitates are found in large numbers in both the HAZ regions. These particles have a large variation of Si concentration in them (3-11%), which was found by performing an EDS scan on the zone.

In the AA2060 T8E30 alloy, the TMAZ region is a very small one with a maximum width of 0.5 mm. This can be seen in the Figure 4.1. The microstructure of this zone is affected by both heat and plastic deformation which causes the grains to be deformed and intermetallics to break down to smaller particles [4], as is observed in Figure 4.3(d),(e). The coarse particles here are much smaller than in other zones and are also less densely populated here. The dispersoids, on the other hand, are the largest in size here and can be found all over this region.

Figure 4.4(a, b) shows the TMAZ region on either side of the weld stir zone, i.e. AS and RS respectively. In both these images, there are a few similar observations. Firstly, the region affected by both plastic deformation and heat is quite narrow. Next, the grains here are bent, elongated and eclipsed shaped since they are quite large and they continue into the HAZ. This was also observed by Akhtar et. al. [53] in their study on the AA2060 alloy. This is also the reason due to which the average grain area of this zone cannot be determined.

The SZ of the AA2060 T8E30 alloy is seen in Figure 4.1. It is approximately 5 mm in width and 1 mm in height. This zone is a mixture between both the alloys and their elements. The average grain area of the SZ is 28.533 ± 3.15 μm^2, which is very small compared to any other zone of this alloy. There is

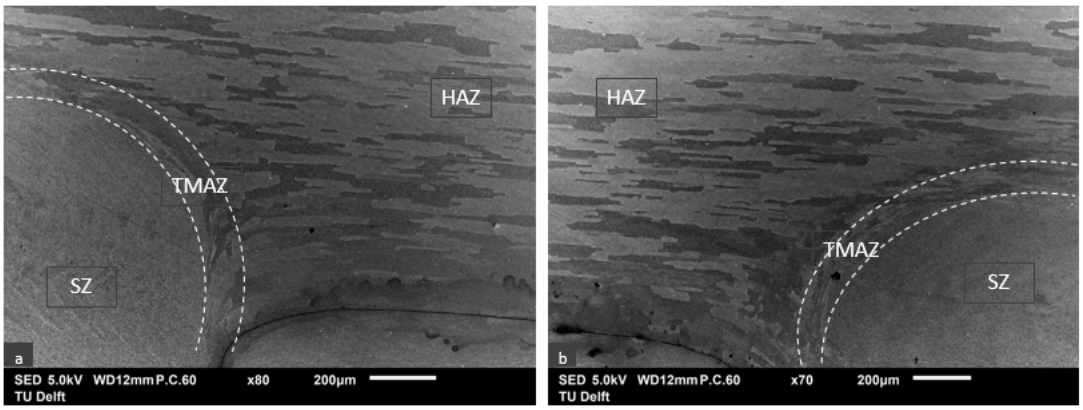

Figure 4.4: SEM images of TMAZ of AA2060 T8E30 alloy (a) AS, (b) RS.

a 99.95 % reduction in size in the SZ compared to the BM of the same alloy, due to high temperatures in the SZ during FSW process which cause recrystallisation of the grains. However, the grains here are still larger than the AA2099 T83 alloy SZ.

There are very few coarse constituent particles in this zone, and they are also the smallest in this zone. Since the tool pin rotates in this zone while welding, the coarse particles are broken down into smaller particles and are flung to the neighbouring zones [4]. However, there are coarse particles here that have a Cu concentration as high as 80%, with trace amounts of elements such as Mg (0.93%). Dispersoids are located in abundance in this zone. They have been added to reduce the grain size during recrystallisation [50].

4.3.2. Average Grain Area

The SEM images of the welded zones of both alloys were analysed in Adobe Photoshop to determine the average grain area. From the Figures 4.2 and 4.3, a specific population of primary grains were selected and measured. The average value of these grain areas were calculated along with the standard deviation and error.

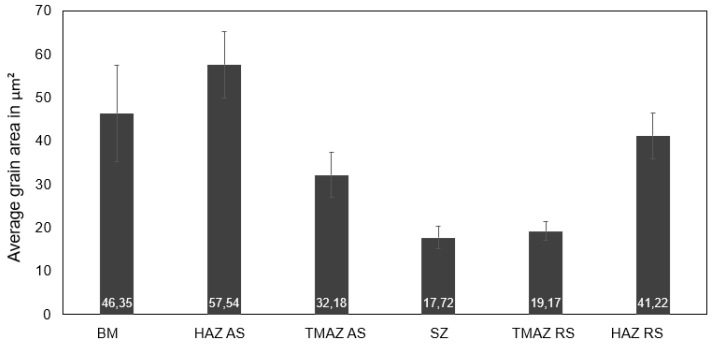

Figure 4.5: Average grain area of AA2099 T83 alloy.

The mean grain area of various zones of the AA2099 T83 welded sample has been depicted in the graph in Figure 4.5. The grain areas have been measured in both the advancing side as well as the retreating side of the weld joint. There is a clear trend of grain area reduction observed as the SZ is approached from either side of the weld joint.

The BM of this alloy has an average grain area of 46.35 ± 11.09 μm^2. This has been used as the

point of reference for comparison amongst the average grain areas of the zones in this alloy. The HAZ regions on both sides have very high values compared to the other zones, however the AS has bigger grains than the RS. The HAS AS has a 24% increase in grain size whereas the RS has a 11.1% reduction compared to the base metal.

The TMAZ regions have even smaller grains than the HAZ regions due to its proximity to the weld centre. Similar to the case of the HAZ region, the TMAZ-AS region has relatively larger grains with a value of 32.18 ± 5.09 μm^2. This implies that the reduction of average grain area is 30.58%. The reduction in TMAZ-RS is 58.65% , which is almost twice that of the AS. It has an average grain size of 19.17 ± 2.13 μm^2. The SZ has the smallest grains amongst all zones in the AA2099 T83 alloy, with the average grain area value of 17.72 ± 2.65 μm^2. This is a huge reduction of 61.77% as compared to the BM region.

The trend of the average grain area for the AA2099 T83 weld zones is a decreasing trend towards the weld centre. The HAZ-AS region is the peak on the left side, whereas the RS on the right side. From both ends, the grains get smaller all the way towards the weld centre, i.e. the SZ. This shows that there is a direct relation between the average grain area and the distance to the weld centre, and therefore to the heat generated during the FSW process. Another important observation is that the grains in the AS are much larger than those in the RS, which is why the shape is irregular.

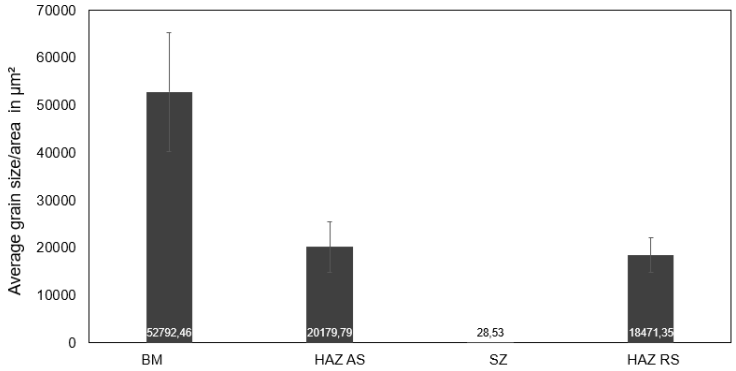

Figure 4.6: Average grain area of AA2060 T8E30 alloy.

The AA2060 T8E30 average grain areas in presented in Figure 4.6. The BM has very large grains with a value of 52792.46 ± 12490.95 μm^2. These grains are over a thousand times larger than those of the AA2099 T83 BM. This is due to the differences in production and processing methods of both alloys.

The trend of the grain sizes in this graph is also a decreasing trend towards the weld centre. The HAZ regions have relatively smaller grains with a reduction of 61.78% in the AS and 65.02% in the RS as compared to the BM. The SZ has the smallest grains here as well, with an average grain value of 28.533 ± 3.15 μm^2. This is a drastic 99.95% reduction of grain size in the alloy.

4.3.3. Intermetallics Size and Population Density

The SEM images of the welded zones of both alloys from Figures 4.2 and 4.3 were analysed in ImageJ to calculate the population density of the intermetallics on the surface and the average intermetallics area. The total surface area of the analysed images was 19622.7 μm^2. The dark particles from Figures 4.2 and 4.3 are the hardening precipitates and dispersoids in the alloy. Since the images could not be used to distinguish these two particles from each other, the average grain area was also considered in addition to the population density to understand this better. The coarse constituent particles were the lighter spots in the images.

The population density of intermetallic particles on the surface of the AA2099 T83 alloy has been represented in the graph in Figure 4.7 as area percentage. From this graph, it is clear that the BM

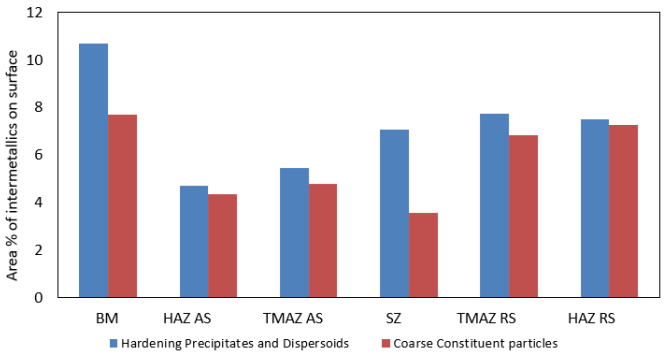

Figure 4.7: Area % of intermetallics on the surface of AA2099 T83 alloy.

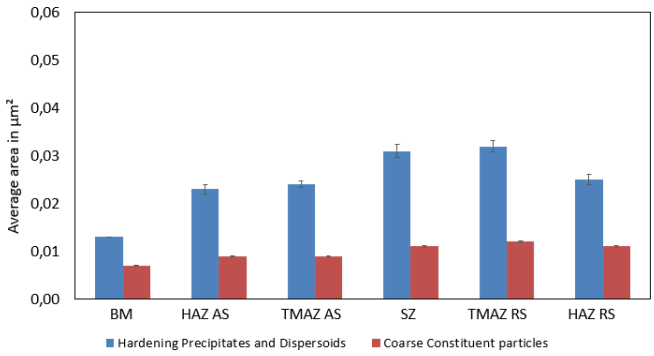

Figure 4.8: Average intermetallics size/area of AA2099 T83 alloy.

is most densely populated with both the coarse particles and the precipitates and dispersoids. Here onwards, the coarse particles has a decreasing trend all the way to the SZ and then increasing from the SZ towards the HAZ RS. The hardening precipitates on the other hand, is at its lowest in the HAZ AS and increases all the way from there to the other side of the weld joint, i.e. the HAZ RS. It is important to note that the TMAZ RS has a slightly higher population density than the HAZ RS.

Figure 4.8 is a graph showing the average intermetallic particle area of each weld zone of the AA2099 T83 alloy. The mean area of the coarse particles has an increasing trend towards the weld centre. The average size increases from the BM to the SZ and decreases again towards the HAZ RS. The hardening precipitates and the dispersoids average size has a similar trend as well. It is also observed that the AS has smaller particles compared to the RS.

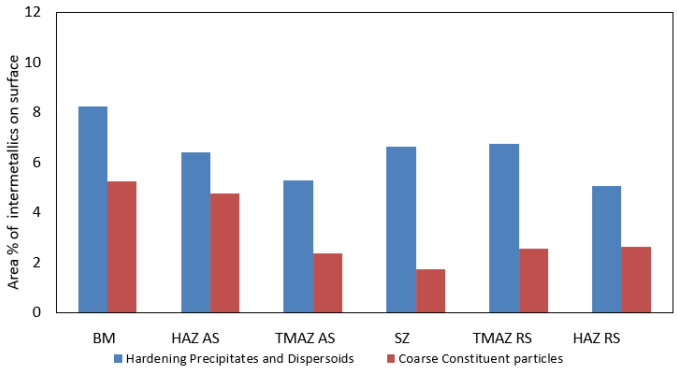

Figure 4.9: Area % of intermetallics on the surface of AA2060 T8E30 alloy.

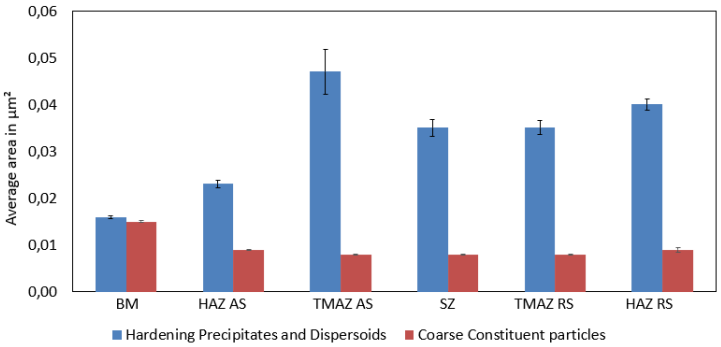

Figure 4.10: Average intermetallics size/area of AA2060 T8E30 alloy.

The AA2060 T8E30 has similar characteristics of intermetallic particles population as the AA2099 T83 alloy. The coarse particles has a decreasing trend from the BM to the SZ and increasing thereon to the HAZ RS (Figure 4.9). The dispersoids and hardening precipitates are the least in TMAZ AS and HAZ RS for this alloy. The BM has the largest population density of the intermetallics compared to the other weld zones.

The coarse particles average area is the largest in BM followed by the HAZ regions, and then the smallest in the SZ and TMAZ regions (Figure 4.10). The trend is more complex for the dispersoids and precipitates. The BM and HAZ AS have very small values for the average intermetallic area, whereas the remaining zones have a much larger average area. These large particles are the dispersoids which occur more near the weld region. The BM and HAZ regions are populated with the hardening precipitates unlike the weld region where the precipitates break down during the FSW process. These precipitates are much smaller in area although distributed with a higher population density. Due to this, the BM and HAZ have a higher population density but lower average area, and the SZ and TMAZ have a higher average area and lower population density.

4.3.4. Mechanical Properties - Micro-hardness of the Weld Joint

The micro-hardness of the AA2099 T83 and the AA2060 T8E30 alloy Base Metal was measured using the Vickers micro-hardness method. The results are recorded in the Table 4.1. It is observed that the AA2060 T8E30 alloy has a much higher micro-hardness value as compared to the AA2099 T83 alloy. These values are used as the standard values to which the hardness of the different weld zones were compared. The measurements were conducted on samples which were at quite a distance from the weld region to avoid the effect of heat which is propagated to a large distance from the weld centre.

Table 4.1: Micro-hardness values of Base Metal of AA2099 T83 & AA2060 T8E30 alloys.

Alloy	Micro-hardness (0.5 HV)
AA2099 T83	122 ± 2.33
AA2060 T8E30	177±1.527

Figure 4.11 is an image of the weld joint sample that was tested for the micro-hardness of each weld zone. Rows 1 and 2 belong to the AA2099 T83 alloy whereas rows 3 and 4 are of the AA2060 T8E30 alloy. The start of these measurements was from the advancing side and is indicated by a line in the image. The total number of indentations were 22 with a distance of approximately 1 mm between 2 indents. This way the micro-hardness of each zone was measured all the way from the BM on the Advancing side to the BM on the retreating side. The various zones of the weld joint are clearly marked in the image. It is important to note that the HAZ region does not have a specific outer boundary, since the dissipation of heat can be towards a larger area. The micro-hardness profiles of each row are shown in the graphs and discussed below.

Figure 4.12 shows the micro-hardness profile of row 1 in the AA2099 T83 alloy. This is the topmost

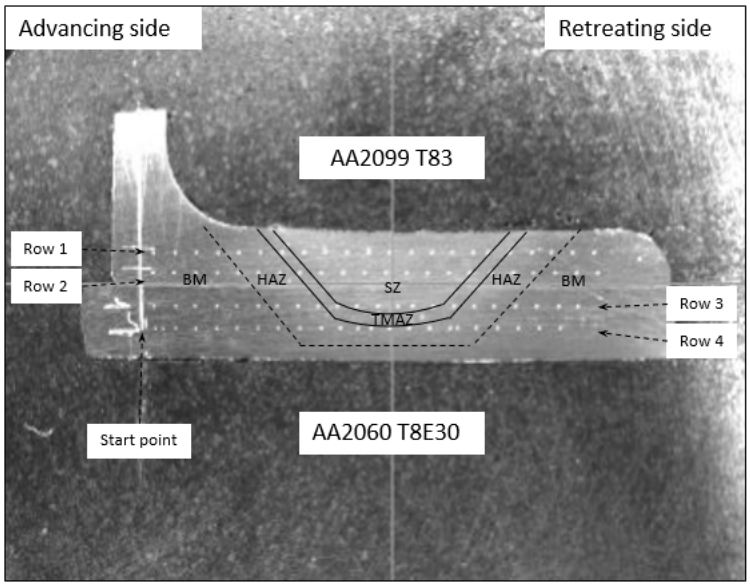

Figure 4.11: Sample of weld joint showing the rows of hardness indentation.

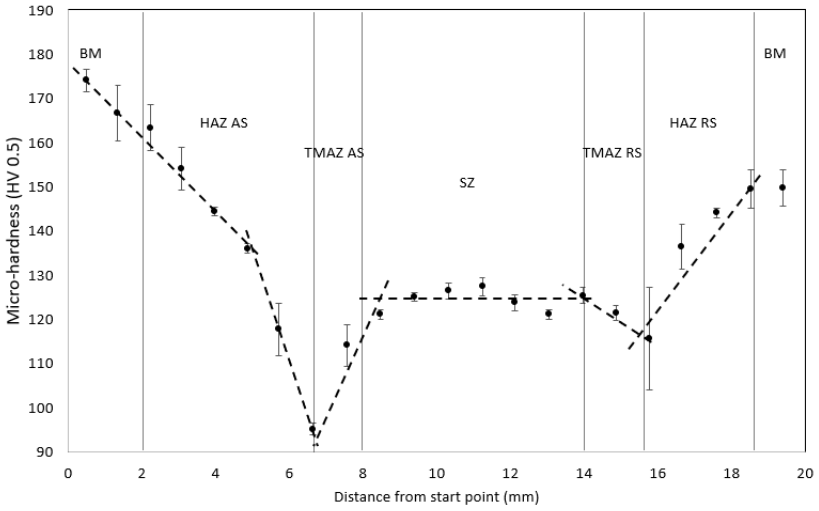

Figure 4.12: Micro-hardness profile of row 1 - AA2099 T83 alloy.

row of the weld joint. This profile has an irregular W-shaped profile of the micro-hardness. The base metal regions of this alloy have a higher micro-hardness value as compared to the one in Table 4.1. This can be attributed to the ageing of the sample post welding process. On the advancing side of the BM the micro-hardness is 174 HV. This is a 42.62% increase than the value obtained earlier. There is a constant decrease throughout the BM and part of the HAZ AS after which is a steep decrease to the interface of the HAZ AS and the TMAZ AS regions. This is the lowest value of micro-hardness recorded in the row with a value of 96.9 HV. The TMAZ AS has a slightly higher value than the interface with an upward trend to the SZ of the alloy.The Stir Zone of this row is 6 mm in length and is the largest, as can be seen in Figure 4.11. The hardness values reaches a plateau in this region, with the maximum value 123.33 HV recorded.

On the retreating side, the BM has a recorded value of 149.67 HV, which is quite less than that of the BM at the AS. Again, there is a gradual decrease all throughout the HAZ RS till the interface of the HAZ RS and the TMAZ RS which has a value of 115.67 HV. The TMAZ RS has a slightly higher value

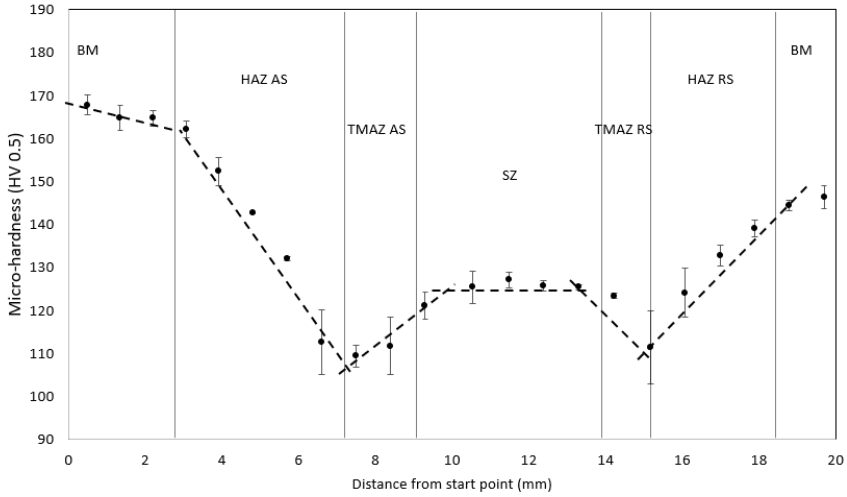

Figure 4.13: Micro-hardness profile of row 2 - AA2099 T83 alloy.

than the interface, but still lower than the SZ.

The 2nd row of micro-hardness measurement of the AA2099 T83 alloy too has a W-shaped profile and is seen in Figure 4.13. The BM here has reported a hardness value of 167.67 HV in the AS and 146.33 HV in the RS. Again, these measurements report a much higher value than the one obtained in Table 4.1. This is an indication that the ageing of the alloy does play a significant role in the hardness of the alloy [64].

The trend from the HAZ AS and the RS is decreasing towards the interface of the TMAZ regions where the lowest values of micro-hardness are recorded as 109.33 and 111.33 for the AS and RS respectively. The TMAZ regions have slightly higher values leading up to the SZ which has a plateau trend here as well. The SZ of this row is 4 mm in length and has a maximum value of 127 HV.

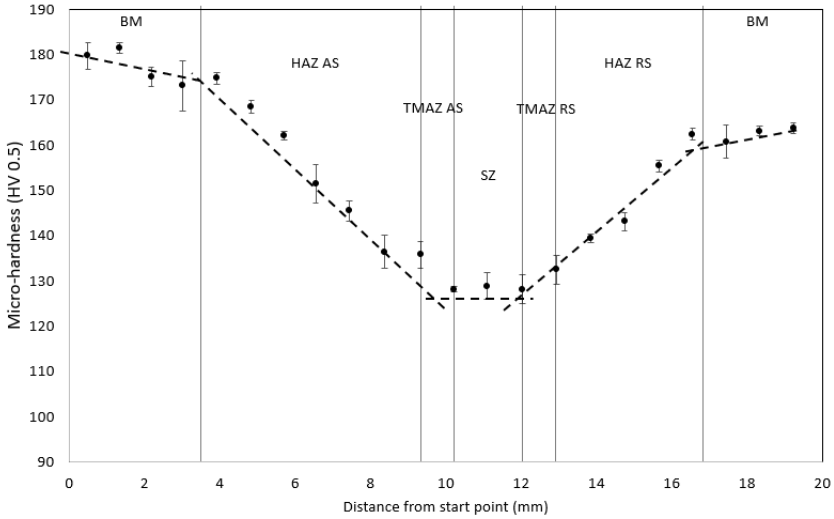

Figure 4.14: Micro-hardness profile of row 3 - AA2060 T8E30 alloy.

Figure 4.14 shows the micro-hardness profile of row 3 in the AA2060 T8E30 alloy. This graph has a V-shaped profile. Here, it is observed that the hardness of BM of the AS is indicative of the measurement recorded in Table 4.1. However, the hardness of BM of the RS region is reduced by 7.6 % with a

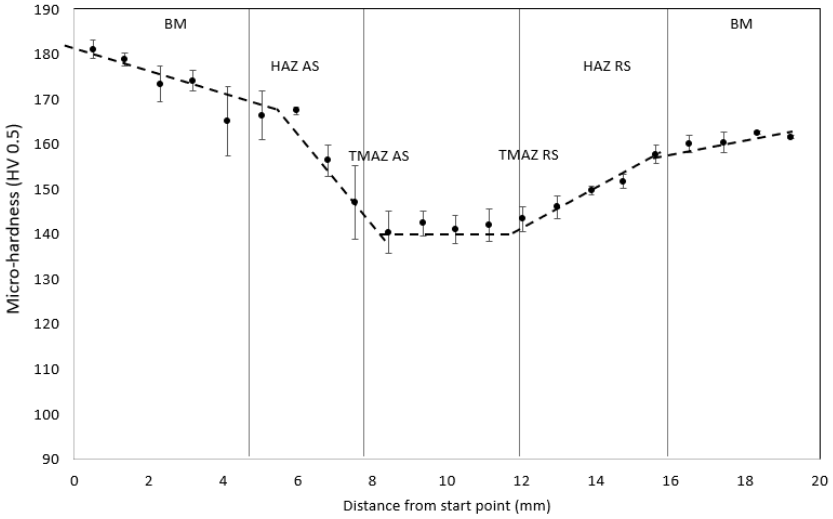

Figure 4.15: Micro-hardness profile of row 4 - AA2060 T8E30 alloy.

value of 163.67 HV compared to the BM which is at a distance from the weld region. There is a linear decrease in trend all the way from the HAZ to the SZ on both sides to a value of 128 HV in the SZ. The SZ of this region is very small in length (3 mm), and has a constant value of 128 HV.

The profile of row 4 of the micro-hardness measurements has been shown in Figure 4.15. This graph also has a V-shaped profile but is irregular in shape. This row runs directly below the SZ of the weld, therefore there is no SZ here. The BM on the AS has a micro-hardness value of 184 HV while that of the RS is 164 HV. This trend is consistent with that of row 3. The trend from the HAZ AS to the TMAZ AS is decreasing with a steep slope till the interface with a value of 140.33 HV, whereas the slope on the RS from the HAZ RS to the TMAZ RS is flatter and records the micro-hardness at the interface with a value of 142 HV. The central region here is entirely the TMAZ region of the AA2060 T8E30 alloy and is seen as a plateau in Figure 4.15.

4.4. Discussion

The Al-Li alloys that are used here have very different microstructures and surface properties. Apart from the elemental constitution of these alloys, the production methods play an important role in determining the properties of the alloys such as grain size and orientation, mechanical properties, and also the electrochemical behaviour [42, 65–67]. The AA2099 T83 alloy was produced by extrusion, which is evident by the grain orientation towards the extrusion direction. In the extrusion process, the grains of the alloy undergo recrystallisation which ultimately results in a smaller grain size [42]. Therefore, the average grain area of the base metal of AA2099 T83 alloy is below 50 μm^2.

The AA2060 T8E30 on the other hand is a cold rolled sheet. This cold rolling elongates the grains up to a large extent giving them a layered structure and resulting in an average grain size of 52792 μm^2, which is approximately 250 times that of the AA2099 T83 BM. This structure of the cold rolled AA2060 alloy was also observed by B. Cai et. al. [2]. These grains are so large that they can be seen clearly in an etched sample even without the use of a microscope (Figure 4.1). It is important to note that cold rolling induces numerous dislocations within the alloy which are later on the sites where the hardening precipitates are pinned [67].

The alloys are thermally treated to produce a stable temper designated as a T8 temper. The T8 designation indicates that the alloy has been solution treated, cold worked for strain hardening , and then artificially aged to achieve precipitation hardening [68]. During cold working, the alloy undergoes deformations inducing dislocations in the matrix. When the alloy is artificially aged, the hardening pre-

cipitates that are formed such as the T_1 phase which are very small in size (200 nm <)[39], locate themselves on these dislocations and on the grain boundaries and thus achieving precipitation hardening of the alloy [69].

The intermetallic particles found in these alloys are of much importance to the mechanical properties and electrochemical behaviour of the alloys. The coarse constituent particles of both the alloys were examined under SEM and EDS. The presence of Al-Cu-Fe-Mn intermetallic particles was confirmed with some particles having a high Cu content while others a lower Cu content. The composition of Cu in wt % varied from 7.5 - 78.9 % in these particles. The presence of these particles was observed by various researchers in the microstructure of both the alloys [35, 39, 70]. For the AA2060 T8E30 alloy, the presence of the S phase (Al_2CuMg) was also confirmed by an EDS analysis on the coarse particles.

The dispersoids and hardening precipitates in these alloys could not be determined under the EDS. This was due to 2 main reasons, firstly because these particles are too small (0.5 μm <) and the resolution of the SEM/EDS was not sufficient to detect these particles, and secondly because most of these particles contain Li which is undetectable by EDS, as mentioned earlier. Reports in literature indicate the presence of the T_1 phase (Al_2CuLi) and the δ' phase (Al_3Li) as the hardening precipitates in the AA2099 T83 alloy [18, 39, 70]. The T_1 phase was also detected in the AA2060 T8E30 alloy [2, 35]. The dispersoids present in these alloys are the β' (Al_3Zr) phase particles which play an important role in recrystallisation and control the grain size of the alloys [2, 18, 35, 39, 70].

During the friction stir welding process, there are 2 factors that induce change in the microstructure of the various weld zones. These are the thermal changes and plastic deformation, both of which are caused by the rotational movement of the tool pin [4]. The heat that is generated during the process aids in the dissolution of hardening precipitates and grain refinement. The plastic deformation from the rotational movement of the tool changes the grain orientation and helps in breakdown of the coarse constituent particles [2]. These factors then have several consequences on the corrosion behaviour of the weld regions.

As the alloys undergo a thermal cycle, recrystallisation occurs in the SZ region of the weld. However this is not the case for the other zones. The dispersoids that are present in the alloy are re-distributed in the stir zone and locate themselves in the grain boundaries [2]. The combination of recrystallisation and presence of dispersoids on the grain boundaries result in very fine grains in the SZ, which is also seen in the work of Rambabu et. al. [5] in their study of the AA2219 alloy. This is observed for both the AA2099 T83 and the AA2060 T8E30 alloys in Figures 4.2 and 4.3. For the AA2099 T83 alloy, the reduction in grain size of the SZ is just around 50 - 55 %, but for the SZ of the AA2060 T8E30 alloy the reduction is around 99.95 % due to the the immense size of the grains in the BM. The increase in heat in the SZ also promotes the dissolution of the hardening precipitates in this zone [32]. Due to this, the hardness of the SZ region drops considerably as compared to the BM of both the alloys, which was seen earlier in the micro-hardness section of the chapter (Figures 4.12 and 4.14).

The TMAZ region has severely deformed grains due to the rotational motion of the tool pin [32]. For the AA2099 T83 alloy, there is a decrease in grain size in the TMAZ zone along with a change in orientation of the grains. In the AA2060 T8E30 alloy, it is observed that the elongated grains that extend to a few millimeters. These grains are only partially deformed in the TMAZ region of this alloy since the zone is quite narrow in width (Figure 4.4). There are very few hardening precipitates remaining in the TMAZ region due to the proximity of this zone to the stir zone which causes the dissolution of the precipitates. This dissolution of hardening precipitates results in a lower micro-hardness of the region. There is however a higher distribution of the coarse constituent particles in this region. When the tool pin rotates and thus generating heat, it pushes the softer/melted material away towards the retreating side. During this phenomenon the coarse particles from the SZ are broken down into smaller particles and are deposited on the TMAZ regions and especially in the retreating side of the alloy due to material flow [32]. Thus, a higher distribution of coarse particles is observed in the TMAZ along with a reduction in the average size of these particles.

The HAZ regions of both alloys have similar microstructures to that of their parent materials, i.e.

the BM. The HAZ regions do not undergo any deformation but they do undergo a thermal cycle. Thus, there is no change in the orientation of the grains but the thermal cycle induces grain refinement in this weld zone [4]. This results in a reduction of the grain size in the HAZ of the AA2060 T8E30 alloy as compared to the respective BM, which is seen in the results section of this chapter. The thermal cycle however induces grain coarsening in the HAZ region of the AA2099 T83 alloy [71]. Thus elongated and recrystallized grains are observed in this zone in Figure 4.2. This also explains why the HAZ AS of the AA2099 T83 alloy has a larger average grain size as compared to the BM of the same alloy (Figure 4.5).

The distribution density of the intermetallic particles in the HAZ regions is quite high. During FSW the rotational movement of the tool pin causes different relative speeds of plastic material on advanced side and retreating side, which affects the material flow, thus resulting in different microstructures on both sides[32]. In the retreating side of the AA2099 T83 weld zones, coarsening of the intermetallic particles was observed due to this (Figure 4.8). Unlike the SZ or the TMAZ, most of the hardening precipitates in this zone were not been dissolved during welding. The regions closer to the TMAZ and SZ have a higher dissolution of the hardening precipitates. As the distance from weld zone is increased on either side, it is observed that the amount of dissolved hardening precipitates in the HAZ keeps decreasing. This is also evident from the micro-hardness profiles of both the alloys. It is known that the micro-hardness of the Al-Li alloys is directly related to the amount of hardening precipitates in the alloy, especially the T_1 phase [4, 6]. Thus, as the TMAZ is approached from the HAZ, there is a huge reduction in micro-hardness due to the increased dissolution of hardening precipitates near the weld centre.

The micro-hardness profile of the weld zones for both the alloys follows a similar trend to the distribution of the hardening precipitates in the respective alloy. However, the dispersoids and the hardening precipitates cannot be distinguished from each other from the SEM images in Figures 4.2 and 4.3. Since these particles are very small (nanometer range), even an EDS analysis of these particles is not conclusive. Therefore, the average size of these particles and population density were evaluated to determine the distribution of the hardening precipitates.

The dispersoids such as the β' (Al_3Zr) phase are generally of the size between 100 - 500 nm, whereas the hardening precipitates such as the T_1 phase found in these alloys, are smaller in size (less than 200 nm)[2, 39]. As mentioned earlier, the hardening precipitates are dissolved during the FSW process in the SZ, TMAZ and partially in the HAZ. Thus, the darker spots that were seen in these regions were mainly dispersoids, which is evident from the average size of intermetallics in Figures 4.8, and 4.10. For the BM, on the other hand, there is a high distribution with a smaller average size of the dark spots indicating that these particles are the hardening precipitates. Therefore, a decreasing trend is observed in the hardening precipitates from the BM towards the TMAZ, which is similar to the micro-hardness profiles of the weld regions of both alloys.

Since the SZ does not have hardening precipitates it should have the lowest micro-hardness. However, this is not the case for either alloy. The lowest micro-hardness values observed were in the interface of the HAZ and TMAZ regions. It is mainly related to the dissolution of strengthening precipitates and also partly due to the coarse grain size induced by thermal effect. Therefore the interface region becomes the weakest zone in terms of micro-hardness [71]. This trend was observed by various researchers in their study of FSW Al-Li alloys [2, 4, 71]

4.5. Conclusion

The microstructural characterisation of the AA2099 T83 and AA2060 T8E30 alloys was performed and evaluated in this chapter. It was observed that the production methods used - extrusion and cold rolling for the respective alloys, had played an important role in the microstructure of these alloys. Large Al-Cu-Fe-Mn intermetallic particles were found in the alloys with both high and low Cu content. S (Al_2CuMg) phase particles were observed in the AA2060 T8E30 alloy matrix. Hardening precipitates were observed in the grain boundaries of the alloys and the larger dispersoids on the surface of the matrix.

The effect of FSW on the microstructure of the weld zones was investigated for both alloys. It was observed that the SZ regions had undergone recrystallisation to obtain fine grains. A decreasing trend in average grain area was observed towards the weld centre. However, coarsening of grains was observed in the HAZ regions of the AA2099 T83 alloy which was suggested to be due to the thermal cycle caused by FSW. A difference in the microstructure characteristics was observed between the advancing and retreating sides due to the rotation of tool pin and material flow during FSW.

The presence of hardening precipitates was not observed in the SZ, and was reduced in the TMAZ and HAZ regions, which suggested the dissolution of these precipitates due to the heat from FSW process. The micro-hardness profiles of the weld zones presented a similar trend to this. Therefore, it was proposed that there is a direct relation between the concentration of hardening precipitates and the micro-hardness of that region. The lowest micro-hardness was observed for the HAZ/TMAZ interface. It was suggested that this was attributed to the coarsening of grain in HAZ and the dissolution of the hardening precipitates, both of which were observed in this chapter.

The distribution of the coarse constituent particles presented a decreasing trend towards the weld centre. These particles were found to be the smallest in the SZ of the AA2060 T8E30 alloy. In a sharp contrast, the coarse constituent particles were found to be much larger in the AA2099 T83 SZ suggesting coarsening of these particles during FSW in this region.

5
Electrochemical Tests

5.1. Introduction

In the previous chapter, the microstructural characteristics of the alloy weld zones were evaluated. It was found that due to FSW, each weld zone had different characteristics from each other. These changes are bound to have some effect on the electrochemical behaviour of the alloys and their kinetics. To determine the correlation between the microstructure and electrochemical behaviour of the AA2099 T83 and AA2060 T8E30 alloys base metals and their respective weld zones, electrochemical methods such as OCP measurements, potentiodynamic polarisation tests, LPR measurements, and SKP tests were performed.

5.2. Materials and Experimental Methods

The samples used for the electrochemical tests were obtained from the as received welded sample of Z-shaped extrusion of AA2099-T83 and cold rolled sheet of AA2060-T8E30 provided by Arconic. All the chemicals used were of analytical grade and provided by Sigma-Aldrich Chemical Company. The sample preparation, experimental set-up and test parameters of the electrochemical experiments are given in chapter 3, section 3.6. The tests were conducted in a freshly prepared 0.1M NaCl aqueous solution of near neutral pH in ambient environment. The experimental set-up of the SKP test is given in section 3.8.

5.3. Results

5.3.1. Open Circuit Potential (OCP) Measurements

Table 5.1: Mean OCP values of the weld zones of AA2099 T83 and AA2060 T8E30 alloys.

Weld Zones	OCP (mV) vs Ag/AgCl	
	AA2099 T83	AA2060 T8E30
BM	-623.18 ± 0.06	-611.91 ± 0.03
HAZ AS	-658.70 ± 0.12	-562.64 ± 0.11
HAZ RS	-611.62 ± 0.05	-652.61 ± 0.09
SZ	-601.27 ± 0.11	-578.08 ± 0.03

Figure 5.1(a) presents the OCP of the selected weld zones of the AA2099 T83 alloy as a function of time over 24 hours of total experiment time in 0.1 M aqueous NaCl solution in ambient environment. It is observed that the SZ has the least negative potential, followed by the HAZ RS, the BM, and then the HAZ AS. Therefore, the nobility of the weld zones from less noble to more noble is in the following order: HAZ AS < BM < HAZ RS < SZ.

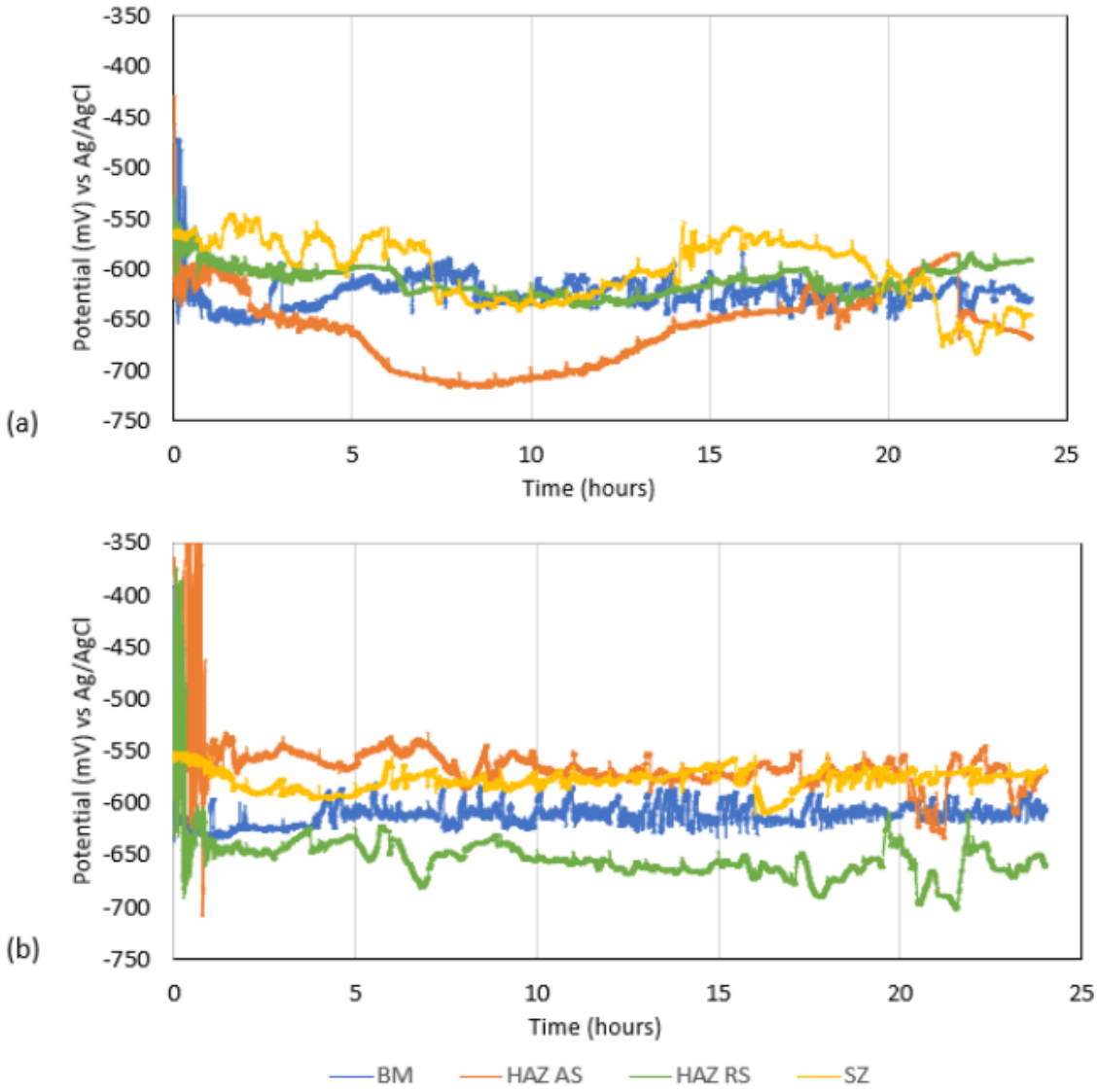

Figure 5.1: OCP measurement as a function of time over 24 hours of total experiment time in 0.1 M aqueous NaCl solution in ambient environment of: (a) AA2099 T83 alloy weld zones, (b) AA2060 T8E30 alloy weld zones.

The OCP of the AA2060 T8E30 alloy weld zones as a function of time is shown in the Figure 5.1(b). Unlike the AA2099 T83 alloy, the weld zones of this alloy present relatively potentials during the test. Here, the least negative potential is of the HAZ AS, followed by the SZ, the BM, and then the HAZ RS. Therefore, the nobility is in the following order: HAZ RS < BM < SZ < HAZ AS.

5.3.2. Potentiodynamic Polarisation Tests

AA2099 T83

The Potentiodynamic polarisation curves of the weld zones of the AA2099 T83 alloy in 0.1 M aqueous NaCl solution in ambient environment are plotted in Figure 5.2(a-d), and the corresponding corrosion potentials E_{corr} and corrosion current density I_{corr} for the HAZ RS and SZ are given in Table 5.2. The corrosion potential and corrosion current density for the BM and the HAZ AS could not be determined by Tafel extrapolation since in both cases corrosion occurs immediately. Due to this, estimations for the corrosion potential were made from the graphs in Figure 5.2(a, b) and are given in Table 5.2. It is observed that the corrosion potential of the SZ is the most negative, followed by the HAZ RS, HAZ AS, and finally the BM.

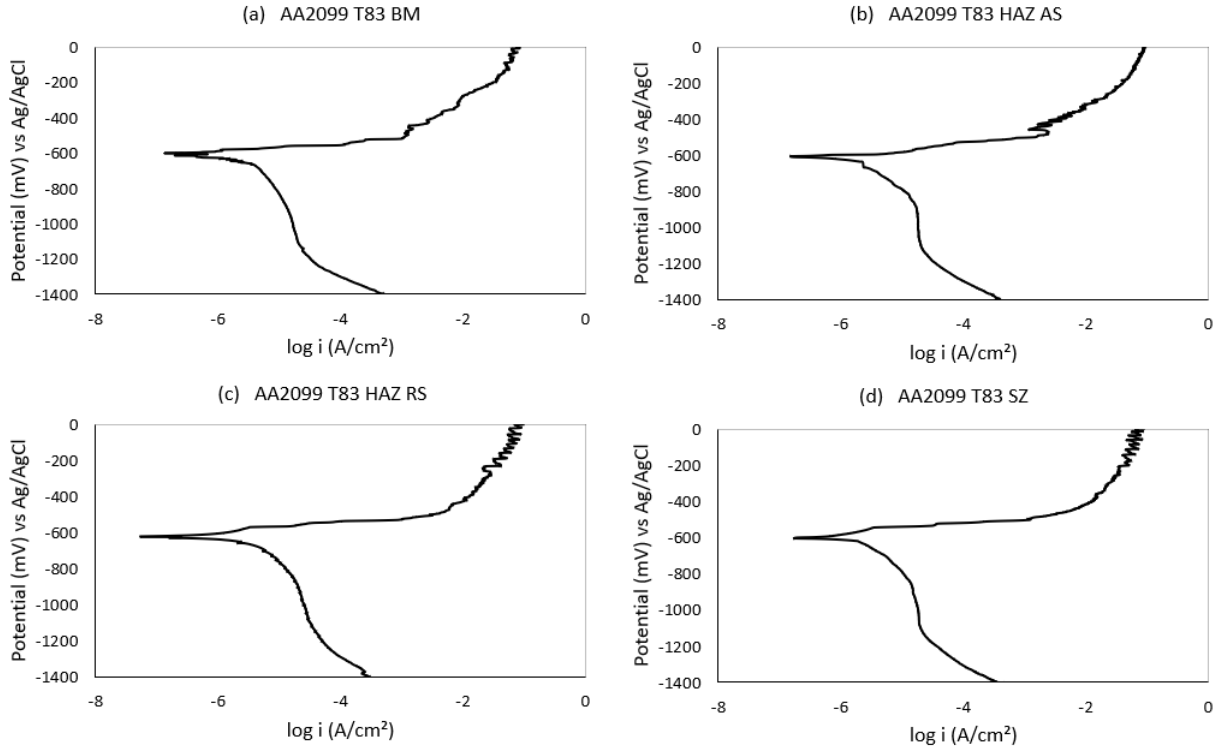

Figure 5.2: Potentiodynamic polarisation curves for the weld zones of AA2099 T83 alloy in 0.1 M aqueous NaCl solution in ambient environment: (a) BM, (b) HAZ AS, (c) HAZ RS, and (d) SZ.

Table 5.2: Corrosion potential (E_{corr}) and corrosion current density (I_{corr}) of the weld zones of AA2099 T83 alloy from potentiodynamic polarisation in 0.1 M aqueous NaCl solution in ambient environment.

Weld Regions	E_{corr} (mV) vs Ag/AgCl	$I_{corr}(\mu A/cm^2)$
SZ	-640.16 ± 23.24	0.201 ± 0.053
HAZ RS	-615.01 ± 12.87	0.118 ± 0.006
HAZ AS	-608	-
BM	-602	-

Although the corrosion current densities of the BM and the HAZ AS could not be extrapolated, it can be estimated by the position of the polarisation curves from the figure. The BM of the AA2099 T83 alloy is located more towards the right side, suggesting that it has a higher corrosion current density, while the HAZ RS curve is more on the left side than the other regions. The HAZ AS and the SZ have similar current densities since they are located relatively close to each other. Thus, the BM has the highest corrosion rate compared to the weld zones of the alloy. This result is explained by the high density of the hardening precipitates such as T_1 phase in the BM (as seen in chapter 4, Figure 4.7). These precipitates are found to be more active than the alloy matrix [30].

The curves from the Figure 5.2 also show the passive behaviour and pitting potentials of each weld zone. This is determined by the anodic branch of the curve. For the BM and the HAZ AS regions of the AA2099 T83 alloy, a defined passive layer is not observed initially. This is indicated by the sudden surge of current within a very small potential range. This is also an indication that for these 2 zones, the pitting potential E_{pit} is close to its corrosion potential E_{corr}. However, there is an indication of passive region formation for both these regions later on around -500 mV vs Ag/AgCl. The polarisation curves of the HAZ RS and the SZ regions of this alloy do show the presence of a passive layer on the surface with distinct pitting potentials at E_{pit} = -573 mV vs Ag/AgCl for the HAZ RS, and E_{pit} = -596 mV vs Ag/AgCl for the SZ.

From the cathodic branch of these graphs, it was determined that all zones have a limited current

density due to oxygen diffusion. This phenomenon is prominent in the SZ ad the HAZ AS of this alloy as the current density remains constant between the potential range of -900 to -1100 mV vs Ag/AgCl. Below this potential there is hydrogen evolution in all the weld zones.

AA2060 T8E30

The potentiodynamic polarisation curves of the AA2060 T8E30 weld regions are shown in Figure 5.3(a-d). Tafel extrapolation was used to estimate the values of the corrosion potential E_{corr} and corrosion current density I_{corr} of the SZ and the HAZ RS. The values are given in Table 5.3. Similar to the AA2099 T83 alloy, the values for the BM and HAZ AS of this alloy could not be determined by Tafel extrapolation, thus estimations for the corrosion potential were made from the graphs and the values are given in the Table 5.3. Here, the most negative corrosion potential is of the SZ, followed by the BM, the HAZ AS, and lastly the HAZ RS.

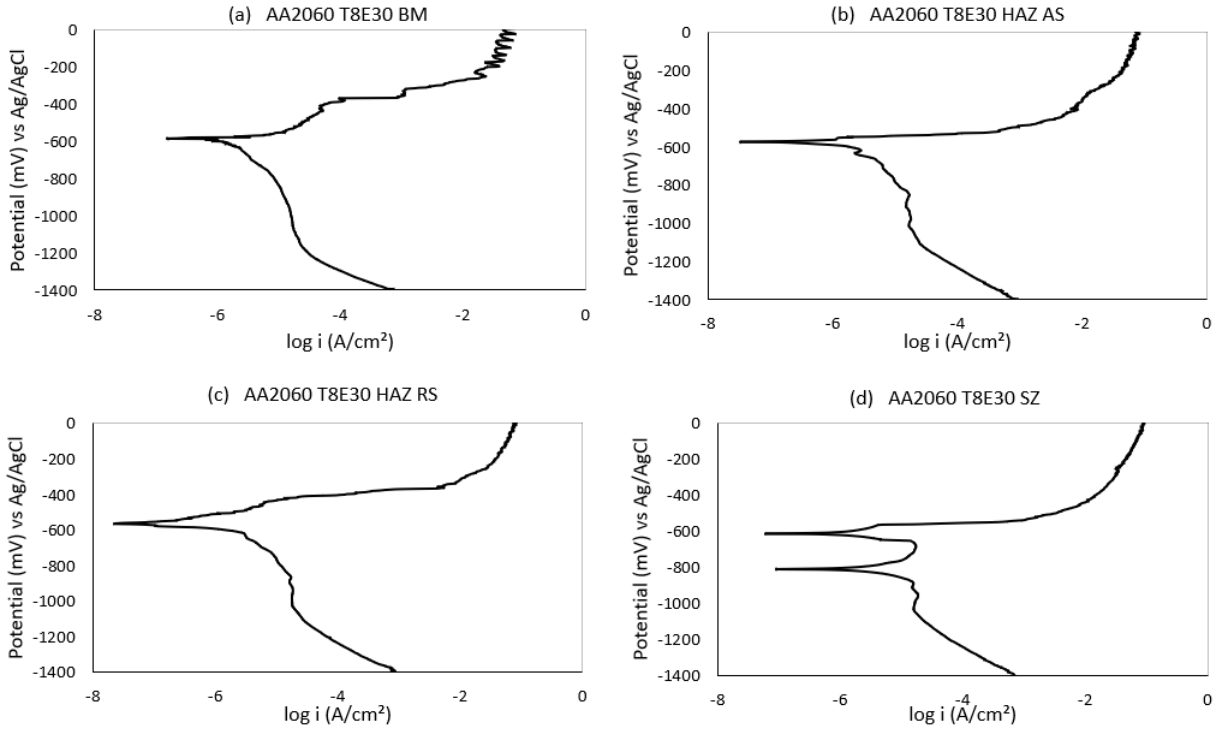

Figure 5.3: Potentiodynamic polarisation curves for the weld zones of AA2060 T8E30 alloy in 0.1 M aqueous NaCl solution in ambient environment: (a) BM, (b) HAZ AS, (c) HAZ RS, and (d) SZ.

Table 5.3: Corrosion potential (E_{corr}) and corrosion current density (I_{corr}) of the weld zones of AA2060 T8E30 alloy from potentiodynamic polarisation in 0.1 M aqueous NaCl solution in ambient environment.

Weld Regions	E_{corr} (mV) vs Ag/AgCl	$I_{corr}(\mu A/cm^2)$
SZ	-622.40 ± 7.94	0.223 ± 0.055
HAZ RS	-570.18 ± 7.66	0.975 ± 0.471
HAZ AS	-573	-
BM	-589	-

The current density is the highest in the HAZ RS since the curve is located towards the right, followed by the HAZ AS, the BM and then the SZ which is located more on the left side. For the HAZ AS, immediate pitting is observed during anodic polarisation with the sudden increase in current. This is similar to the case of the AA2099 T83 HAZ AS. The BM too undergoes immediate pitting, however a passive region is formed soon after, as observed from the Figure 5.3(a). The SZ of this alloy has a

distinct pitting potential of E_{pit} = -568 mV vs Ag/AgCl. This region, similar to the case of AA2099 T83 SZ, does form a passive region which protects the surface from immediate pitting. For the HAZ RS, although not as distinct as the SZ polarisation curve, the pitting potential is -439 mV vs Ag/AgCl.

The AA2060 T8E30 alloy weld zones have limited current density due to oxygen diffusion, similar to the AA2099 T83 alloy. However, for the SZ of this alloy there are 2 corrosion potentials observed in the graph. This will be explained later in the discussion section of the chapter.

5.3.3. Linear Polarisation Resistance (LPR) Measurements

The linear polarisation resistance of the selected zones of both alloys were monitored over a total experimental period of 24 hours in 0.1M NaCl aqueous solution in ambient environment to study the corrosion resistance and its evolution with time. The results are shown in the graphs below.

AA2099 T83

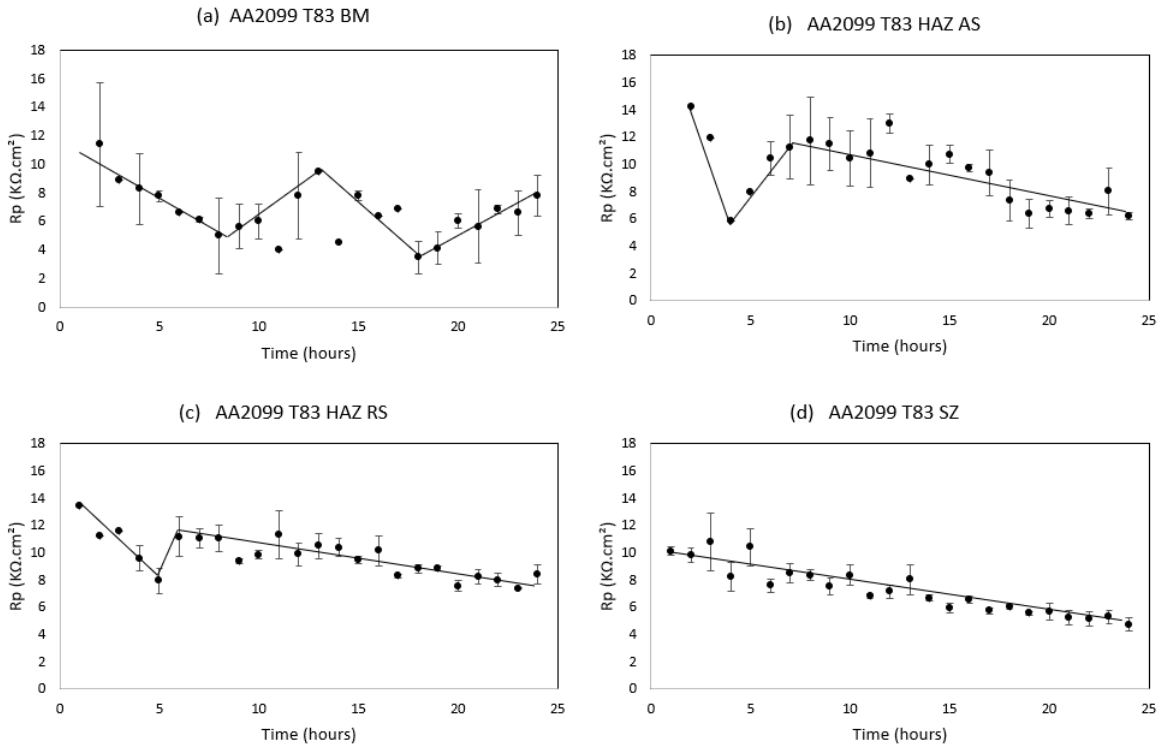

Figure 5.4: LPR measurement as a function of time over 24 hours of total experiment time in 0.1 M aqueous NaCl solution in ambient environment of the AA2099 T83 alloy weld zones: (a) BM, (b) HAZ-AS, (c) HAZ-RS, (d) SZ.

Figure 5.4(a-d) shows the resistivity of the weld zones of AA2099 T83 immersed in a 0.1M NaCl solution. It is observed that for all the weld zones of this alloy, the trend of corrosion resistance is to decay with time, however for the BM there is a slight increase towards the end. The initial resistivity of the zones are also quite similar and within the range of 10 - 14 $K\Omega.cm^2$. It is also observed that both the HAZ regions of this alloy have a higher resistivity than the BM and the SZ. The BM initially has a high resistivity, but it decreases drastically once the experiment starts. The SZ, on the other hand, has the least resistivity amongst all the zones and has a larger decay over the 24 hours of immersion.

The resistivity of the BM of the AA2099 T83 alloy is shown in the Figure 5.4(a). After 1 hour of immersion, the initial resistivity was measured to be 11.3 $K\Omega.cm^2$. A decreasing trend was observed till 7 hours of the experiment after which there was an increase for 5 hours suggesting the formation of a passive region on the surface of the sample. Again a decreasing trend was seen for 3 hours followed

by an increasing trend till the end of the experiment at 24 hours with a final resistivity of 7.8 $K\Omega.cm^2$. Figure 5.4(b) shows the resistivity of the HAZ AS of the AA2099 T83 alloy. Here, the initial resistivity is 14.22 $K\Omega.cm^2$ at 1 hour immersion, after which there is a sudden decrease which indicates the breakdown of the passive region. After 3 hours of immersion, there is an increase in resistivity for 4 hours of immersion). As the test continues, there is a gradual decreasing trend observed with a final resistivity of R_P = 6.4 ± 0.3 $K\Omega.cm^2$ at 24 hours.

The HAZ RS has the highest polarisation resistance compared to the other weld zones of the alloy, as seen in Figure 5.4(c). Here, the initial polarisation resistance has a value of 13.4 $K\Omega.cm^2$ at 1 hour of immersion. Initially, there is a small decrease for 5 hours following a peak value suggesting the instability of the passive layer. This is followed by a gradual decreasing trend that continues till the end of the experiment at 24 hours. The SZ of the alloy has the lowest polarisation resistance compared to the other zones of the AA2099 T83 alloy. From the graph in Figure 5.4(d), it is apparent that there is a gradual decrease in resistivity all throughout the experiment till 24 hours of the total experimental time.

AA2060 T8E30

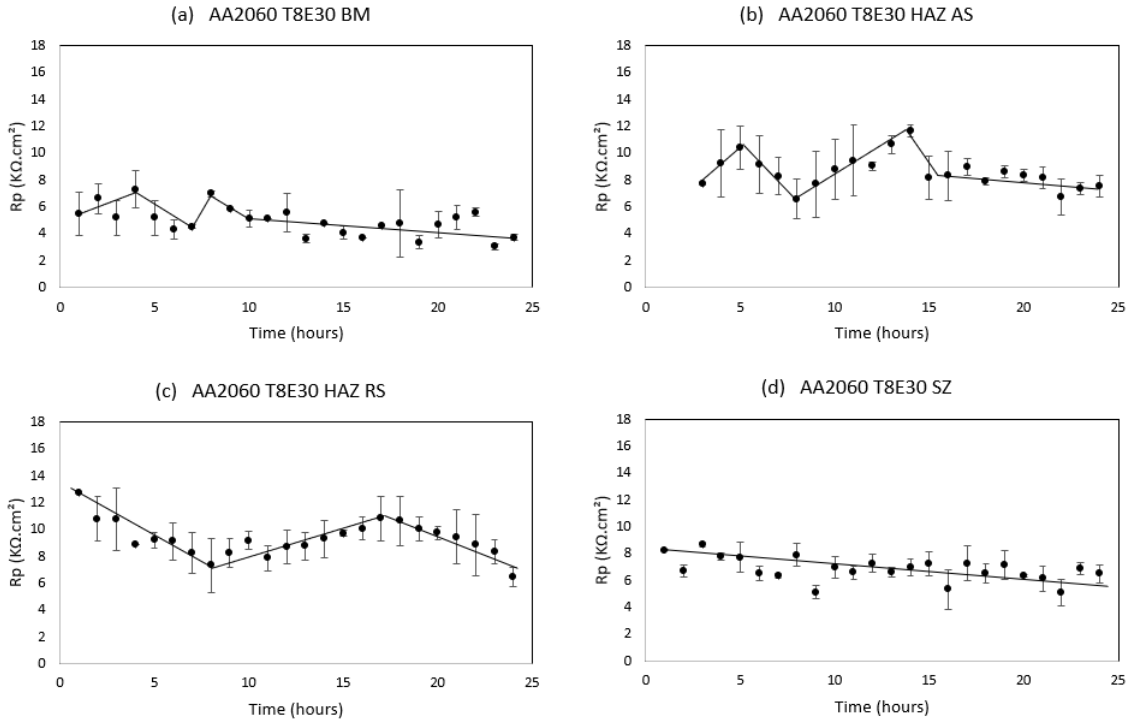

Figure 5.5: LPR measurement as a function of time over 24 hours of total experiment time in 0.1 M aqueous NaCl solution in ambient environment of the AA2060 T8E30 alloy weld zones: (a) BM, (b) HAZ-AS, (c) HAZ-RS, (d) SZ.

The polarisation resistance of the weld zones of the AA2060 T8E30 alloy are shown in Figure 5.5. It is observed that the initial resistivity of this alloy is lower than that of the AA2099 T83 alloy. Again the HAZ regions have a higher resistance here, followed by the SZ and then the BM.

The BM of the AA2060 T8E30 alloy has the lowest polarisation resistance. Figure 5.5(a) shows the LPR graph for the BM of this alloy. The initial resistivity of this zone is 5.49 $K\Omega.cm^2$. Initially there is an increase in resistivity for 3 hours followed by a decrease for the next 3 hours. However, after 8 hours of the experiment, a decreasing trend in resistivity was observed for the base metal of this alloy.

The HAZ regions seems to be the most resistant zones of the alloy, as can be seen from the LPR graph in Figure 5.5(b, c). For the HAZ AS, the initial polarisation resistance is 7.73 $K\Omega.cm^2$, after which it increases till 5 hours of immersion possibly due to a passive region formation. A number of fluctua-

tions are observed in this region, which could suggest the simultaneous breakdown and formation of the passive region in this weld zone. After 15 hours there is a slight decreasing trend till the end of the experiment with a value of 7.5 ± 1 $K\Omega.cm^2$ at 24 hours. The HAZ RS region has fewer fluctuations than the HAZ AS of this alloy. The initial polarisation resistance of this zone is the highest with a value of 12.72 $K\Omega.cm^2$. A gradual decrease in resistivity is observed till 8 hours followed by an increasing trend till 17 hours of immersion. After this a decreasing trend is observed all through the experiment till the end.

The trend of the polarisation resistance of the SZ of AA2060 T8E30 alloy (Figure 5.5(d)) is similar to that of the AA2099 T83 SZ. The SZ of both the alloys has a trend of constant decay with time. The initial resistivity of this weld zone is 8.26 $K\Omega.cm^2$ after which a slight decreasing trend of resistivity is observed for the entire experimental time of 24 hours.

5.3.4. SKP

The surface potential of the base metals of AA2099 T83 and AA2060 T8E30 alloys were measured using SKP at 0 % relative humidity at room temperature. These values are given in the Table 5.4. It is observed that the AA2060 T8E30 alloy BM has a slightly higher surface potential than the AA2099 T83 BM.

Table 5.4: Surface potential of the base metal of AA2099 T83 and AA2060 T8E30 alloys measured under SKP.

Alloy	Surface Potential (mV)
AA2099 T83 BM	408 ± 10.0
AA2060 T8E30 BM	426 ± 11.2

The weld region for the as-received sample, as seen in Figure 5.6, was scanned under the SKP to obtain the surface potential map of the sample. Figures 5.7 and 5.8 show the surface potential of the scanned region in millivolts. The lowest potentials correspond to areas of anodic activity whereas the less negative potentials are cathodic regions on the surface.

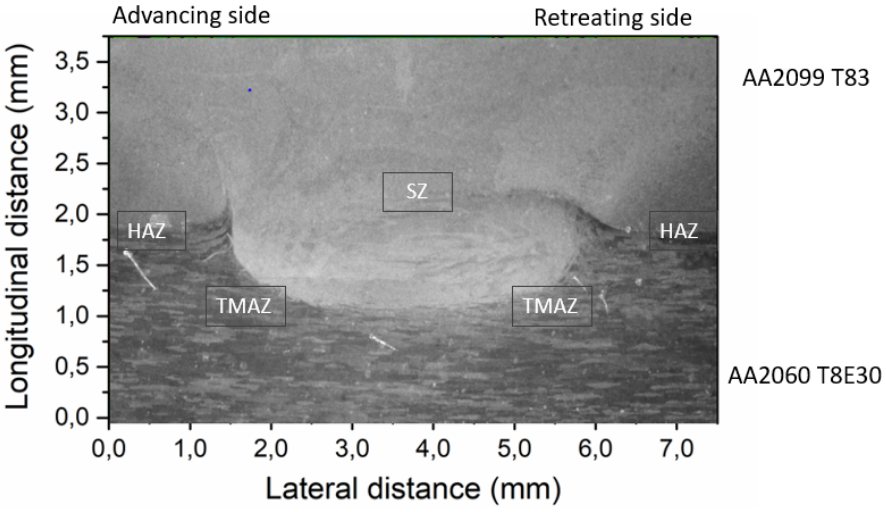

Figure 5.6: Weld region of the sample scanned under SKP.

From the Figure 5.7, it is observed that there is a considerable difference in the surface potential between the SZ of 2 alloys. The SZ of the AA2099 T83 alloy has a surface potential of around 200 mV less than the AA2060 T8E30 alloy, suggesting that the AA2099 T83 region is anodic whereas the

AA2060 T8E30 region is more cathodic in nature. In the AA2099 T83 alloy, the surface potential of the surface is relatively consistent with the measurement of the bm, as seen in Table 5.4. Towards the interface of the TMAZ RS and the SZ in this alloy, a small region which has a more negative surface potential compared to the rest of the surface is observed with a surface potential of -550 to -620 mV. This region, which is highly active, is located very close to the more noble AA2060 T8E30 SZ. Thus, it is bound to induce some galvanic effect between the 2 regions.

For the AA2060 T8E30 alloy, it is observed that the SZ region has the least negative surface potential and this decreases towards all directions in the alloy gradually, as observed in Figure 5.8. Although there is quite some difference in the surface potential between the weld zones here, the gradual decrease shows that the effect of galvanic corrosion within these regions will not be severe.

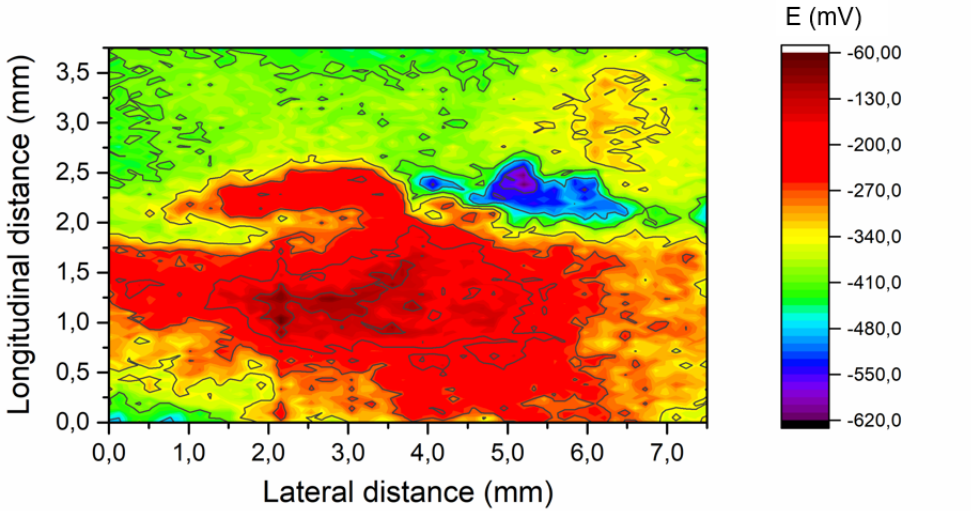

Figure 5.7: SKP surface potential map for the weld region of the sample.

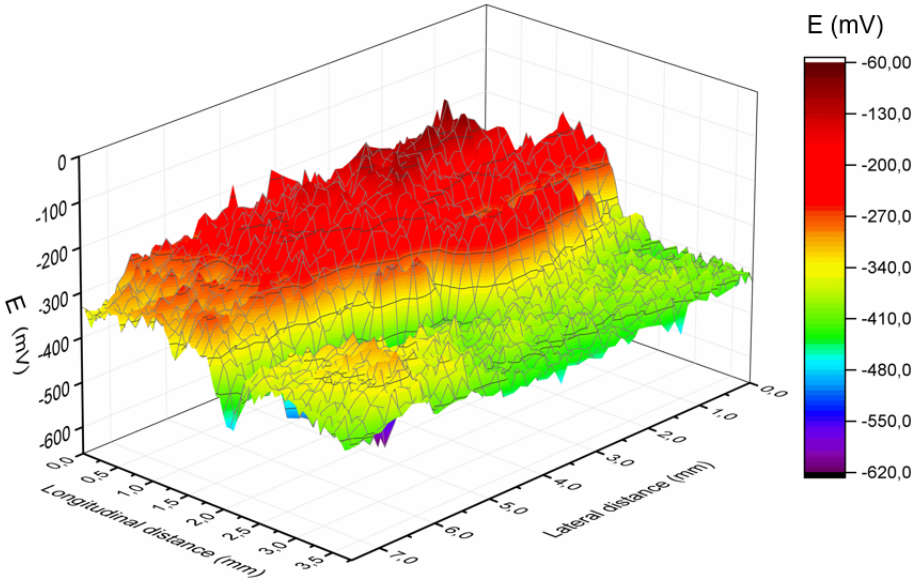

Figure 5.8: SKP surface potential topography map for the weld region of the sample.

5.4. Discussion

The Electrochemical tests performed on the alloys give an insight into various details of their corrosion behaviour such as the corrosion kinetics, passivity and the electrochemical behaviour of the alloy among other things. The electrochemical behaviour of the alloys depends on several factors such as the intermetallic particles and phases and even the production methods of the alloy [26, 30, 35].

The tendency of each weld zone to corrode was observed in the open circuit potential measurements. Of the 2 alloys, the AA2099 T83 alloy was identified as the more active alloy. This is due to the high lithium content in this alloy (Table 3.1). However, the difference in potential between the 2 alloys is not a large one (10 to 20 mV). This is attributed to the cold rolling process that the AA2060 T8E30 alloy has undergone during production, which induces dislocations and enhance precipitation hardening [67]. This makes the AA2060 T8E30 alloy quite active as well. The OCP measurements of the AA2060 T8E30 alloy present a relatively stable potential over the 24 hours of immersion, but the graph for the AA2099 T83 show that there are several peaks and valleys indicating that for this alloy there is a simultaneous formation and a breakdown of the passive regions.

For both the alloy weld zones, the SZ regions presented the least negative potential values thus exhibiting the highest nobility. This is mainly due to the absence of the highly active lithium containing T_1 phase hardening precipitates in this zone due to dissolution during FSW [2, 3, 6]. The electrochemical behaviour of the HAZ zones is not consistent with both alloys or even in the AS and RS of the same alloy. This is due to the difference in distribution and average size of the intermetallic particles in these regions [2], which is also seen in the previous chapter. To understand the kinetics of these zones, anodic and cathodic polarisation tests were carried out on each weld zone individually for both the AA2099 T83 and AA2060 T8E30 alloys.

The potentiodynamic polarisation curves are used to determine the passive behaviour, the pitting potentials, the rate of corrosion, and other corrosion kinetics of the alloys. From the weld zones, the SZ of both the alloys show a similar passive behaviour for a very small potential range, after which there is an immediate breakdown due to pitting at their respective pitting potentials. However, this passive behaviour is not as prominent in the other weld regions of either alloy or even in the base metals. This is due to the dissolution of the T_1 phase in the SZ [5]. All the other regions have immediate pitting when the polarisation starts as seen by the sudden surge in corrosion current density in the graphs. This effect is more pronounced in the AA2099 T83 alloy zones due to the active nature of the alloy. In the AA2060 T8E30 alloy weld regions, although pitting is immediately observed in each zone, the BM and HAZ RS of this alloy show some passivity after the initial breakdown. According to Urushino et. al. [72], when Al alloys undergo ageing, some of them exhibit 2 pitting potentials which correspond to the pitting in grain boundaries and pitting in the alloy matrix. The preferential pitting occurs at the grain boundaries, which is observed by the initial surge in current density in the polarisation graph (Figure 5.3(a)). The second abrupt increase in the current density corresponds to pitting in the alloy matrix [72].

The AA2060 T8E30 SZ exhibits 2 corrosion potentials in the potentiodynamic polarisation test (Figure 5.3(d)). This behaviour was observed in all 3 repetitions of the experiment. The exact reason for this behaviour is not known, however it could be suggested that this is due to the interaction of the alloying elements from the AA2099 T83 and AA2060 T8E30 alloys, since the SZ here is a mixture of both these alloys. This causes a higher rate of cathodic reactions in the AA2060 T8E30 alloy SZ, which is also observed from the SKP surface potential map in Figure 5.7. However, it is important to note that the SKP measurements were performed in a non-chloride environment, thus the results cannot be used to determine the activity in a chloride environment.

The corrosion resistance of the weld zones was determined by linear polarisation resistance tests over a period of 24 hours. Initially, the AA2099 T83 alloy has a higher resistance to corrosion compared to the AA2060 T8E30 alloy. However, towards the end of the experiment the resistivity of both the alloy weld regions are within 4 - 8 $K\Omega.cm^2$. The general trend for the resistivity was to decrease with time for both the alloy weld zones. The HAZ regions of both alloys presented higher resistivity than the SZ or the BM of the corresponding alloy. This was due to the distribution of the highly active T_1 precipitates in the HAZ regions [6, 32]. Although they are present here, the distribution density of these particles

are much less here than that of the base metal (Figures 4.7 and 4.8), thus the HAZ regions exhibit a slightly higher resistivity than the BM. This also explains the initial reduction of the resistivity of the HAZ regions. The T_1 precipitates are possibly attacked first since they are highly active [20], thus causing a reduction in the resistivity of the alloys weld zones. Additionally, it was also observed that the SZ regions of both the alloys presented a gradual decreasing trend in resistivity throughout the experiment and there are no sudden fluctuations in this trend. This is attributed to the absence of strengthening precipitates in the SZ caused due to the thermal cycle from the welding process [2].

5.5. Conclusion

The electrochemical behaviour and kinetics of corrosion of the AA2099 T83 and AA2060 T8E30 alloys weld regions were investigated in this chapter. From the OCP tests, it was observed that the AA2099 T83 alloy was the more electrochemically active alloy. The nobility of the weld zones of the AA2099 T83 alloy was in the order: SZ > HAZ RS > BM > HAZ AS, and that of the AA2060 T8E30 alloy was in the order: HAZ AS > SZ > BM > HAZ RS.

The corrosion rates were determined by the potentiodynamic polarisation tests. For the AA2099 T83 weld zones, the corrosion rate follows the order: HAZ RS < HAZ AS $\simeq$ SZ < BM , and for the AA2060 T8E30 alloy: SZ < BM < HAZ AS < HAZ RS, from lowest to highest corrosion rates. It was also observed that only the SZ regions of both alloys exhibited a distinct passive behaviour. Therefore, it was suggested that due to the absence of the T_1 precipitates, the SZ regions of the alloys were the least prone to corrosion attack.

The resistivity of the weld zones of both alloys over 24 hours in a chloride environment was evaluated. For the BM and HAZ regions, fluctuations were observed in the resistivity values. It was proposed that this was attributed to the presence of the highly active T_1 precipitates in these regions which are attacked immediately on immersion. The SZ regions did not show these fluctuations, thus suggesting that the corrosion attack in the SZ was controlled by the coarse constituent particles whereas the T_1 phase precipitates were responsible for the corrosion attack of the BM and HAZ regions of the AA2099 T83 and AA2060 T8E30 alloys.

6

In-Situ Immersion Testing

6.1. Introduction

The in-situ immersion test is based on the novel technique by Sullivan et. al. [62]. These tests were conducted to determine the localised corrosion attack and its behaviour in the microstructure of the welded sample. This chapter was then related to the microstructure to determine the preferential attack phases and the type of corrosion attack in the weld zones of the alloy. The kinetics of corrosion from the previous chapter were also evaluated along with the in-situ immersion tests to obtain an in-depth understanding of the localised corrosion behaviour of the FSW alloy sample.

6.2. Materials and Experimental Methods

The samples used for the in-situ immersion testing were obtained from the as received welded sample of the Z-shaped extrusion of AA2099-T83 and cold rolled sheet of AA2060-T8E30. All the chemicals used were of analytical grade and provided by Sigma-Aldrich Chemical Company. Sections of the as-received sample were cut perpendicular to the welding direction to obtain cross-sectional samples of the entire welded region in 4.5 mm x 23.5 mm rectangular coupons.

The standard sample preparation for the in-situ immersion tests is given in chapter 3. The tests were conducted in a 0.1 M NaCl aqueous solution of near neutral pH at room temperature in ambient environment. Scanning electron microscope (SEM) images of the alloy were taken after corrosion testing and after desmutting using SEM in secondary electron mode to further investigate the initiation sites for corrosion within the microstructure. Energy dispersive x-ray spectroscopy (EDS) elemental mapping and area analysis of the microstructure of the alloy was carried out to assess distribution of the alloy components within the various phases.

6.3. Results

6.3.1. AA2099 T83

Base Metal (BM)

Figure 6.1 shows the exposed area of the AA2099 T83 base metal at various intervals of the in-situ immersion testing. The first image, (a), is the exposed area right before immersion. Here, it is observed that the large coarse constituent particles are located on the matrix and the smaller hardening precipitates are bound to the grain boundaries and dislocations.

The formation of corrosion rings starts after 15 minutes of immersion in 0.1M NaCl solution, and are distinct in Figure 6.1 (b). There are 2 corrosion rings located within close proximity to each other. The larger corrosion ring has a radius of 122.1 μm, whereas the smaller one has a radius of 36 μm. It is also observed that the area around the coarse particles start to darken along with the grain boundaries. This suggests the initiation of corrosion due to galvanic activity within and around the particles.

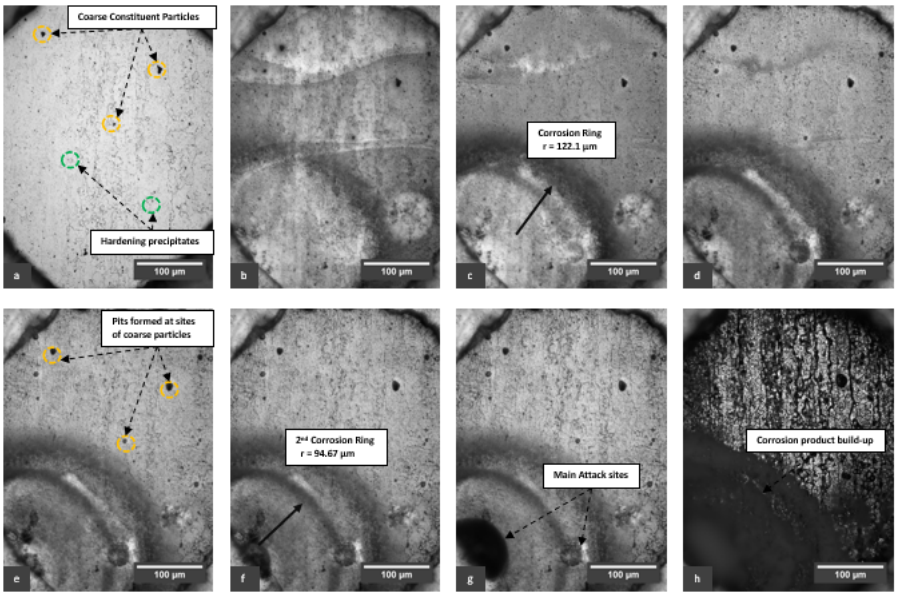

Figure 6.1: In-situ Immersion Test of AA2099 T83 BM in a freshly prepared 0.1 M NaCl aqueous solution in ambient environment: (a) Before immersion, (b) 30 mins immersion, (c) 1 hour immersion, (d) 1 hr 30 mins immersion, (e) 2 hrs immersion, (f) 2 hrs 30 mins immersion, (g) 3 hrs immersion, (h) After 24 hrs immersion.

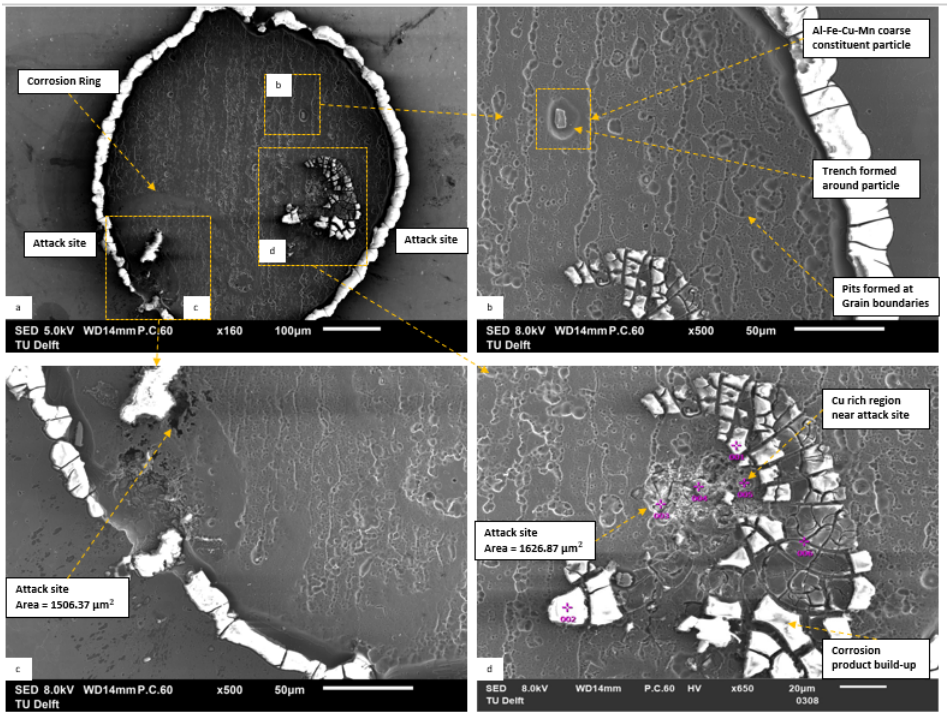

Figure 6.2: SEM images of exposed area of In-situ immersion test sample for AA2099 T83 BM (a) Entire exposed region, (b) Region around coarse constituent particle, (c & d) Attack sites.

After 90 minutes of immersion , Figure 6.1(d), there are clear attack sites located within the corrosion rings. These attack sites have corrosion product/ oxides deposit on them, causing them to appear darker than the surface. The sites of the coarse constituent particles also show the formation of pits and their propagation at this point. There is a 65-75 % increase in the areas of the coarse particles confirming the propagation of pits. After 2 hours of immersion, Figure 6.1(e), a number of attack sites are formed within the larger corrosion ring forming their smaller corrosion rings. A huge amount of corrosion product build up settles on these attack sites. The grain boundaries are also attacked by this

point due to the presence of hardening precipitates located there.

The ex-situ image after 24 hours of immersion, Figure 6.1(h), shows the grain boundaries attacked and the coarse particle sites increased in area by 110 % compared to the original sites. In this image, the main attack sites cannot be seen at all due to the heavy build-up of corrosion products.

The SEM images of the exposed area of AA2099 T83 BM after desmutting with 30% HNO_3 are seen in Figure 6.2. There are a number of features in this area that are observed here. These are magnified and shown in the images (b-d). In Figure 6.2(b), the large coarse particle was found to be an Al-Fe-Cu-Mn intermetallic, confirmed by EDS analysis on the particle. This particle had trenching all around it with the region rich in Cu content. An intergranular attack was also observed with pits formed at grain and sub-grain boundaries. This indicated corrosion attack on both the coarse particles and hardening precipitates.

The attack sites are seen in Figure 6.2(c, d). The attack site has an area of 1506.37 μm in (c), and an area of 1626.87 μm in (d). These attack sites are covered with corrosion product, which can be seen as the huge bright spots in and around these regions. This was confirmed by an EDS analysis on these sports revealing high oxide concentration there. The area surrounding these attack sites were found to be rich in Cu content compared to the surface matrix. Numerous smaller cavities and pits are also observed in the grain boundaries.

Heat Affected Zone (HAZ)

HAZ-AS

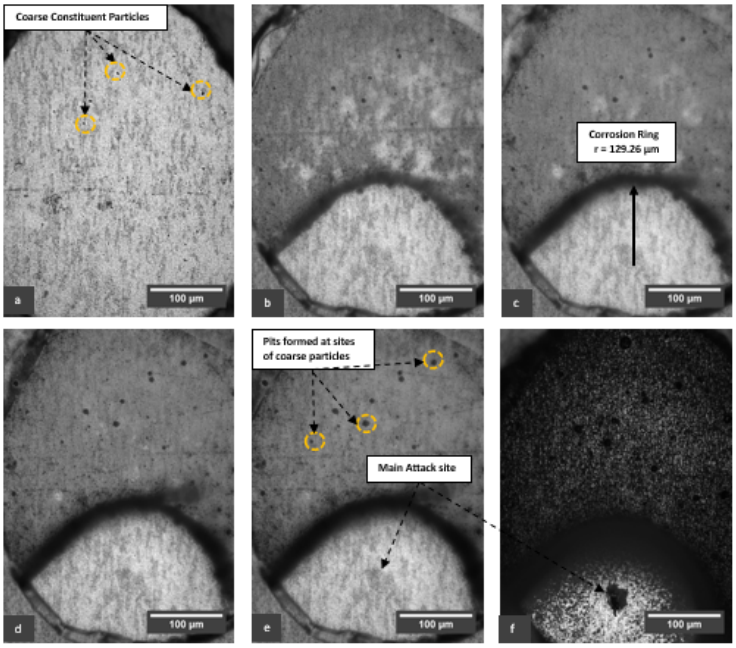

Figure 6.3: In-situ Immersion Test of AA2099 T83 HAZ-AS in a freshly prepared 0.1 M NaCl aqueous solution in ambient environment: (a) Before immersion, (b) 1 hour immersion, (c) 1 hr 30 mins immersion, (d) 2 hrs immersion, (e) 2 hrs 30 mins immersion, (f) After 24 hrs immersion.

The in-situ immersion testing of the AA2099 T83 HAZ AS is represented by the images in Figure 6.3. Image (a) shows the total exposed area which undergoes testing, which has a diameter of d = 0.5mm. Here, the coarse constituent particles are clearly visible on the matrix of the alloy. The hardening precipitates cannot be particularly distinguished from the grain boundaries due to their size in nanometers. Once the sample is immersed, a corrosion ring starts forming within 15 minutes. However, a distinct ring is only formed after 30 minutes of immersion in the electrolyte, with a radius of r = 118.3 μm.

After an hour of immersion, Figure 6.3(b), the sites of the coarse particles darken around them suggesting the initiation of localised corrosion there. The corrosion ring increases in size up to a radius of r = 129.26 μm after 90 minutes of immersion in Figure 6.3(c). At this interval, it is also observed the centre of the corrosion ring starting to darken, indicating the location of the main attack site. This attack site becomes apparent after 2 hours of immersion.

The sites of the coarse constituent particles show large pits that have formed after 2 hours of immersion in Figure 6.3(d). These sites are as large as 60 μm^2 in area and get even bigger up to 74.86 μm^2 after 2 hours and 30 minutes of immersion. Towards the end of the immersion testing, there is severe corrosion product build-up at the edge of the corrosion ring which darkens the entire surface. Thus, the sample was desmutted from corrosion products and analysed under the SEM. This is seen in the Figure 6.4.

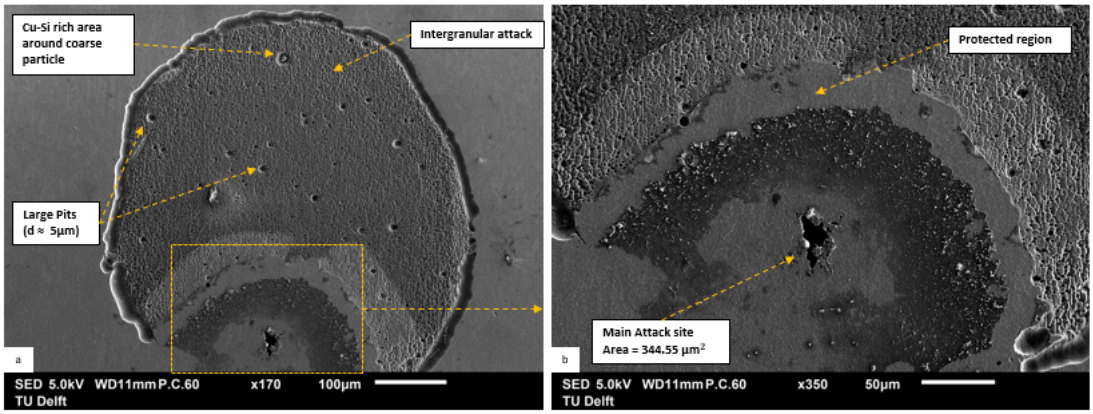

Figure 6.4: SEM images of exposed area of In-situ immersion test sample for AA2099 T83 HAZ-AS (a) Entire exposed region, (b) Main attack site.

The Figure 6.4 shown above, reveals a number of details of the immersion testing of the AA2099 T83 HAZ AS. There is severe intergranular attack on the surface of the alloy with small circular pits on these grain boundaries. This suggests the dissolution of the hardening precipitates located here. There are large pits with an average size of d = 5 μm, at the sites of coarse particles. However, some coarse particles rich in Cu are still attached to the surface with trenches around them. These trenches have a high concentration of Cu and Si, which was confirmed by an EDS analysis of this region. This indicates the selective dissolution of the particles which cause the more active elements to corrode away, leaving the nobler Cu in these regions.

The main attack site has been magnified and shown in Figure 6.4(b). This attack site has an area of 344.55 μm^2. There is a protected region around the attack site which represents the location of the corrosion ring seen in Figure 6.3(b-f). On the edge of this protected region, there are several large pits high in Cu content, representing the sites of the coarse constituent particles. The bright spots within the corrosion ring are the oxide products attached to the surface of the alloy in a thin film. Here, the intergranular and inter-subgranular attack of the alloy surface is observed closely.

HAZ-RS

The intervals for in-situ immersion testing of the AA2099 T83 HAZ RS are seen in Figure 6.5(a-f). The first image shows us the exposed area of the weld joint, which is of radius r = 0.5 mm. Here, the coarse constituent particles on the surface are also observed. These particles are larger than those in the HAZ AS, with an average area of 0.011 μm^2 as compared to 0.009 μm^2 of the HAZ AS. There is a larger distribution of the coarse particles particles in this region. Within 10 minutes of immersion there is a formation of a corrosion ring. This ring is formed completely within 30 minutes of immersion and has a radius of r = 91.21 μm, as can be seen in Figure 6.5(b). From the centre of the corrosion ring, there is an intense evolution of H_2 gas, indicating localised corrosion occurring at the region. This gas evolution is continued upto an hour of immersion along with the darkening of the corrosion ring.

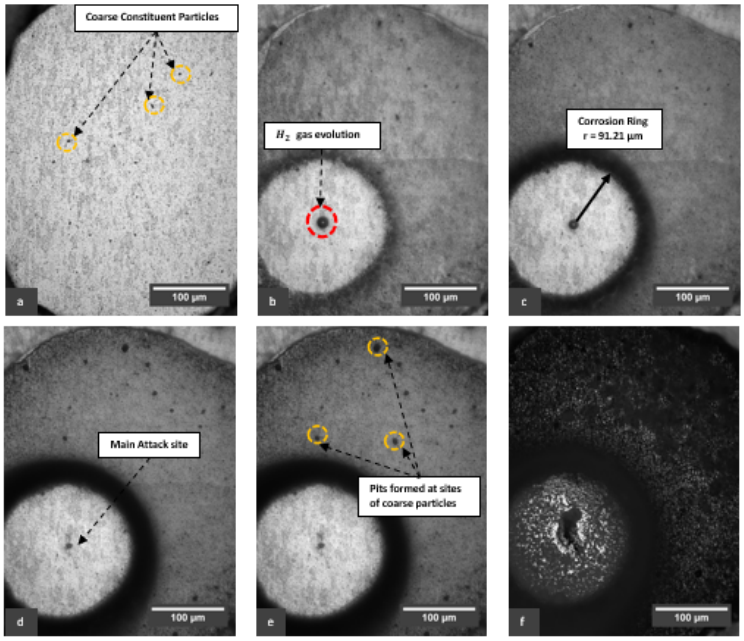

Figure 6.5: In-situ Immersion Test of AA2099 T83 HAZ-RS in a freshly prepared 0.1 M NaCl aqueous solution in ambient environment: (a) Before immersion, (b) 30 mins immersion, (c) 1 hr immersion, (d) 2 hrs 30 mins immersion, (e) 3 hrs immersion, (f) After 24 hrs immersion.

After 2 hours and 30 minutes of immersion, it is observed that a number of pits have initiated outside the corrosion ring on the surface of the sample. The sites of coarse particles have also darkened in colour due to corrosion product from activity in those regions. The area of these sites has increased 4 - 5 times as compared to the original size. The main attack site is now visible at the centre of the corrosion ring as a dark circle. In Figure 6.5(f), the main attack site has grown to a large extent, covered and surrounded by corrosion product build-up which forms a thick layer all over the surface.

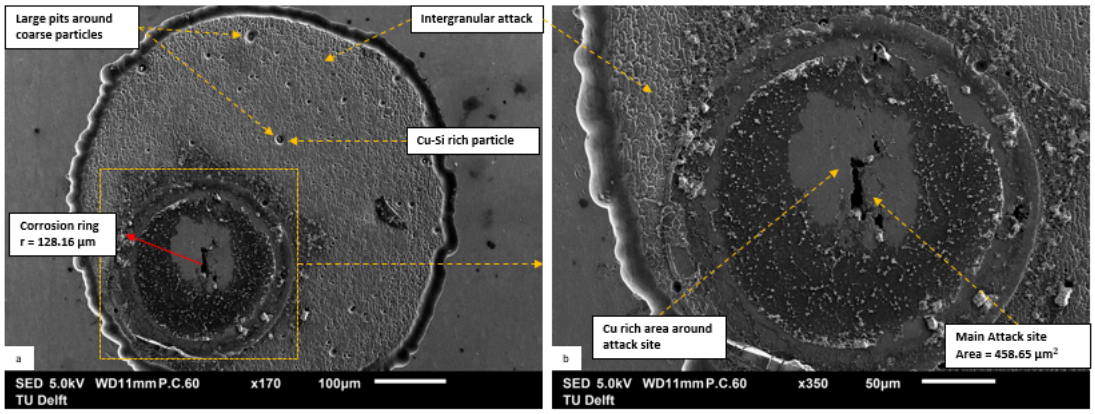

Figure 6.6: SEM images of exposed area of In-situ immersion test sample for AA2099 T83 HAZ-RS (a) Entire exposed region, (b) Main attack site.

The SEM images after the desmutting of the AA2099 T83 HAZ RS weld zone are shown in Figure 6.6, to give a deeper understanding of the corrosion mechanism occurring here. The corrosion ring is seen clearly without the oxide build-up on top of it. It has a radius of r = 128.16 μm, which is larger than what was seen in Figure 6.5. There are large pits and trenches around the coarse constituent particles which are rich is Cu and Si concentration. The RS here, shows more pits and cavities compared to the AS of the HAZ. This is due to the larger population density of these particles in this zone. The trenches

were revealed to have high concentration in Cu, similar to the AS region.

Figure 6.5(b) is a magnification of the main attack site within the corrosion ring of this sample. The total area of the main attack site is 458.65 μm^2, which is larger than that of the AS but much smaller compared to the BM of the alloy. The interface region within the corrosion ring and outside the main attack site is a protected region which is covered in a thin layer of oxide build-up from corrosion products. The attack outside the corrosion ring appears to be intergranular and inter-subgranular in nature, keeping consistency with the AS of the HAZ zone of this alloy.

Stir Zone (SZ)

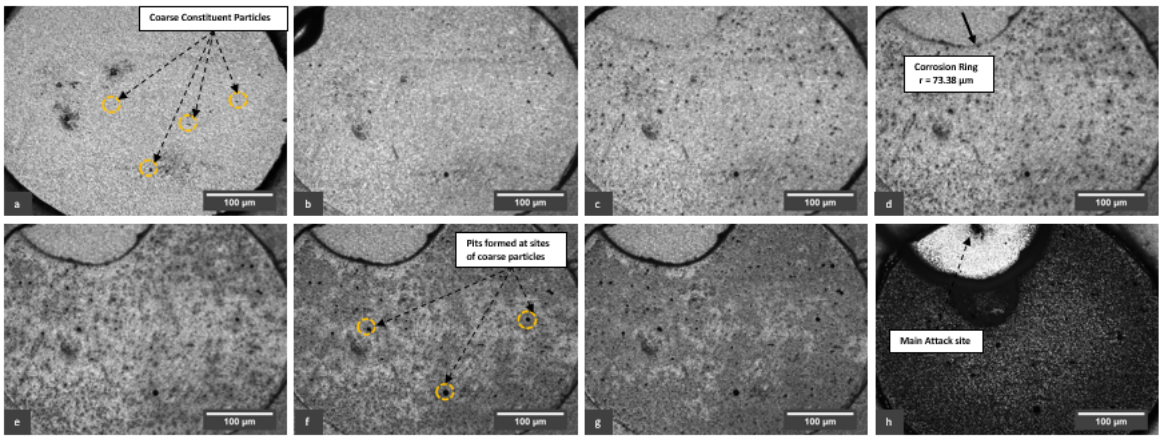

Figure 6.7: In-situ Immersion Test of AA2099 T83 SZ in a freshly prepared 0.1 M NaCl aqueous solution in ambient environment: (a) Before immersion, (b) 30 mins immersion, (c) 1 hour immersion, (d) 1 hr 30 mins immersion, (e) 2 hrs immersion, (f) 2 hrs 30 mins immersion, (g) 3 hrs immersion, (h) After 24 hrs immersion.

The SZ, which is the centre region of the weld, was tested under in-situ immersion testing and the various intervals for the immersion test are shown in Figure 6.7(a-h). The coarse particles can be seen as the large dark particles on the exposed matrix surface. The smaller dark particles here are dispersoids, which were added during the welding process to modulate the grain size after recrystallisation. As it is observed, the corrosion activity in this region is quite slow, with the corrosion ring forming after 1 hour of immersion. In images (c-d) there is a huge number of pit initiation on the surface. However, not all pits propagate and thus the pit density reduces within 2 hours of immersion.

The corrosion ring has a radius of r = 73.38 μm, which is the smallest of any weld region. The region inside the corrosion ring is protected up to the main attack site, which is revealed only towards the end of the test in Figure 6.7(h). The pits and cavities formed are numerous and distributed all over the surface but are small in size. After 24 hours of immersion, Figure 6.7(h), the main attack site and the corrosion product build-up at the edge of the corrosion ring were observed.

Figure 6.8 shows the SEM images of the AA2099 T83 SZ after desmutting following the immersion test. There are numerous small pits all over the surface with the diameter of these pits ranging from d = 0.1 - 1.5 μm. Large pits are present at the sites of coarse constituent particles with their radius as large as r = 8 μm. These are very few in number within the exposed area.

The main attack site is shown in Figure 6.8(b). It is located almost on the edge of the exposed area and has an area of 1469.25 μm^2. The bright spots surrounding this attack site are the presence of oxide products. The region between the attack site and the corrosion ring is the protected region where there is no indication of any localised attack. An important observation in the immersion testing of this zone is that there is no intergranular attack in this zone. This can be attributed to the absence of hardening precipitates in the zone, which locate themselves on grain boundaries and dislocations. The hardening precipitates of this zone have been dissolved during the FSW process, leaving the grain

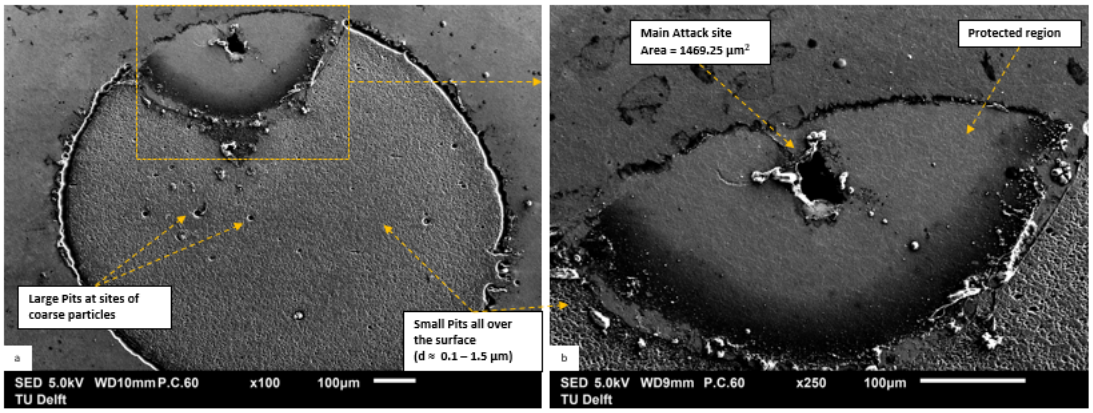

Figure 6.8: SEM images of exposed area of In-situ immersion test sample for AA2099 T83 SZ (a) Entire exposed region, (b) Main attack site.

boundaries free from galvanic activity and therefore the absence of intergranular attack.

6.3.2. AA2060 T8E30

Base Metal (BM)

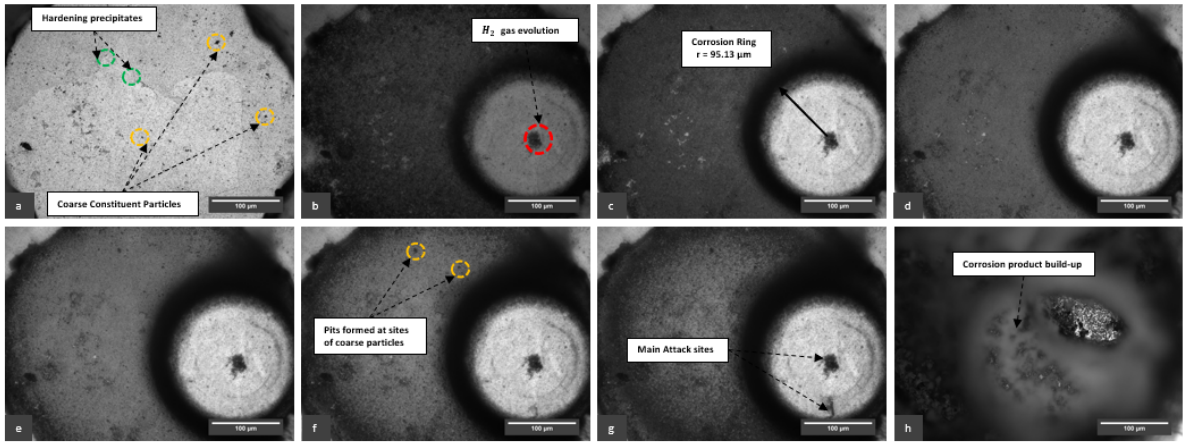

Figure 6.9: In-situ Immersion Test of AA2060 T8E30 BM in a freshly prepared 0.1 M NaCl aqueous solution in ambient environment: (a) Before immersion, (b) 30 mins immersion, (c) 1 hour immersion, (d) 1 hr 30 mins immersion, (e) 2 hrs immersion, (f) 2 hrs 30 mins immersion, (g) 3 hrs immersion, (h) After 24 hrs immersion.

The base metal of the AA2060 T8E30 alloy was tested under in-situ immersion testing in 0.1M NaCl solution. The various intervals of the immersion test are shown in the images (a-h) in Figure 6.9. Here, Figure 6.9(a), the large grains of the cold rolled alloy are observed. The hardening precipitates are located on the grain boundaries of this alloy as small dark spots. The larger dark spots have been identified as coarse constituent particles in the matrix of the alloy. immediately after immersion, the corrosion ring forms within a few minutes. This is accompanied by H_2 gas evolution from the centre of the corrosion ring. The corrosion ring here has a radius of r = 95.13 μm with a main attack site in the centre, as is seen in Figure 6.9(c).

The corrosion ring increasingly gets darker as immersion is continued. However, it is observed that the upper side of the corrosion ring has accumulated more corrosion products over a larger area in Figure 6.9(f). The sites of coarse particles have also enlarged and formed pits and cavities due to local activity here. At the edge of the corrosion ring on the lower side, the formation of another attack site

is observed, which continues to grow in Figure 6.9(g). Towards the end of the immersion test after 24 hours, there is nothing visible due to the intense build-up of a thick layer of corrosion products on the surface of the alloy.The sample was then removed and studied under SEM.

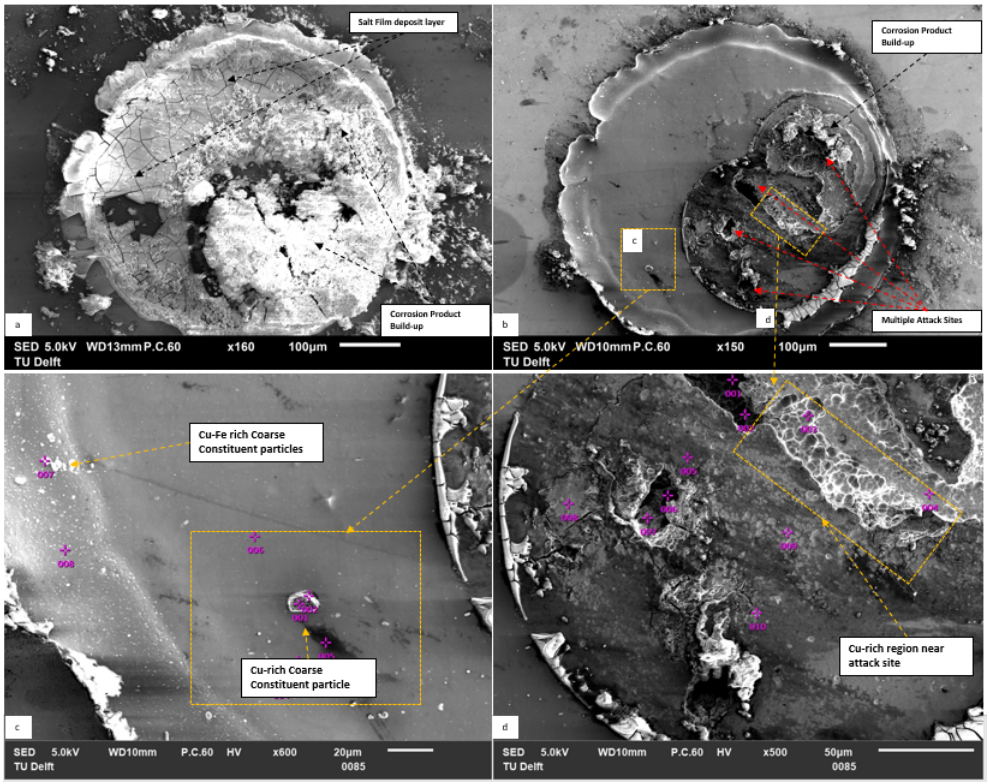

Figure 6.10: SEM images of exposed area of In-situ immersion test sample for AA2060 T8E30 BM (a) Entire exposed region before de-smutting, (b) Entire exposed region after de-smutting (c) Region around coarse constituent particle, (d) Attack sites.

Figure 6.10 are the SEM images of the AA2060 T8E30 alloy BM after immersion test. Image (a) shows the sample untreated after the test. Here the intense corrosion product build up on the site of the main attack site and the corrosion ring are observed. The rest of the surface is covered with a thin film of salt deposit. This sample was then desmutted in 30 % HNO_3 solution to remove the salt film and the corrosion products. The result is seen in Figure 6.10(b).

In Figure 6.9(b), it is clearly seen that there are not 1 but 2 corrosion rings on the surface of the alloy. These corrosion rings are accompanied with multiple attack sites in them. The second corrosion ring was not visible under the optical microscope due to the corrosion products covering the region. There are a total of 4 main attack sites within these overlapping corrosion rings with their sizes ranging from 157.22 μm^2 - 1662 μm^2 in area. There is still some residual corrosion product on the edges of the exposed surface even after desmutting of the sample. Images c and d of this Figure are magnified regions of the exposed area in image b.

An EDS analysis on the bright particles in Figure 6.10(c) reveal that they are mainly Cu rich coarse particles with Fe or Mn along with traces of Mg in them. However, there seems to be no trenches or cavities around these particles, suggesting a uniform corrosion on the exposed surface outside of the corrosion ring. Figure 6.10(d) is a magnification of the interface of the 2 corrosion rings where they overlap. There are indications that intergranular attack connects the main attack sites. The region next to the main attack site was revealed to have a very high concentration of Cu with as much as 11.23 % of total Cu concentration in this region. This indicates the possibility of selective dissolution of either the matrix or the intermetallic particles, leaving the nobler Cu on the surface.

Heat Affected Zone (HAZ)

HAZ-AS

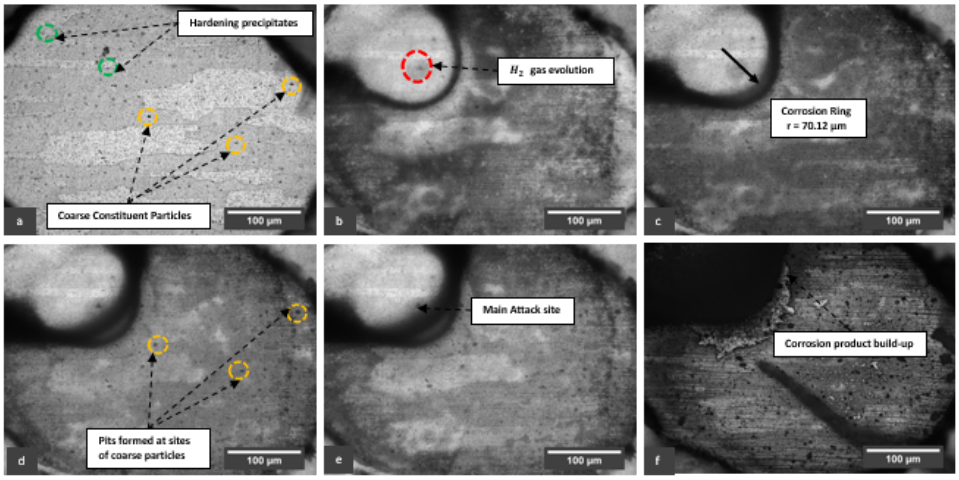

Figure 6.11: In-situ Immersion Test of AA2060 T8E30 HAZ-AS in a freshly prepared 0.1 M NaCl aqueous solution in ambient environment: (a) Before immersion, (b) 30 mins immersion, (c) 1 hour immersion, (d) 2 hrs immersion, (e) 3 hrs immersion, (f) After 24 hrs immersion.

The exposed area with a diameter of d = 0.5 mm of the HAZ-AS of AA2060 T8E30 alloy has been shown in Figure 6.11(a). The grains here are flat and have a pancaked structure, similar to the base metal of the alloy. However, they are much smaller in size due to their proximity to the weld joint. The hardening precipitates are situated in the grain boundaries and the dislocations of the alloy, whereas the coarse particles are located freely on the matrix. Within 10 minutes of immersion of the sample, a corrosion ring is formed with a radius of r = 70.12 μm. From the centre of the corrosion ring, there is an evolution of H_2 gas suggesting that this is the region of the main attack site. This region progressively gets darker with time indicating the continuation of localised attack in this site. Another feature observed is that the grains are selectively attacked which is indicated by the intensity of the colour here. The lighter phased grains seem to be nobler than the others and hence corrode at a later stage of the immersion test.

The formation of pits can be observed in Figure 6.11(d) at the sites of the coarse constituent particles. The area surrounding these particles get larger by a factor of 2 to 3 times, unlike the weld zones of the AA2099 T83 alloy where the factor is between 4-7 times that of the original area. This indicates that the coarse particles are not as active in the weld zone of this alloy. There is an inward darkening of the corrosion ring as the immersion carries on after 2 hours, indicating the build up of corrosion products on the surface. Figure 6.11(f) shows the surface of the sample after 24 hours of immersion. Here, the entire corrosion ring is covered with a dark layer of corrosion products. The numerous pits on the surface outside the corrosion ring is also observed here. Most of these pits are located right at the grain boundaries, as seen in Figure 6.11(a), where there is a high concentration of the hardening precipitates.

The SEM images of the desmutted AA2060 T8E30 HAZ-AS sample are shown in Figure 6.12. As observed in the BM, there are still corrosion products embedded to the main attack site of the exposed area. The main attack site is enclosed within the corrosion ring. Outside the corrosion ring there are a number of pits and cavities formed. These are few in number and distributed all over the surface of the matrix. The presence of trenches around coarse particles are also confirmed. Other than these features, the region outside the corrosion ring has a uniform surface which indicates the possibility of uniform corrosion here.

The main attack site within the corrosion ring is magnified and shown in Figure 6.12(b). Here, the type of attack observed is intergranular and it is quite large as well with a length of l = 173.96 μm. This intergranular attack is due to the hardening precipitates in the grain boundaries which undergo galvanic

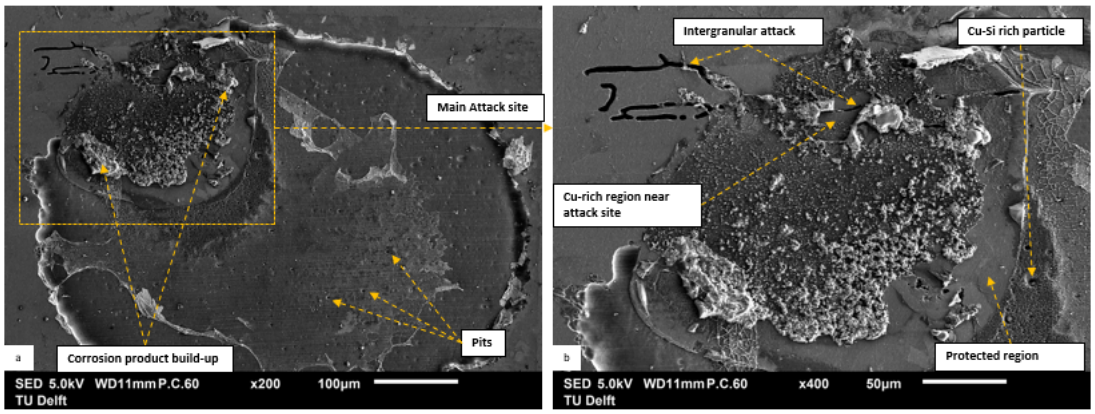

Figure 6.12: SEM images of exposed area of In-situ immersion test sample for AA2060 T8E30 HAZ-AS (a) Entire exposed region, (b) Attack site.

activity. This attack also allows for the propagation of the electrolyte outside of the exposed area, which is why the intergranular attack continues outside up to 100 μm in length. The bright spots covering the attack was revealed to be oxide products on the surface. The regions in proximity to the attack were rich in Cu content which further solidifies the argument for dissolution of the hardening precipitates. On the edge of the corrosion ring, trenches or pits formed around Cu-Si rich coarse particles due to the dissolution of the matrix by nobler elements of these coarse particles.

HAZ-RS

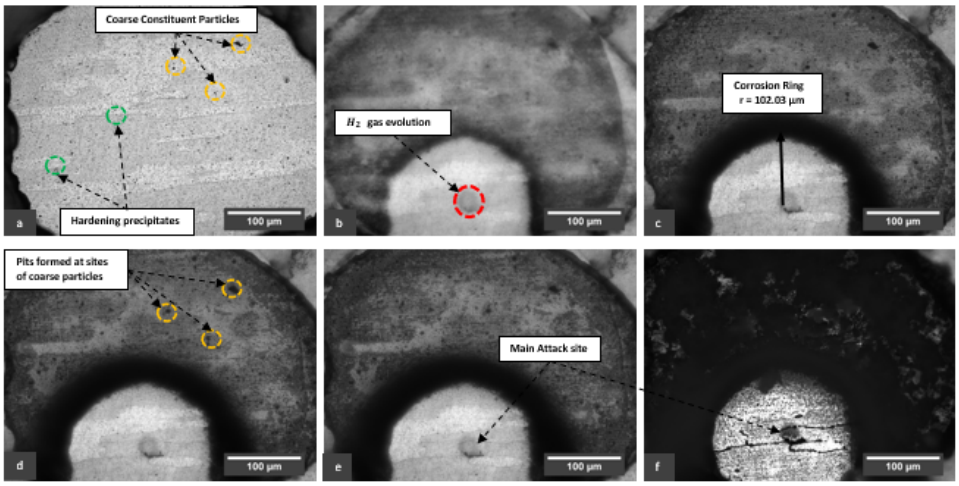

Figure 6.13: In-situ Immersion Test of AA2060 T8E30 HAZ-RS in a freshly prepared 0.1 M NaCl aqueous solution in ambient environment: (a) Before immersion, (b) 30 mins immersion, (c) 2 hrs immersion, (d) 2 hrs 30 mins immersion, (e) 3 hrs immersion, (f) After 24 hrs immersion.

The HAZ-RS of the AA2060 T8E30 weld joint was tested under similar conditions for in-situ immersion test. Figure 6.13 shows the intervals of the immersion test before, during and after immersion. Image (a) shows the region exposed for this test before immersion. Here it is observed that the grains of this region are smaller compared to the HAZ-AS region, however the intermetallic particles and their location in this region are similar to the HAZ-AS. Once immersed, the corrosion ring forms rapidly within 5 minutes followed by H_2 gas evolution, as can be seen in Figure 6.14(b). Again, the grains here are selectively attacked with the dark phase grains attacked first.

The corrosion ring has a radius of r = 102.3 μm with the main attack site located right at the centre of it. Figure 6.13(d , e) show the numerous pits formed in the region outside the corrosion ring. The large pits are mainly around coarse constituent particles in the alloy. The smaller pits are scattered all

around the exposed surface. In 6.13(e), it is clearly seen that the main attack site is an intergranular attack within the corrosion ring, extending from one end to the other. the region outside the corrosion ring is mostly hidden by a deposit of corrosion products. To get a better understanding of the kinetics, the sample was desmutted in 30 % HNO_3 solution and studied under the SEM.

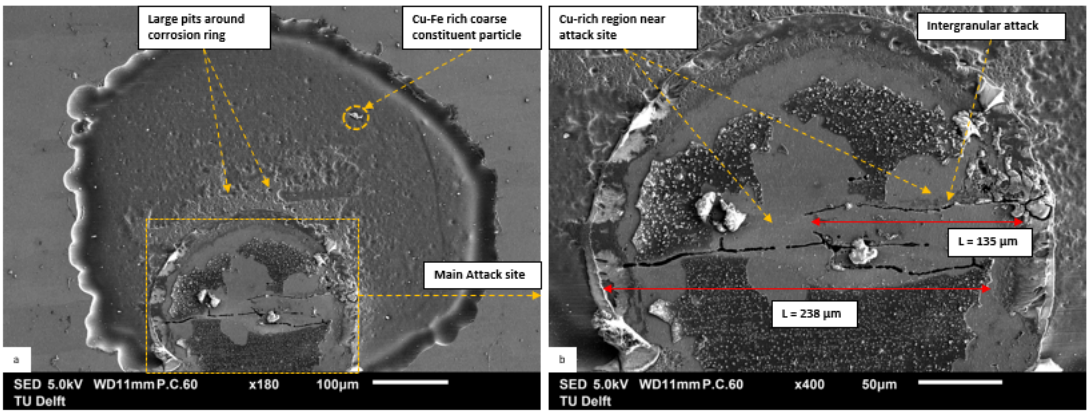

Figure 6.14: SEM images of exposed area of In-situ immersion test sample for AA2060 T8E30 HAZ-RS (a) Entire exposed region, (b) Attack site.

In Figure 6.14(a), it is observed that most of the corrosion product which was present on the surface has been removed by desmutting. The surface shows numerous pits and cavities on the surface due to the higher density of hardening precipitates present here. There are very few trenches in this region, which can be attributed to the smaller size of the coarse constituent particles compared to that of the HAZ-AS. These coarse particles are mainly Cu-Fe rich particles. Another important observation is the presence of numerous large pits on the outer interface of the corrosion ring.

The type of attack within the corrosion ring is intergranular attack, similar to the HAZ-AS. This is magnified and shown in 6.14(b). These attacks are large in size, ranging from 135 μm to 238 μm in length. However, this type of attack stops right before the corrosion ring. The region between this attack and the corrosion ring is largely protected and covered with a very thin layer of corrosion product build up on the surface, as confirmed by an EDS analysis on these particles. The region next to the attack is high in Cu content, which is in consistency with the results from the HAZ-AS region of the alloy.

Stir Zone (SZ)

The various intervals for the in-situ immersion test of AA2060 T8E30 SZ are shown in Figure 6.15(a-f). The exposed surface is seen in image a of the figure. The surface has a dense population of dispersoids, which are seen as small dark spots. The larger particles here are the coarse constituent particles in the matrix. Within 10 minutes of immersion in 0.1M NaCl solution, a corrosion ring is formed on the surface. This corrosion ring has a radius of r = 98.05 μm. Right below the corrosion ring, there is a smaller attack zone which appears as a dark circle in Figure 6.15(b). The main attack site within the corrosion ring is not seen until after 3 hours of immersion. This is located on the top edge of the corrosion ring.

As the immersion is continued, it is observed that the corrosion ring and the attack site get darker due to the accumulation of corrosion products on it. It is also seen that some of the regions of the exposed area are more corroded than the other. This can be distinguished by the contrast of each region, with the whiter regions less attacked than the darker regions. After 24 hours of immersion, 6.15(f), the surface is almost completely covered with corrosion product which obstructs the view of the sample surface.

The sample was desmutted and stuided under the SEM to obtain the images in Figure 6.16. From this Figure, the differences in magnitude and type of attack on different regions of the exposed sample

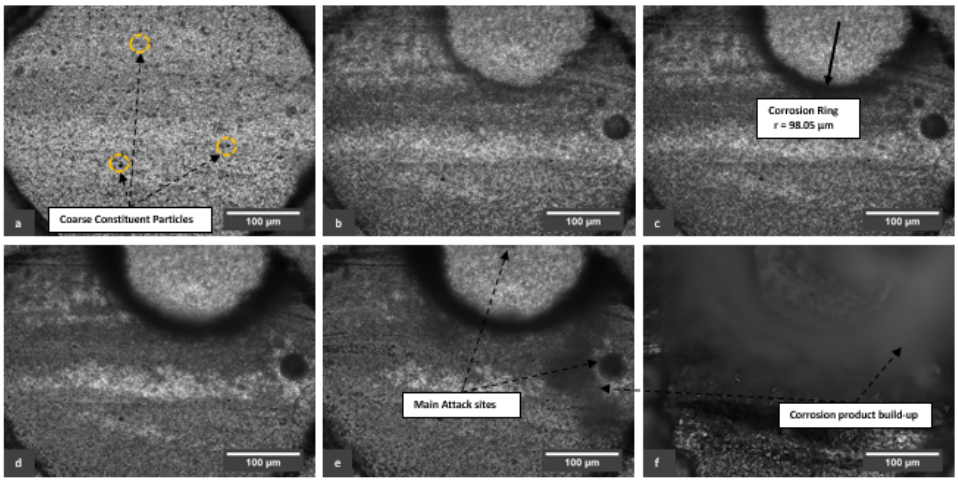

Figure 6.15: In-situ Immersion Test of AA2060 T8E30 SZ in a freshly prepared 0.1 M NaCl aqueous solution in ambient environment: (a) Before immersion, (b) 30 mins immersion, (c) 1 hour immersion, (d) 2 hrs immersion, (e) 3 hrs immersion, (f) After 24 hrs immersion.

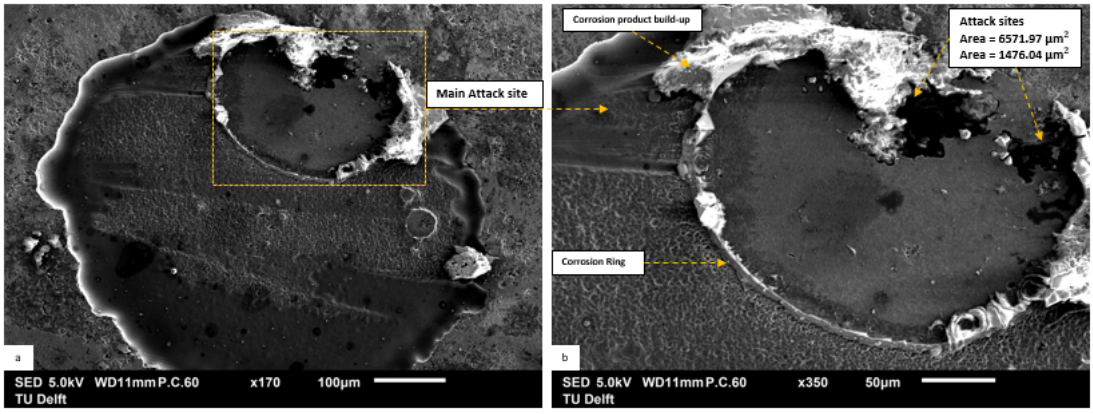

Figure 6.16: SEM images of exposed area of In-situ immersion test sample for AA2060 T8E30 SZ (a) Entire exposed region, (b) Attack site.

is observed. The top region (outside the corrosion ring) and the bottom region have a uniform surface with coarse particles still embedded to the surface. There are few pits and cavities seen here. The central region, on the other hand, is completely covered with small pits on the surface. Here, the coarse particles have trenches around them due to the galvanic activity between them and the alloy matrix.

The edges of the corrosion ring still have traces of corrosion product on them. The main attack region within this ring has 2 sites of attack located next to each other. The size of these sites are 6571.97 μm^2 and 1476.04 μm^2 in area. The rest of the area within the corrosion ring is protected by any type of attack and remains unchanged.

6.3.3. Thermo-mechanically Affected Zone (TMAZ)

The TMAZ zones of the weld region are quite small and narrow in width which does not allow for them to be isolated from the other zones. Due to this, a part of the TMAZ regions of both the alloys are exposed simultaneously in the in-situ immersion tests that follow. The exposed region has a diameter of d = 0.5 mm with the AA2060 T8E30 alloy located on the top and the AA2099 T83 alloy on the bottom. This immersion test was carried out for both the advancing and retreating side TMAZ regions.

TMAZ-RS

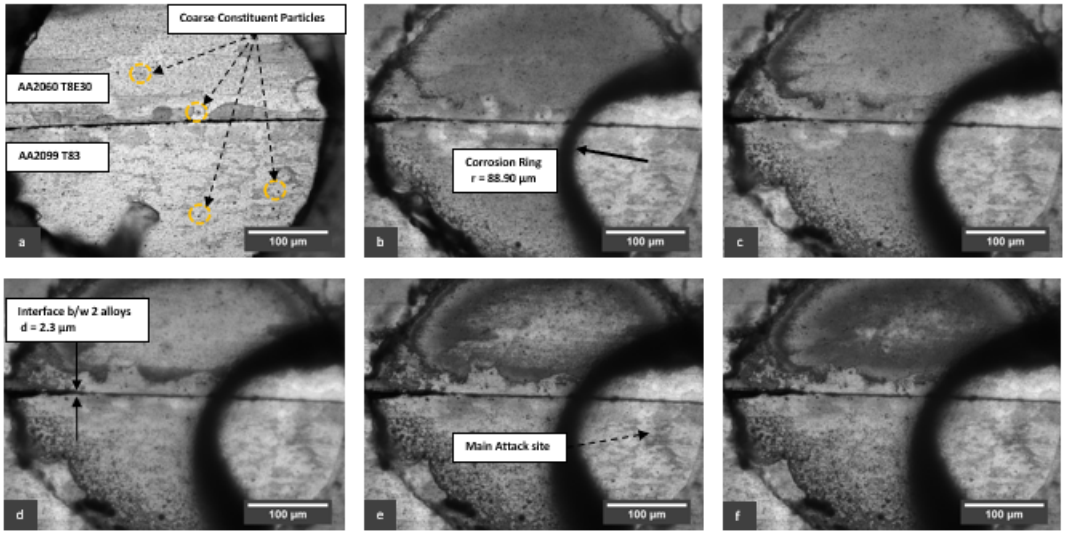

Figure 6.17: In-situ Immersion Test of TMAZ-RS in a freshly prepared 0.1 M NaCl aqueous solution in ambient environment: (a) Before immersion, (b) 1 hour immersion, (c) 1 hr 30 mins immersion, (d) 2 hrs immersion, (e) 2 hrs 30 mins immersion, (f) 3 hrs immersion.

The various intervals of the in-situ immersion test of the TMAZ-RS are shown in Figure 6.17. The exposed region is seen in Image (a) with the AA2060 T8E30 alloy on the top and the AA2099 T83 alloy at the bottom. They can be clearly distinguished from each other by the grain size, shape and orientation. These 2 alloys are separated by a gap of 2.3 μm. Large coarse constituent particles are seen located on the surface of both the alloys. Within 10 minutes of immersion, a corrosion ring is formed with a radius of r = 88.90 μm. In Figure 6.17(b) it is observed that this corrosion ring spans mostly the AA2099 T83 alloy and just a part of the AA2060 T8E30 alloy.

As immersion continues, both the alloys undergo different types of attack. On the AA2060 T8E30 alloy the grains are selectively attacked. These attacked grains can be seen as the darker grains in Figure 6.17(c-e). The type of attack on the AA2099 T83 alloy is intergranular, which is seen in images d and e. The main attack site is revealed in Figure 6.17(e) by the darkened region within the corrosion ring.

Pits are formed in both alloys but are different in size and distribution. In the AA2060 T8E30 alloy, the density of pit distribution is large but these pits are quite small. On the other hand, in the AA2099 T83 alloy the pits are large and at the sites of coarse particles. However, there are very few of these large pits on the surface of the AA2099 T83 alloy, as is observed in Figure 6.17(f).

The exposed region was desmutted in 30 % HNO_3 solution to remove the corrosion products on the surface and give a clear view of the corroded TMAZ RS region of both the alloys. The sample was then studied under SEM to obtain the images in Figure 6.18. Image a) shows the entire exposed region that was tested with the AA2060 T8E30 alloy on the top and the AA2099 T83 alloy at the bottom. There are still corrosion products attached to the surface edges and at the interface between the 2 alloys. The important features of this image are magnified and shown in images (b-d).

Figure 6.17(b) shows the largest attack site located within the corrosion ring on the side of AA2099 T83 alloy. This attack size has a total area of 11636.76 μm^2. There is a heavy build-up of corrosion products within the attack site. This was confirmed by an EDS scan of the region which indicated that they were indeed oxide products. The regions next to the main attack site were revealed to have a very high Cu concentration ranging between 11 % -18%. On the outer side of the corrosion ring, numerous pits were formed all along the edge.

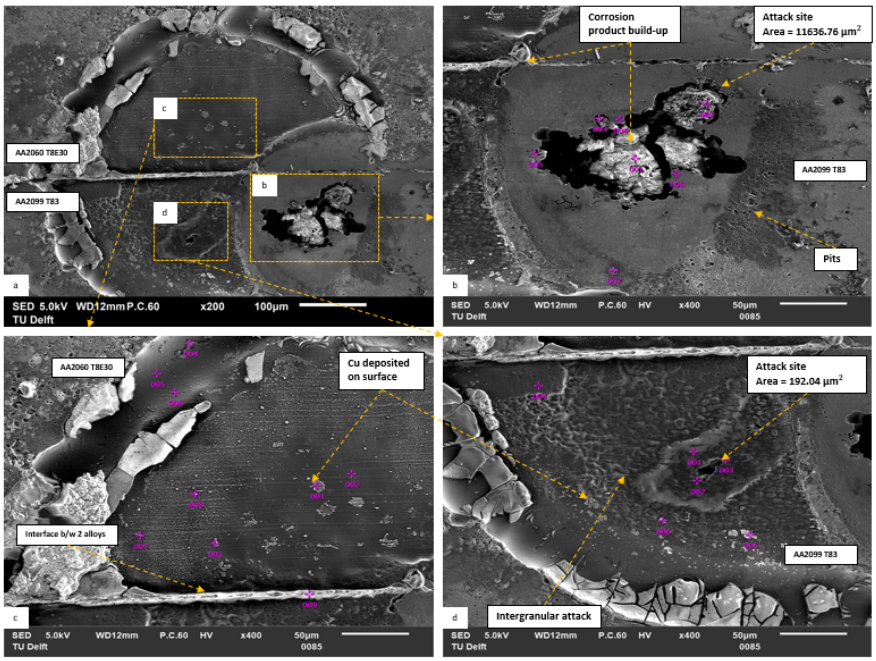

Figure 6.18: SEM images of exposed area of In-situ immersion test sample for TMAZ-RS (a) Entire exposed region after de-smutting, (b) Attack site (c) Cu deposits on surface, (d) Attack site.

The surface of the corroded AA2060 T8E30 TMAZ-RS region is seen in Figure 6.17 (c). The surface has a uniform texture with bright clusters of particles distributed on the surface. This suggests that the alloy undergoes uniform corrosion here. The bright clusters of particles were found to be Cu deposits by performing an EDS scan on the particles. These clusters were revealed to have extremely high Cu content with as much as 83.68 % concentration of Cu. These types of clusters are found in the AA2099 T83 alloy as well (Figure 6.17(d)). The interface gap is completely blocked with corrosion products, indicating that an attack has occurred within this gap.

Figure 6.17(d) shows the surface of the AA2099 T83 TMAZ-RS region outside of the corrosion ring. Almost the entire surface is affected by intergranular/ inter-subgranular attack. A small attack site is located in this region with an area of 192.04 μm^2. Cu deposits were located on the edges of the exposed region, as mentioned earlier. It is clear that the TMAZ-RS of both the alloys undergo different types of corrosion attacks and reveal different surface features that will be studied and discussed in the sections to follow.

TMAZ-AS

The TMAZ-AS regions of the AA2060 T8E30 alloy and the AA2099 T83 alloy were tested in an in-situ immersion test with the electrolyte as 0.1M NaCl solution. Figure 6.19(a-f) show the various intervals of the immersion test with the AA2060 T8E30 alloy on the top and the AA2099 T83 alloy at the bottom. Within a few minutes of immersion there is hydrogen gas evolution from the AA2099 T83 side, which later is the site for the main attack. In the AA2060 T8E30 side, there is a formation of a dark layer which is the build-up of corrosion products. This layer shows similarities to a corrosion ring but is not definitive.

On the AA2060 T8E30 TMAZ-AS, the initiation of pits is observed in Figure 6.19(b). However, a lot of these pits are terminated within 2 hours of immersion. The presence of pits on the AA2099 T83 side cannot be confirmed at this point, since there are no indications on the sites of coarse particles or at the surface of the matrix. After 24 hours of immersion, most of the upper side is covered with corrosion products and the main attack site is now apparent.

Since the in-situ images did not reveal much about the corrosion attack of the TMAZ-AS zone, the sample was desmutted and studied under SEM. Figure 6.20 shows the SEM images of the TMAZ-AS

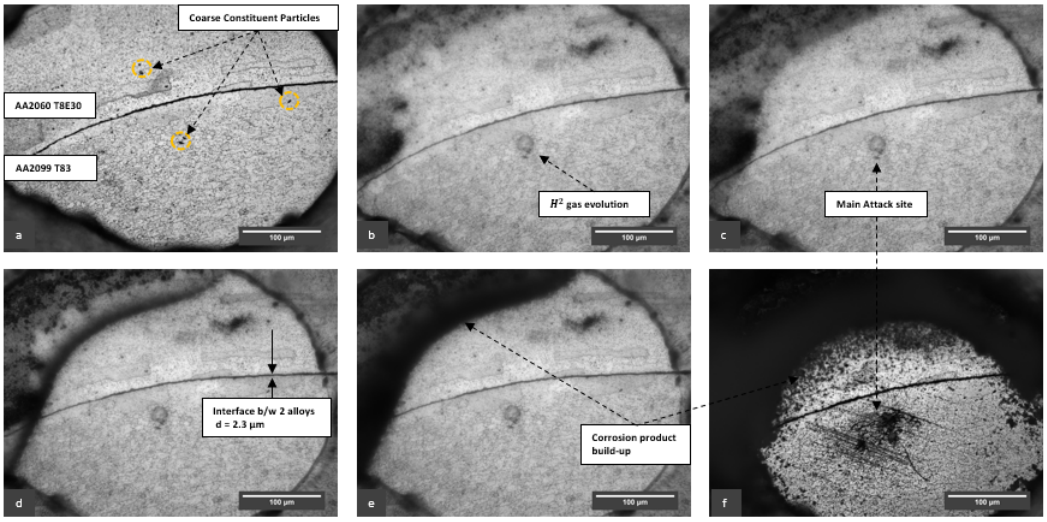

Figure 6.19: In-situ Immersion Test of TMAZ-AS in a freshly prepared 0.1 M NaCl aqueous solution in ambient environment: (a) Before immersion, (b) 30 mins immersion immersion, (c) 1 hour immersion, (d) 2 hrs immersion, (e) 3 hrs immersion, (f) After 24 hrs immersion.

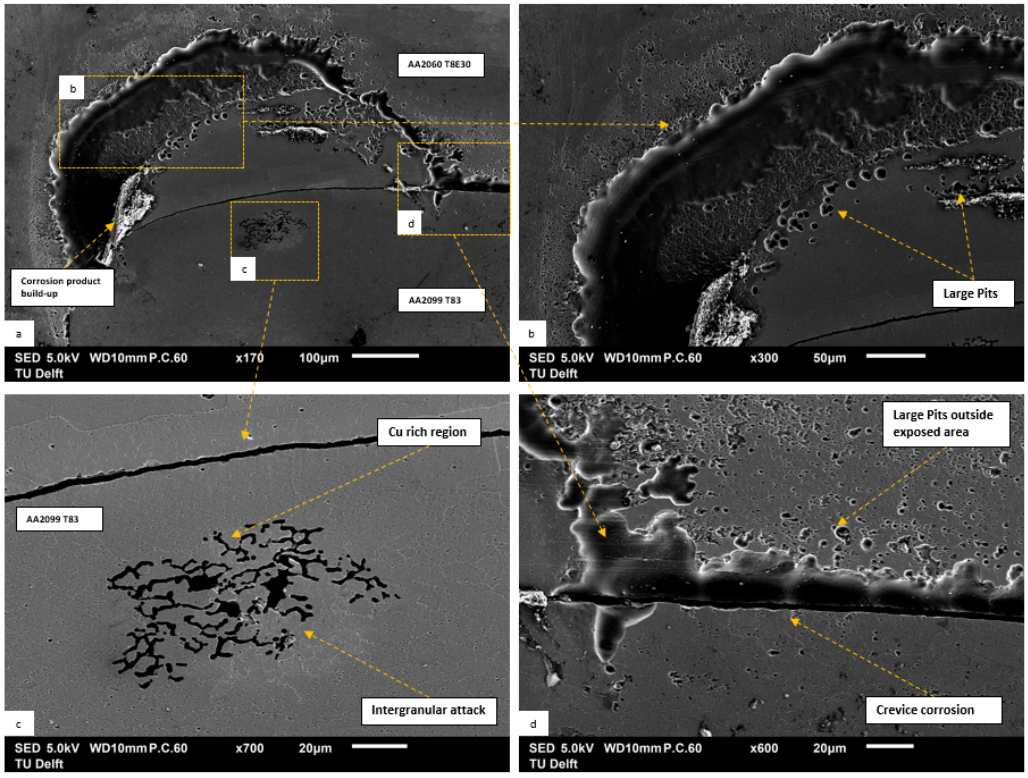

Figure 6.20: SEM images of exposed area of In-situ immersion test sample for AA2060 T8E30 BM (a) Entire exposed region after de-smutting, (b) Large pits on surface (c) Main attack site, (d) Crevice corrosion.

of both the alloys. Figure 6.20(a) shows the exposed region which was tested under in-situ immersion test. From this image, it is observed that most of the surface is protected from corrosive attack. This could imply that the dark layer was indeed a corrosion ring with an attack site in the middle and protected region all around it. The important features of this sample are magnified and shown in images (b-d).

Figure 6.20(b) shows the AA2060 T8E30 TMAZ-AS side of the sample. Here, the sample was indeed attacked at the region which was covered by the dark layer of corrosion products. On the inner edge of this layer, there are large pits on the surface of this alloy. The region surrounding these pits have a slightly higher Cu content with traces of Mg in them. The location and geometry of these pits are similar to those found on the edge of the corrosion ring in other zones of the AA2060 T8E30 alloy.

The main attack site is located in the AA2099 T83 TMAZ-AS and is seen in Figure 6.20(c). This is clearly an intergranular attack on the surface. An EDS scan revealed a slightly higher Cu content (approximately 5 %) in this region along with Si.

Image (d) of Figure 6.20 shows the region outside the exposed area of the TMAZ-AS region. However, it is observed that this region has also been attacked near the interface and pits have formed further away. These observations indicate that crevice corrosion has occurred here. During the immersion test, the electrolytic solution escapes through the interface gap of the alloys and propagates further into the weld joint sample. This leads to crevice corrosion in the sample.

6.4. Discussion

The in-situ immersion tests gives an insight into the corrosion behaviour of the weld zones in terms of the type of corrosion attack, the local attack sites, and even the role of intermetallic particles in the corrosion of these alloys. This can then be related to the microstructure and the electrochemical behaviour of the zones to give a complete overview of the localised corrosion behaviour of the alloys.

From these experiments, it is evident that the corrosion attack on the AA2099 T83 alloy starts immediately as the chloride ions from the electrolyte come in contact with the surface of the weld zones, with the formation of corrosion rings within the first 10 minutes. This was followed by H_2 gas evolution from the centre of the corrosion rings. The area from which the H_2 bubbles were released were later identified as attack sites. This was also reported in the work of Donatus et. al [6] on the AA2198 alloy welded by FSW. Since the attack sites act as the anode, the entire remaining region within the corrosion ring acts as the cathode and thus protecting itself from corrosive attack. For the SZ of this alloy, the corrosion ring formed an hour after immersion indicating a slower attack due to the passive behaviour of this zone, as observed in the previous chapter (Figures 5.2(d), 5.3(d)).

The darkening of the grain boundaries and sites of coarse particles during these immersion tests indicated that there was localised attack on the intermetallic particles. The coarse constituent particle sites get larger in area with increasing time of immersion. Under SEM analysis, it was found that there were trenches formed around the coarse particles. This indicated that these Cu rich or Cu-Fe coarse particles are more noble than the alloy matrix, thus causing them to act as cathodes and the alloy as anode. This leads to the dissolution of the alloy matrix around the coarse particles. This was also reported by Zhu et. al. [35] on their study of the AA2060-T8 alloy localised corrosion behaviour. In some cases, the alloy matrix around a particle is attacked to such an extent that the coarse particles are not attached to the matrix any longer. This leaves large pits/cavities on the surface of the matrix, as observed in Figure 6.8.

The attack on the grain boundaries, which is seen by the darkening of these regions, is due to the hardening precipitates present in the grain boundaries. The T_1 (Al_2CuLi) precipitate, which is the dominant phase found in this alloy [39], is highly active due to the presence of lithium in it [20]. Initially it acts as an anode with respect to the matrix during which the lithium in it degrades over time. Once this happens, the remaining elements in these particles are Al and Cu. The Cu content in this particle then makes it cathodic to the matrix, thus corroding the matrix all around it. This is referred to as the selective dissolution of the T_1 precipitate [30]. The BM and the HAZ regions exhibit severe intergranular attack due to the attack on the T_1 precipitates.

Since the hardening precipitates are not found in the SZ, this behaviour is not observed in the region. The attack on the SZ of the AA2099 T83 alloy is dominated by pitting due to the presence of

the Cu-rich coarse constituent particles which are distributed evenly on the surface and are less active than the T_1 precipitates [6]. This causes a slower attack in the SZ region as compared to the BM or the HAZ regions. Pits start to form all over the surface of this weld region. The re-passivation of some pits is observed during the immersion test. This passivity was also observed in the anodic polarisation and also in the LPR test of this weld region in the previous chapter. Once the passive layer breaks down and the corrosion attack continues, the entire surface is covered in pits.

The corrosion attack on the AA2060 T8E30 alloy weld regions is quite similar to that of the AA2099 T83 alloy. A corrosion ring formed within the first 15 minutes of immersion followed by anodic H_2 gas evolution from the centre of the corrosion ring. Large attack sites were later found at these regions. The sites of the coarse constituent particles and grain boundaries darkened indicating attack on these particles. The main attack sites of the AA2060 T8E30 weld zones exhibited a much larger attack compared to the ones seen in the AA2099 T83 alloy. However, the attack outside the corrosion ring was very limited and controlled. Towards the end of the experiment, the surface of the sample was completely covered in a thick layer of corrosion product build-up (Figure 6.16). These features suggested that the mechanism of corrosion of the AA2060 T8E30 alloy was not exactly the same as that of the AA2099 T83 alloy even though they do have similarities.

The BM of the AA2060 T8E30 alloy was studied under SEM and an EDS analysis was performed after the immersion test and desmutting. The coarse particles on the surface of the alloy were found to be the S phase (Al_2CuMg) particles. According to Zhu et. al. [35], the S phase particles are highly active compared to the alloy matrix. Thus they act as local anodic sites initially. The mechanism of attack on the S phase in this alloy is similar to that in the AA2024 alloy, as suggested by Wint. et al. [73]. They proposed that since the particle is more active than the matrix, it is galvanically attacked until all the Mg^{2+} and Al^{3+} ions are released from the particle. Once this happens, the remainder is a porous Cu sponge at the site of the particle. These Cu particles along with the Cu^{2+} ions are then redistributed and re-plated on the surface of the alloy. This was observed under the SEM images of the alloy, especially towards the edges of the exposed area in the experiment in Figure 6.10. This was also the reason why a high Cu content was always observed in the regions surrounding the attack sites. The dissolution of the S phase particles for the AA2060 alloy was also observed by Zhu et. al. [35].

The HAZ regions of the alloy exhibited intergranular corrosion in the main attack site within the corrosion ring. This was confirmed under SEM analysis of the samples. The intergranular attack was quite large ranging in size from 130 - 250 μm in length. The attack was due to the dissolution of the T_1 phase hardening precipitates located in the grain boundaries [39]. However, the entire exposed area outside the corrosion ring presented a very uniform surface with few pits on it. From the images of the in-situ test, it was observed that this region is also attacked but this is a very slow process. It was also seen that the attack starts in selected grains and is later propagated to the other grains on the surface. This is referred to as the selective dissolution of the strain deformed grains on this alloy [74]. The grains which are more deformed are more active compared to the less deformed grains. This causes the corrosion attack on these grains to occur first. Once these grains are completely attacked, the remaining grains are then attacked. This results in a thick build up of corrosion products on the surface. When the corrosion products are removed from the surface by desmutting, an entire layer of corroded grains is removed thus showing a uniform surface with few pits on it (Figure 6.12).

The AA2060 T8E30 SZ has a similar corrosion mechanism to that of the AA2099 T83 SZ. The region outside the corrosion ring is dominated by pitting corrosion, however this is not observed on the entire surface. This is attributed to the difference in alloying elements found in different regions of the SZ. In this region there is a mixture of both the alloys due to the FSW process. Due to this, certain regions with immense pitting were observed, as seen in the SZ of the AA2099 T83 alloy (Figure 6.16), and in certain regions the surface was uniform with small spots of Cu deposits as seen in the other weld zones of the AA2060 T8E30 alloy. This could also possibly be the reason why 2 corrosion potentials were observed for the AA2060 T8E30 SZ in Figure 5.3.

The galvanic effect between the 2 alloys were tested in the TMAZ regions of the weld sample. In the RS side of the TMAZ region the attack was more pronounced. A corrosion ring was formed partly

in both the alloys with the large attack side on the AA2099 T83 alloy side. Outside the corrosion ring, intergranular corrosion was observed in this alloy. For the AA2060 T8E30 alloy, the dissolution of the S phase particles were observed with Cu deposits on the surface. This attack was followed by the dissolution of the grains as seen earlier. The crevice between the 2 alloys, with a width of 2.3 μm, also induced crevice corrosion here although this was quite limited in the RS side.

The AS side of TMAZ region also exhibited intergranular attack on the AA2099 T83 side. On the AA2060 T8E30 side, large pits were observed on the edge of the corrosion ring. However, in this region the crevice attack took over as the dominant type of attack thus protecting the remainder of the exposed area. This attack continued outside the exposed area on either sides of the crevice, since there was a pathway for the electrolyte through the crevice. These experiments indicated that the galvanic effect between the 2 alloys is not severe due to the similarities of the microstructure and its features, thus giving rise to similar electrochemical behaviour in both the alloys. This was also observed in the open circuit potential values of the alloys in the previous chapter (Figure 5.1), which presented that the potentials of both the alloys are quite similar to each other (within a range of 10 - 20 mV vs Ag/AgCl).

6.5. Conclusion

The corrosion behaviour and type of corrosion attack on the AA2099 T83 and AA2060 T8E30 alloys and their respective weld zones were investigated in this chapter. The attack on the BM and HAZ regions of both alloys initiated as soon as the immersion started with the formation of a corrosion ring and hydrogen evolution. The sites of hydrogen evolution were later identified as attack sites. Intergranular corrosion was observed in these regions due to the attack on the T_1 precipitates located on the grain boundaries which caused pitting in these sites. Trenches, cavities, and pits were observed at the sites of the coarse particles suggesting galvanic activity between the coarse particles and the alloy matrix. The attack on the SZ regions was suggested to be caused by the activity of the coarse constituent particles since there were no hardening precipitates in this region, which resulted in a slower attack than the other regions.

The AA2060 T8E30 alloy weld regions also exhibited an attack by the selective dissolution of deformed grains. It was suggested that this occurred due to the strain induced by strengthening methods which resulted in a uniform surface outside the corrosion ring after desmutting the sample. Cu platelets were observed on the surface of this alloy after desmutting. It was proposed that these platelets/particles were related to the dissolution of the S phase (Al_2CuMg) particles. These particles when corroded, left a porous Cu deposit in the pit which was then re-plated on the surface of the alloy. The SZ of the AA2060 T8E30 exhibited pitting attack in certain regions and selective dissolution of grains in other regions. It was proposed that this occurred due to the alloying elements of both the AA2099 T83 and the AA2060 T8E30 alloys in this region.

It was observed that when the TMAZ regions were tested in a couple, a localised corrosion attack occurred in both alloys. The AA2099 T83 alloy exhibited pitting and intergranular attack whereas the AA2060 T8E30 alloy exhibited selective dissolution of grains and the dissolution of S phase particles resulting in Cu deposits on the surface. Thus, it was suggested that the galvanic effect between the 2 alloys was not too severe causing a particular alloy to be more corroded than the other. Crevice corrosion was also observed in the interface between the 2 alloys resulting in a deeper attack within the alloys.

7

Effect of Anodising and Sol-gel coating on the FSW alloy

7.1. Introduction

Anodising has been know to increase the corrosion resistance of aluminium alloys and is used widely in the aerospace industry for protection against corrosion [3]. On the other hand, the role of sol-gel coatings are to provide good adhesion between the metal and paint [75]. Hence, the sol-gel coatings themselves are not sufficient protection for the aluminium alloys. In this chapter, the effect of anodising and sol-gel coating on the electrochemical behaviour of the welded alloys are evaluated by electrochemical methods. This determines their advantages over the as-received samples and how well they protect the alloys from corrosion.

7.2. Materials and Experimental Methods

The samples used were obtained from the anodised welded sample and the sol-gel coated welded sample of the Z-shaped extrusion of AA2099-T83 and cold rolled sheet of AA2060-T8E30 provided by Arconic. The sample preparation and experimental details of the tests conducted are given in chapter 3. All the chemicals used were of analytical grade and provided by Sigma-Aldrich Chemical Company. The electrochemical tests were conducted in a freshly prepared 0.1M NaCl aqueous solution of near neutral pH in ambient environment.

7.3. Results

7.3.1. Effect of Anodising

Thickness of Anodised Layer

The anodised layer thickness of both the AA2099 T83 and AA2060 T8E30 alloys were measured and are given in Table 7.1 with the thickness profile plotted in Figure 7.1. An inverted V-shaped trend was observed for both the alloys with the highest values at the SZ.

The BM of the AA2099 T83 alloy has an anodised layer of thickness t = 2.49 ± 0.08 μm. As the centre of the weld region is approached, the thickness keeps increasing by 0.1 - 0.15 μm in each zone, until the SZ where there is a sudden increase in the thickness of the anodised layer, t = 3.34 ± 0.26 μm. This is a 33.8% increase in thickness as compared to the BM of this alloy.

For the AA2060 T8E30 alloy, again the BM has the lowest value with thickness t = 2.49 ± 0.08 μm. This is similar to the thickness of the BM of AA2099 T83 alloy. The HAZ regions have a slightly thicker anodised layer than the BM. It is important to note that in this alloy, the TMAZ zone is not visible on the surface since it engulfs the nugget zone and is situated on the inner region of the alloy. The SZ has

Table 7.1: Thickness of anodised layer at the weld zones of the AA2060 T8E30 and AA2099 T83 alloys.

Alloy	Weld Zone	Thickness (μm)
AA2060 T8E30	BM	2.49 ± 0.08
	HAZ AS	2.95 ± 0.16
	SZ	3.34 ± 0.15
	HAZ RS	2.98 ± 0.09
AA2099 T83	BM	2.50 ± 0.22
	HAZ AS	2.59 ± 0.10
	TMAZ AS	2.88 ± 0.08
	SZ	3.34 ± 0.26
	TMAZ RS	2.67 ± 0.14
	HAZ RS	2.63 ± 0.10

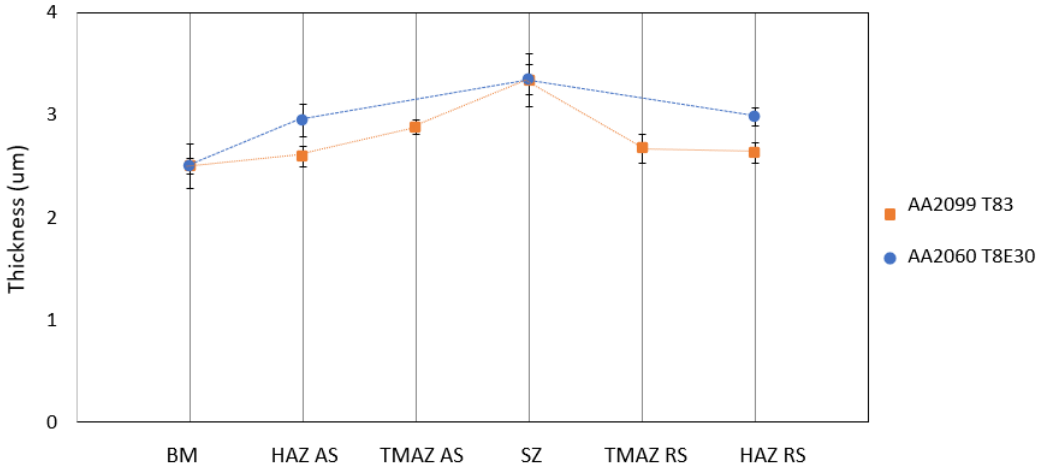

Figure 7.1: Anodised layer thickness at the weld zones of the AA2099 T83 and AA2060 T8E30 alloys.

the thickest anodised layer in this alloy. Its thickness, t = 3.34 ± 0.15 μm, is again a 33.8% increase compared to the BM of the alloy.

Effect on Mechanical Properties - Micro-hardness

The micro-hardness of the anodised alloys BM was measured using a Streurs Vickers micro-hardness testing machine and are given in the Table 7.2. The values of the as-received alloys BM are also shown here for comparison. It was observed that the anodised sample BM clearly has a higher micro-hardness value compared to the as-received sample. For the AA2099 T83 alloy, the increase in hardness is quite considerable with a 56.82 % increase, whereas the increase in the AA2060 T8E30 BM is very less with just a 1.32 % increase. The micro-hardness of the SZ of anodised sample could not be measured due to the inadequate resolution of the Micro-hardness testing machine.

Table 7.2: Micro-hardness values of anodised sample and as-received sample base metals of the AA2099 T83 & AA2060 T8E30 alloys.

	Micro-hardness (0.5HV)	
Alloy	As-received sample	Anodised sample
AA2099 T83	122 ± 2.33	191.33 ± 0.67
AA2060 T8E30	177 ± 1.53	179.33 ± 2.19

Potentiodynamic Polarisation of Anodised samples

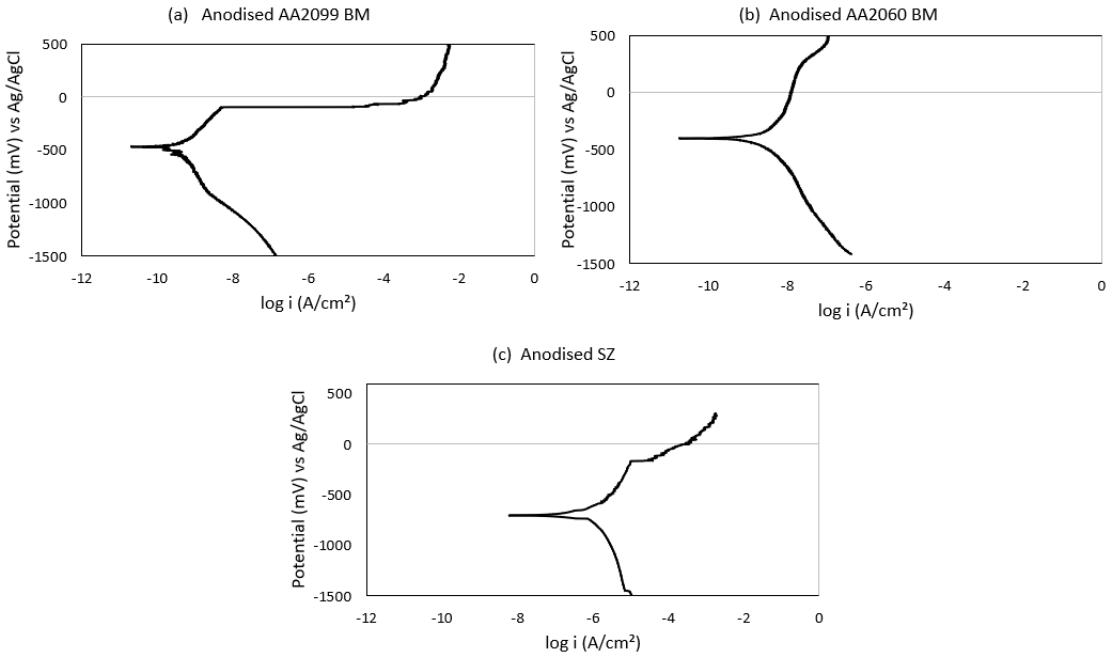

Figure 7.2: Potentiodynamic polarisation curves for the anodised samples in a 0.1 M aqueous NaCl solution in an ambient environment: (a) AA2099 T83 BM, (b) AA2060 T8E30 BM, and (c) SZ of the anodised sample.

The potentiodynamic polarisation curves for the anodised sample regions in 0.1 M aqueous NaCl solution in an ambient environment are given in the Figure 7.2. The values for the corresponding corrosion current density and the corrosion potentials were determined by Tafel extrapolation and are given in the Table 7.3. The corrosion potential of the SZ is clearly much more negative than that of the 2 base metals indicating its higher tendency for corrosion. The corrosion current density of the SZ is also very high suggesting the high rate of corrosion in this zone. In regards to the base metals, the AA2060 T8E30 BM has a higher current density and a lower corrosion potential compared to the AA2099 T83 BM. Therefore the order of nobility of the anodised samples from less noble to high noble is: SZ < AA2060 T8E30 BM < AA2099 T83 BM.

Table 7.3: Corrosion potential (E_{corr}) and corrosion current density (I_{corr}) of the anodised sample AA2099 T83 BM, AA2060 T8E30 BM, and SZ from potentiodynamic polarisation in 0.1 M aqueous NaCl solution in ambient environment.

Samples	E_{corr} (mV) vs Ag/AgCl	$I_{corr}(\mu A/cm^2)$
AA2099 T83 BM	-419.74 ± 31.329	0.000122 ± 0.00003
AA2060 T8E30 BM	-496.30 ± 62.177	0.009378 ± 0.00882
SZ	-704.61	0.068

From the Figure 7.2, it is observed that there is passive behaviour in all 3 tested samples. The anodised AA2099 T83 BM shows a passive behaviour till a pitting potential of -95 mV vs Ag/AgCl, after which there is a huge surge in the current density indicating pitting corrosion. The anodised AA2060 T8E30 BM presents a more effective passive layer compared to the AA2099 T83 BM. This is indicated by the anodic branch of the potentiodynamic polarisation curve in Figure 7.2(b). The pitting potential of this sample was found to be 255 mV vs Ag/AgCl, thus suggesting that this sample is more resistant to pitting. The SZ of the anodised sample has a pitting potential of -173 mV vs Ag/AgCl. This is the lowest compared to the other anodised samples, suggesting that this region is the most prone to pitting corrosion.

The 3 tested samples have limited current density due to oxygen diffusion. However, the SZ has a

more pronounced effect as observed by the decreasing slope of the cathodic branch of the SZ in Figure 7.2(c). For the base metals of the anodised samples, the slope is more inclined, hence suggesting that this effect is not as much in the SZ.

The rate of corrosion in the anodised sample is in the order: AA2099 T83 BM < AA2060 T8E30 BM < SZ, where SZ has the highest rate of corrosion, indicating that this region is the most vulnerable zone of the 3 in this sample.

7.3.2. Effect of Sol-gel coating on the surface

LPR Measurements of Sol-gel coated samples

The linear polarisation resistance graphs for both the base metals and the SZ of the sol-gel sample in 0.1 M aqueous NaCl solution in an ambient environment are given in Figure 7.3. From this figure, it is observed that the resistivity of the SZ is highest during the overall experiment of 24 hours. The AA2060 T8E30 BM has a slightly less resistivity compared to the SZ. The AA2099 T83 BM has the least resistivity amongst the 3 samples tested.

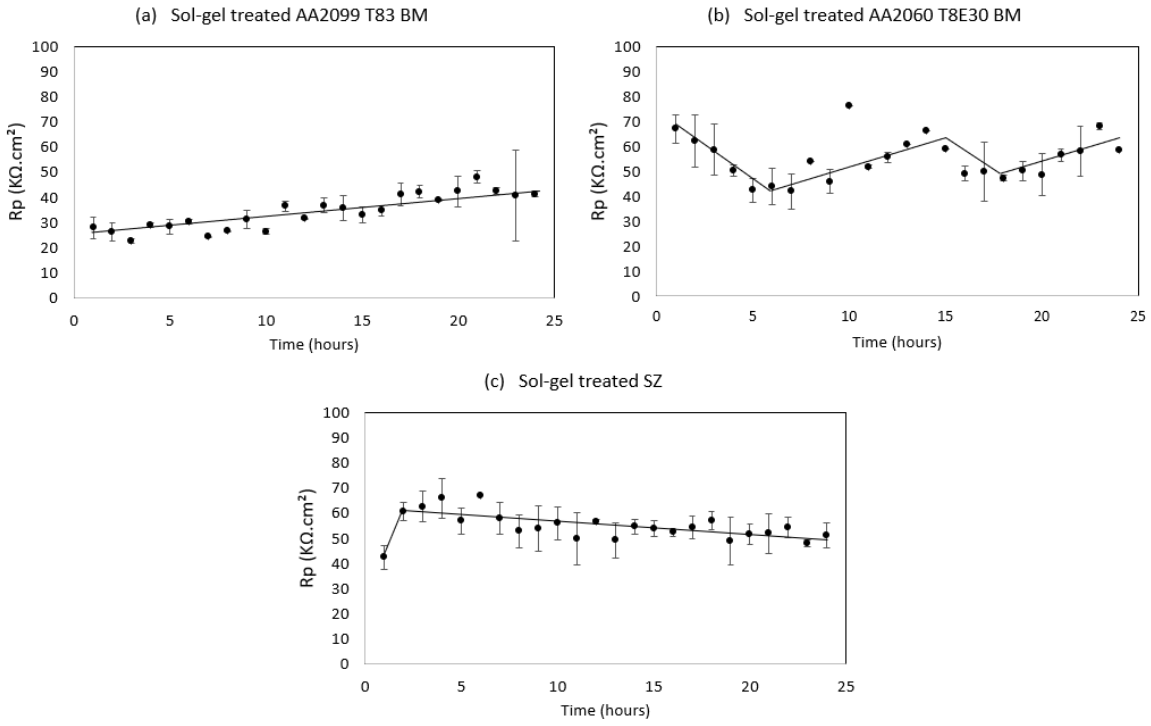

Figure 7.3: LPR measurement as a function of time over 24 hours of total experiment time in 0.1 M aqueous NaCl solution in ambient environment of the Sol-gel samples: (a) AA2099 T83 BM, (b) AA2060 T8E30 BM , (c) SZ

The trend for the resistivity is different for each sample. The sol-gel treated AA2099 T83 BM has an increasing trend in resistivity throughout the 24 hours of total experimental time. The initial resistivity of this zone is R_P = 27.89 $K\Omega.cm^2$, and the resistivity at 24 hours reaches a value of R_P = 48 $K\Omega.cm^2$, which is almost twice of the initial value. For the AA2060 T8E30 BM, the initial resistivity is R_P = 66.91 $K\Omega.cm^2$. An initial decrease is observed till 6 hours of immersion, after which a gradual increase is seen for 10 hours suggesting the formation of a passive layer. This is followed by a sudden decrease in resistivity for 3 hours and then again an increase till the end of the experiment where the resistivity at 24 hours is 67.86 $K\Omega.cm^2$.

The resistivity graph of the SZ of the sol-gel sample is presented in Figure 7.3(c). Unlike the base metals, this region has a decreasing trend of resistivity. At 1 hour of immersion, the resistivity recorded is R_P = 42.21 $K\Omega.cm^2$, after which an initial increasing trend was observed till 4 hours (60 $K\Omega.cm^2$).

Here onwards the resistivity of the SZ gradually decreases over time. It is important to note that although there is a decrease, the final resistivity at 24 hours is R_P = 51 $K\Omega.cm^2$.

7.4. Discussion

7.4.1. Effect of Anodising

Anodizing the FSW sample resulted in the formation of different thickness of the anodised layer on the individual weld zones, as observed in Figure 7.1 and Table 7.1. This result was also observed in various literature sources [3, 76, 77]. However, the trend of anodised layer thickness in these sources is not consistent. In the FSW sample of AA5083 and AA6082 [76], it was observed that both alloys have different thickness of the anodised layer in both the base materials, which was due to the variations of alloying compositions of both the alloys. In the joining of AA2198 alloy by FSW [3], it was observed that the SZ had the thickest anodized layer, which was attributed to the higher content of Li in solid solution due to dissolution of the T_1 precipitates during FSW.

For the base metals of the AA2099 T83 and AA2060 T8E30 alloys, similar thickness of the anodised layer was observed with an increasing trend towards the centre of the weld. Thus the SZ had the thickest anodised layer. This is similar to the case of the AA2198 alloy [3], indicating that the high Li content in solid solution was the reason for this phenomenon. It was suggested that higher the Li content in solid solution, the higher the oxidation rate of the region during anodizing [3]. The dissolution of T_1 precipitates is higher in the SZ, followed by the TMAZ, the HAZ, and no dissolution in the BM. Therefore, the trend in thickness of the anodised layer is directly proportional to the dissolution of the T_1 phase during the friction stir welding process.

The micro-hardness of the anodised sample SZ was found to be the highest in the work of Donatus et. al. [3] on the AA2198 alloy. They suggested that the porous oxide formed on the SZ had the shortest inter-pore distance and/or the thickest cell walls of the pores. This caused the porous oxide layer to be brittle in this region, whereas it was increasingly ductile in the other regions. Therefore, the trend of micro-hardness observed in the anodised sample was increasing from BM to SZ for the AA2198 alloy [3].

An increase in micro-hardness was observed in the anodised AA2099 T83 and AA2060 T8E30 alloys base metals, as seen in Table 7.2. However, the micro-hardness of the SZ could not be determined due to the concentric ”onion” rings formed on the surface of the SZ during FSW. The indentation formed by the micro-hardness testing machine in the SZ could not be observed with the microscopic lens due to the uneven topography of the surface of this zone.

The potentiodynamic polarisation tests of the anodised samples revealed that anodising does in fact protect the alloys from corrosion attack. The corrosion current density of these samples (Table 7.3) were much less than that of the as-received samples, indicating a lower corrosion rate. The SZ exhibited the highest current density among the 3 tested samples, however this was still 4 times less than that of the as-received sample SZ. A distinct passive region is observed for both the alloy base metals as well as the SZ. The pitting potentials of these samples are also much higher than the as-received sample thus indicating that anodising the surface of these alloys play an important role in protection against localised corrosion. This result was also observed for the AA2198 alloy by Donatus et. al. [3].

7.4.2. Effect of Sol-gel coating on the surface

The resistivity of the sol-gel coating on the surface of the alloys was observed to be much more than that of the as-received alloys sample. In fact, an increasing trend in resistivity in the base metals was found in the sol-gel coated sample. This was attributed to the renewal ability of the sol-gel coating [75]. In the work of Yang et.al [78] on the sol-gel coating of AA2024 alloy, it was observed that as the immersion tests starts, initial pitting is observed. However, after some time most pits slow down or stop propagating entirely due to the formation of a mixed (aluminium-silicon) oxide insoluble layer, which

blocks pores and defects in the sol-gel coating [78].

The AA2099 T83 alloy BM, being the more active alloy, exhibits a low resistivity compared to the AA2060 T8E30 BM. Even though the AA2060 T8E30 BM presented a higher resistivity, a decrease in resistivity was observed at 5 hours and 18 hours into immersion. This was attributed to the corrosion attacks on different regions of the surface of the alloy due to ageing parameters. Urushino et. al. [72] found that pitting occurred at different intervals for the grains and the grain boundaries in the AA2024 alloy which had undergone ageing thus exhibiting a selective pitting attack along the grain boundaries.

The SZ of the sol-gel coated sample too had a sudden increase in resistivity after 2 hours of immersion, as seen in Figure 7.3, however the pit density in this zone is very high (Figure 6.7 and 6.8). Therefore after an initial increase in resistivity, a slow decreasing in resistivity was observed for the SZ of the sol-gel coated sample as the propagation of pits occurred at a much faster rate than the rate of the sol-gel coating renewal. Overall, the sol-gel coating presented a higher resistivity for the alloys by a factor of approximately 5 times that of the as-received sample, thus indicating that the sol-gel coating does protect the alloy surface from localised corrosion attacks.

7.5. Conclusion

The effect of anodising the surface of the FSW alloy was investigated. It was observed that the microhardness of the base materials had increased due to the formation of the anodised oxide layer. A reduction in current density was observed for the AA2099 T83 BM, AA2060 T8E30 BM, and the SZ of the anodised sample. The SZ exhibited a higher corrosion current density suggesting a higher corrosion rate than the base metals of the alloys. A distinct and effective passive region was also observed for all 3 samples, suggesting that the anodised layer was effective in protecting the surface of the alloys from immediate localised corrosion.

The effect of sol-gel coating on the FSW alloy was also evaluated. Overall, the sol-gel coated samples exhibited a much higher resistivity compared to the as-received sample. It was found that the initial resistivity was low due to immediate pitting on the surface. However, an increase in resistivity was observed after some time. It was suggested that this occurred due to the self-healing or renewal ability of the sol-gel coating which caused the pits to slow down or stop altogether. Therefore, the sol-gel coating on the sample did enhance the corrosion protection of the FSW AA2099 T83 and AA2060 T8E30 alloys.

8

Conclusion

In the current project, the localised corrosion behaviour of the friction stir welded AA2099 T83 and AA2060 T8E30 alloy has been studied. The correlation between the microstructure of the weld zones and the corrosion behaviour was determined. The effect of anodising and sol-gel coating of the surface of the alloys on the electrochemical behaviour of the sample was also investigated.

The microstructural characterisation of the AA2099 T83 and AA2060 T8E30 alloys revealed that the production methods used - extrusion for the AA2099 T83 alloy and cold rolling for the AA2060 T8E30 alloy, had resulted in different microstructures in both the alloys. The AA2099 T83 had small grains due to recrystallisation during extrusion, whereas the AA2060 T8E30 had large, elongated, and layered grains due to cold rolling. Large Al-Cu-Fe-Mn intermetallic particles were found on the matrix of both alloys. S (Al_2CuMg) phase particles were also observed in the AA2060 T8E30 alloy matrix. Large dispersoids were observed on the matrix of both alloys. The smaller hardening precipitates were mostly observed on the grain boundaries but also on the matrix of the alloy.

The effect of friction stir welding on the microstructure of the weld zones was investigated for both alloys. It was observed that the SZ regions had undergone dynamic recrystallisation to obtain fine grains. A decreasing trend in average grain area was observed towards the weld centre for both alloys. The were no hardening precipitates observed in the SZ regions due to the dissolution of these particles during the FSW process. A lower distribution density of hardening precipitates was also observed in the HAZ and TMAZ regions. It was also found that the coarse constituent particles were fragmented in the weld regions due to their breakdown during FSW. The lower distribution of hardening precipitates in the weld regions resulted in a decrease in the micro-hardness of these regions towards the weld centre. The lowest micro-hardness values were recorded for the HAZ/TMAZ interface. It was proposed that this occurred due to the dissolution of the T_1 precipitates and the coarsening of grains in the HAZ regions.

The electrochemical behaviour and kinetics of corrosion of the AA2099 T83 and AA2060 T8E30 alloys weld regions were investigated using electrochemical methods. The AA2099 T83 alloy was found to be the more electrochemically active alloy. The nobility of the weld zones of the AA2099 T83 alloy was in the order: SZ > HAZ RS > BM > HAZ AS, and that of the AA2060 T8E30 alloy was in the order: HAZ AS > SZ > BM > HAZ RS. The corrosion rates were determined by the potentiodynamic polarisation tests. For the AA2099 T83 weld zones, the corrosion rate follows the order: HAZ RS < HAZ AS = SZ < BM , and for the AA2060 T8E30 alloy: SZ < BM < HAZ AS < HAZ RS, from lowest to highest corrosion rates. A distinct passivity was observed for the SZ of both alloys. It was proposed that due to the absence of the T_1 precipitates, the SZ regions of the alloys were the least prone to corrosion attack.

The localised corrosion attack on the AA2099 T83 and AA2060 T8E30 alloys and their respective weld zones was determined by the immersion tests in a chloride environment. It was observed that the attack on the BM and HAZ regions of both alloys initiated as soon as the immersion started with the formation of a corrosion ring and hydrogen evolution from the centre of the corrosion ring, which were

later identified as attack sites. Intergranular corrosion was observed in these regions due to the attack on the T_1 precipitates located on the grain boundaries which caused pitting in the grain boundaries. Trenches, cavities, and pits were observed at the sites of the coarse particles due to galvanic activity between the coarse particles and the alloy matrix which caused either partial or complete dissolution of the coarse particles. The attack on the SZ regions was suggested to be caused by the activity of the coarse constituent particles since there were no hardening precipitates in this region, which resulted in a slower attack than the other regions.

The AA2060 T8E30 alloy weld regions exhibited an attack caused by the selective dissolution of deformed grains. It was suggested that this occurred due to the strain induced by strengthening methods which resulted in a uniform surface outside the corrosion ring after desmutting the sample. Cu platelets were observed on the surface of this alloy after desmutting due to the dissolution of the S phase (Al_2CuMg) particles. These particles when corroded, left a porous Cu deposit in the pit which was then re-plated on the surface of the alloy. The SZ of the AA2060 T8E30 exhibited pitting attack in certain regions and selective dissolution of grains in other regions. It was proposed that this occurred due to the alloying elements of both the AA2099 T83 and the AA2060 T8E30 alloys in this region.

Lastly, the effect of anodising the surface of the FSW alloy and sol-gel coating on the alloy were investigated. From the potentiodynamic polarisation tests, a reduction in current density was observed for the base metals and the SZ of the anodised sample. A distinct and effective passive region was also observed for all 3 samples, indicating that the anodised layer was effective in protecting the surface of the alloys from corrosion attack. It was observed that the SZ exhibited the highest corrosion current density among the 3 samples suggesting a higher corrosion rate than the base metals of the alloys. The effect of sol-gel coating on the FSW alloy was also evaluated. It was found that the initial resistivity was low due to immediate pitting on the surface. However, an increase in resistivity was observed after a few hours of immersion. It was suggested that this occurred due to the renewal ability of the sol-gel coating which caused the pits to slow down or stop altogether. It was revealed that the sol-gel coated samples exhibited a much higher resistivity compared to the as-received sample. Therefore, the sol-gel coating on the sample did enhance the corrosion protection of the FSW AA2099 T83 and AA2060 T8E30 alloys.

The project was completed to the maximum possible standards given the equipment and time frame. However, due to limitations of the equipment, certain important factors could not be determined. The smaller microstructural characteristics of the alloys could not be determined due to insufficient resolution of the SEM and the inability of EDS to detect Li. This did not allow an investigation into the composition of the smaller hardening precipitates which are found to be the dominant sites of localised corrosion attack. Additionally the TMAZ weld regions of the alloys could not be investigated fully due to the narrow widths of this region. The potentiodynamic polarisation tests did not reveal the corrosion current densities of the base metals due to the extremely quick rate of corrosion on the surface of the alloys. It was also found that the heat disspiation during FSW caused over-ageing in the base metals of the alloys resulting in a change in the micro-hardness. Therefore, future work may be done to investigate the role of the hardening precipitates, such as the T_1 phase, in the localised corrosion behaviour of the weld zones of FSW Al-Li alloy. This approach would give a complete overview to the localised corrosion behaviour of the Al-Li alloys.

Bibliography

[1] N Eswara Prasad, Amol Gokhale och RJH Wanhill. *Aluminum-lithium alloys: processing, properties, and applications*. Butterworth-Heinemann, 2013.

[2] B Cai, ZQ Zheng, DQ He, SC Li och HP Li. Friction stir weld of 2060 Al-Cu-Li alloy: Microstructure and mechanical properties. *Journal of Alloys and Compounds*, 649:19–27, 2015.

[3] Uyime Donatus, Raphael Oliveira Ferreira, Naga Vishnu Vardan Mogili, Barbara Victoria Gonçalves de Viveiros, Mariana Xavier Milagre och Isolda Costa. Corrosion and anodizing behaviour of friction stir weldment of AA2198-T851 Al-Cu-Li alloy. *Materials Chemistry and Physics*, 219:493 – 511, 2018.

[4] A Fattah-alhosseini, M Naseri, D Gholami, O Imantalab, FR Attarzadeh och MK Keshavarz. Microstructure and corrosion characterization of the nugget region in dissimilar friction-stir-welded AA5083 and AA1050. *Journal of materials science*, 54(1):777–790, 2019.

[5] G. Rambabu, D. Balaji Naik, C.H. Venkata Rao, K. Srinivasa Rao och G. Madhusudan Reddy. Optimization of friction stir welding parameters for improved corrosion resistance of AA2219 aluminum alloy joints. *Defence Technology*, 11(4):330 – 337, 2015.

[6] Uyime Donatus, Barbara Victoria Gonçalves de Viveiros, Maicon Cavalieri de Alencar, Raphael Oliveira Ferreira, Mariana Xavier Milagre och Isolda Costa. Correlation between corrosion resistance, anodic hydrogen evolution and microhardness in friction stir weldment of AA2198 alloy. *Materials Characterization*, 144:99 – 112, 2018.

[7] Andrew R Barron. *Physical methods in chemistry and nano science*. Rice University, 2015.

[8] David Costa Milan. *Experimental study of electronic transport in single molecular contacts and surface modification via STM*. Doktorsavhandling, Universidad de Alicante, 07 2016.

[9] Emmanouela Michailidou. *Corrosion Studies on Magnesium and Magnesium Containing Alloys*. Doktorsavhandling, Swansea University, 2018.

[10] Edgar A Pina-Galan. Mathematical analysis of the operation of a scanning kelvin probe. *arXiv preprint arXiv:1907.07465*, 2019.

[11] Egoitz Aldanondo, Ekaitz Arruti, Alberto Echeverria och Iñaki Hurtado. Friction stir welding of lap joints using new Al–Li alloys for stringer-skin joints. I: *Friction Stir Welding and Processing X*, ss 77–88. Springer, 2019.

[12] Y. Ma, X. Zhou, W. Huang, Y. Liao, X. Chen, X. Zhang och G. E. Thompson. Crystallographic defects induced localised corrosion in AA2099-T8 aluminium alloy. *Corrosion Engineering, Science and Technology*, 50(6):420–424, 2015.

[13] João Victor de Sousa Araujo, Uyime Donatus, Fernanda Martins Queiroz, Maysa Terada, Mariana Xavier Milagre, Maicon Cavalieri de Alencar och Isolda Costa. On the severe localized corrosion susceptibility of the AA2198-T851 alloy. *Corrosion Science*, 133:132 – 140, 2018.

[14] Nikolaos D. Alexopoulos, Angeliki Proiou, Wolfgang Dietzel, Carsten Blawert, Volker Heitmann, Mikhail Zheludkevich och Stavros K. Kourkoulis. Mechanical properties degradation of Al-Cu-Li 2198 alloy due to corrosion exposure. *Procedia Structural Integrity*, 2:597 – 603, 2016. 21st European Conference on Fracture, ECF21, 20-24 June 2016, Catania, Italy.

[15] ASM International. Handbook Committee. *Properties and selection: nonferrous alloys and special-purpose materials*, band 2. Asm Intl, 1990.

[16] Timothy Warner. Recently-developed aluminium solutions for aerospace applications. I: *Materials Science Forum*, band 519, ss 1271–1278. Trans Tech Publ, 2006.

[17] M Romios, R Tiraschi, JR Ogren, OS Es-Said, C Parrish och HW Babel. Design of multistep aging treatments of 2099 (C458) Al-Li alloy. *Journal of Materials Engineering and Performance*, 14(5):641–646, 2005.

[18] Roberto J Rioja och John Liu. The evolution of Al-Li base products for aerospace and space applications. *Metallurgical and Materials Transactions A*, 43(9):3325–3337, 2012.

[19] John W Martin. Aluminum-lithium alloys. *Annual Review of Materials Science*, 18(1):101–119, 1988.

[20] R. G. Buchheit, J. P. Moran och G. E. Stoner. Electrochemical behavior of the T1 Al_2CuLi intermetallic compound and its role in localized corrosion of Al-2% Li-3% Cu alloys. *CORROSION*, 50(2):120–130, 1994.

[21] N Eswara Prasad, AA Gokhale och P Rama Rao. Mechanical behaviour of aluminium-lithium alloys. *Sadhana*, 28(1-2):209–246, 2003.

[22] B Noble och GE Thompson. $T_1(Al_2CuLi)$ precipitation in aluminium–copper–lithium alloys. *Metal Science Journal*, 6(1):167–174, 1972.

[23] Uyime Donatus, Maysa Terada, Carlos Ramirez Ospina, Fernanda Martins Queiroz, Aline Fatima Santos Bugarin och Isolda Costa. On the AA2198-T851 alloy microstructure and its correlation with localized corrosion behaviour. *Corrosion Science*, 131:300 – 309, 2018.

[24] Y. Ma, X. Zhou, Y. Liao, Y. Yi, H. Wu, Z. Wang och W. Huang. Localised corrosion in AA2099-T83 aluminium-lithium alloy: The role of grain orientation. *Corrosion Science*, 107:41 – 48, 2016.

[25] J.A. Moreto, C.E.B. Marino, W.W. Bose Filho, L.A. Rocha och J.C.S. Fernandes. SVET, SKP and EIS study of the corrosion behaviour of high strength Al and Al–Li alloys used in aircraft fabrication. *Corrosion Science*, 84:30 – 41, 2014.

[26] N Birbilis och RG Buchheit. Electrochemical characteristics of intermetallic phases in aluminum alloys an experimental survey and discussion. *Journal of The Electrochemical Society*, 152(4):B140–B151, 2005.

[27] Rajiv S Mishra och ZY Ma. Friction stir welding and processing. *Materials science and engineering: R: reports*, 50(1-2):1–78, 2005.

[28] Vincent Proton, Joël Alexis, Eric Andrieu, Christine Blanc, Jérôme Delfosse, Loïc Lacroix och Grégory Odemer. Influence of post-welding heat treatment on the corrosion behavior of a 2050-T3 aluminum-copper-lithium alloy friction stir welding joint. *Journal of The Electrochemical Society*, 158(5):C139–C147, 2011.

[29] Manthana Jariyaboon, AJ Davenport, Rajan Ambat, BJ Connolly, SW Williams och DA Price. The effect of welding parameters on the corrosion behaviour of friction stir welded AA2024–T351. *Corrosion Science*, 49(2):877–909, 2007.

[30] Y. Ma, X. Zhou, W. Huang, G.E. Thompson, X. Zhang, C. Luo och Z. Sun. Localized corrosion in AA2099-T83 aluminum–lithium alloy: The role of intermetallic particles. *Materials Chemistry and Physics*, 161:201 – 210, 2015.

[31] Stephen Cater, redaktör. *Fundamentals of Friction Stir Welding - 3rd Edition*, band 3rd Edition. TWI, 2016.

[32] Ch Venkata Rao, G. Madhusudhan Reddy och K. Srinivasa Rao. Microstructure and pitting corrosion resistance of AA2219 Al–Cu alloy friction stir welds – effect of tool profile. *Defence Technology*, 11(2):123 – 131, 2015.

[33] Aluminum Association m.fl. International alloy designations and chemical composition limits for wrought aluminum and wrought aluminum alloys. *Teal Sheets*, ss 1–28, 2009.

[34] Weijiu Huang, Yanlong Ma, Xiaorong Zhou, Xiaomin Meng, Yi Liao, Linjiang Chai, Yanan Yi och Xinxin Zhang. Correlation between localized plastic deformation and localized corrosion in AA2099 aluminum-lithium alloy. *Surface and Interface Analysis*, 48(8):838–842, 2016.

[35] Yakun Zhu och GS Frankel. Effect of major intermetallic particles on localized corrosion of AA2060-T8. *Corrosion*, 75(1):29–41, 2019.

[36] Ali Abd El-Aty, Yong Xu, Xunzhong Guo, Shi-Hong Zhang, Yan Ma och Dayong Chen. Strengthening mechanisms, deformation behavior, and anisotropic mechanical properties of Al-Li alloys: A review. *Journal of advanced research*, 10:49–67, 2018.

[37] JA DeRose, T Suter, A Bałkowiec, J Michalski, KJ Kurzydlowski och P Schmutz. Localised corrosion initiation and microstructural characterisation of an Al 2024 alloy with a higher Cu to Mg ratio. *Corrosion Science*, 55:313–325, 2012.

[38] N Birbilis och RG Buchheit. Electrochemical characteristics of intermetallic phases in aluminum alloys an experimental survey and discussion. *Journal of The Electrochemical Society*, 152(4):B140–B151, 2005.

[39] Y. Ma, X. Zhou, G.E. Thompson, T. Hashimoto, P. Thomson och M. Fowles. Distribution of intermetallics in an AA2099-T8 aluminium alloy extrusion. *Materials Chemistry and Physics*, 126(1):46 – 53, 2011.

[40] PEPM Campestrini, EPM Van Westing, HW Van Rooijen och JHW De Wit. Relation between microstructural aspects of AA2024 and its corrosion behaviour investigated using AFM scanning potential technique. *Corrosion Science*, 42(11):1853–1861, 2000.

[41] IJ Polmear. Light alloys 3rd ed. *Metallurgy of the Light Metals,(Edward Arnold, London, 1995) pp*, ss 231–232, 1995.

[42] Yi Lin, Ziqiao Zheng, Shichen Li, Xiang Kong och Ye Han. Microstructures and properties of 2099 Al-Li alloy. *Materials Characterization*, 84:88–99, 2013.

[43] WN Garrard. Corrosion behavior of aluminum-lithium alloys. *Corrosion*, 50(3):215–225, 1994.

[44] S Ya Betsofen, VV Antipov, IA Grushin, MI Knyazev, LB Khokhlatova och AA Alekseev. Effect of the composition of Al-Li alloys on the quantitative relation between the $\delta'(Al_3Li)$, $S_1(Al_2MgLi)$, and $T_1(Al_2CuLi)$ phases. *Russian Metallurgy (Metally)*, 2015(1):51–58, 2015.

[45] J.F. Li, C.X. Li, Z.W. Peng, W.J. Chen och Z.Q. Zheng. Corrosion mechanism associated with T1 and T2 precipitates of Al–Cu–Li alloys in NaCl solution. *Journal of Alloys and Compounds*, 460(1):688 – 693, 2008.

[46] C Kumai, J Kusinski, G Thomas och TM Devine. Influence of aging at 200 C on the corrosion resistance of Al-Li and Al-Li-Cu alloys. *Corrosion*, 45(4):294–302, 1989.

[47] JG Rinker, M Marek och TH Sanders Jr. Aluminum-lithium alloys ii. *Met. Soc. AIME*, 597, 1984.

[48] JG Brunner, N Birbilis, KD Ralston och S Virtanen. Impact of ultrafine-grained microstructure on the corrosion of aluminium alloy AA2024. *Corrosion Science*, 57:209–214, 2012.

[49] KD Ralston, N Birbilis och CHJ Davies. Revealing the relationship between grain size and corrosion rate of metals. *Scripta Materialia*, 63(12):1201–1204, 2010.

[50] Vincent Proton, Joël Alexis, Eric Andrieu, Jérôme Delfosse, Marie-Christine Lafont och Christine Blanc. Characterisation and understanding of the corrosion behaviour of the nugget in a 2050 aluminium alloy friction stir welding joint. *Corrosion Science*, 73:130 – 142, 2013.

[51] Mohiedin Bagheri Hariri, Sajad Gholami Shiri, Yadollah Yaghoubinezhad och Masoud Mohammadi Rahvard. The optimum combination of tool rotation rate and traveling speed for obtaining the preferable corrosion behavior and mechanical properties of friction stir welded AA5052 aluminum alloy. *Materials & Design*, 50:620–634, 2013.

[52] WB Lee, YM Yeon och SB Jung. The improvement of mechanical properties of friction-stir-welded A356 Al alloy. *Materials Science & Engineering A*, 355(1-2):154–159, 2003.

[53] N Akhtar, HJ Jin, F Jia och SJ Wu. Fatigue crack growth rates in friction stir welding joints of Al-Li 2060-T8X alloy. I: *2015 12th International Bhurban Conference on Applied Sciences and Technology (IBCAST)*, ss 6–13. IEEE, 2015.

[54] P. Cavaliere, M. Cabibbo, F. Panella och A. Squillace. 2198 Al–Li plates joined by friction stir welding: Mechanical and microstructural behavior. *Materials & Design*, 30(9):3622 – 3631, 2009.

[55] Pengliang Niu, Wenya Li, Zhihan Zhang och Xiawei Yang. Global and local constitutive behaviors of friction stir welded AA2024 joints. *Journal of Materials Science & Technology*, 33(9):987 – 990, 2017.

[56] Yan-hua Zhao, San-bao Lin, Lin Wu och Fu-xing Qu. The influence of pin geometry on bonding and mechanical properties in friction stir weld 2014 Al alloy. *Materials letters*, 59(23):2948–2952, 2005.

[57] Emilie Bousquet, Angéline Poulon-Quintin, Monique Puiggali, Olivier Devos och Marie Touzet. Relationship between microstructure, microhardness and corrosion sensitivity of an AA2024-T3 friction stir welded joint. *Corrosion Science*, 53(9):3026–3034, 2011.

[58] A Karanika, N Vourdas, A Makrikostas, R Marini, Th Plagianakos och S Kalogeropoulos. Development of new environmentally friendly anticorrosive surface treatments for new Al-Li alloys protection within the frame of Clean Sky2. *Procedia Structural Integrity*, 10:66–72, 2018.

[59] Anjam Khursheed. *Scanning electron microscope optics and spectrometers*. World scientific, 2011.

[60] Yakun Zhu, Kai Sun, Jacob Garves, Leslie G Bland, Jenifer Locke, John Allison och GS Frankel. Micro-and nano-scale intermetallic phases in AA2070-T8 and their corrosion behavior. *Electrochimica Acta*, 319:634–648, 2019.

[61] Lei Yao, Jianhua Liu, Songmei Li och Mei Yu. Effects of prior cathodic polarization on crystallographic pit initiation on aluminum. *Corrosion science*, 80:12–18, 2014.

[62] James Sullivan, Shahin Mehraban och Jon Elvins. In situ monitoring of the microstructural corrosion mechanisms of zinc–magnesium–aluminium alloys using time lapse microscopy. *Corrosion Science*, 53(6):2208–2215, 2011.

[63] B Łosiewicz, Magdalena Popczyk, Magdalena Szklarska, Agnieszka Smołka, Patrycja Osak och A Budniok. Application of the scanning kelvin probe technique for characterization of corrosion interfaces. I: *Solid State Phenomena*, band 228, ss 369–382. Trans Tech Publ, 2015.

[64] Xiao-rong ZHOU, Xiao-min MENG, Wei-jiu HUANG, LIAO Yi, Xiao-li CHEN, Ya-nan YI, Xin-xin ZHANG, GE THOMPSON m.fl. Influence of thermomechanical treatments on localized corrosion susceptibility and propagation mechanism of AA2099 Al–Li alloy. *Transactions of Nonferrous Metals Society of China*, 26(6):1472–1481, 2016.

[65] Jiangwei Sun, Liang Zhang, Guohua Wu, Xiaolong Zhang, Mian Rong och Cunlong Wang. Microstructural characteristics and mechanical properties of extruded Al-4Cu-1Li-0.4 Mg-0.1 Zr-xZn alloy. *Materials Science and Engineering: A*, 743:223–232, 2019.

[66] Lixin Zhang, Yihan Wang, Xiaohui Yang, Kai Li, Song Ni, Yong Du och Min Song. Texture, microstructure and mechanical properties of 6111 aluminum alloy subject to rolling deformation. *Materials Research*, 20(5):1360–1368, 2017.

[67] WANG Bo, Xian-hua Chen, Fu-sheng Pan, Jian-jun Mao och FANG Yong. Effects of cold rolling and heat treatment on microstructure and mechanical properties of AA5052 aluminum alloy. *Transactions of Nonferrous Metals Society of China*, 25(8):2481–2489, 2015.

[68] J Gilbert Kaufman. *Introduction to aluminum alloys and tempers*. ASM international, 2000.

[69] Vincent Proton, Joël Alexis, Eric Andrieu, Jérôme Delfosse, Alexis Deschamps, Frédéric De Geuser, Marie-Christine Lafont och Christine Blanc. The influence of artificial ageing on the corrosion behaviour of a 2050 aluminium–copper–lithium alloy. *Corrosion Science*, 80:494–502, 2014.

[70] AR Cisko, JB Jordon, DZ Avery, ZB McClelland, T Liu, TW Rushing, LN Brewer, PG Allison och L Garcia. Characterization of fatigue behavior of Al-Li alloy 2099. *Materials Characterization*, 151:496–505, 2019.

[71] Xiangchen Meng, Zheng Xu, Yongxian Huang, Yuming Xie, Yaobin Wang, Long Wan, Zongliang Lv och Jian Cao. Interface characteristic and tensile property of friction stir lap welding of dissimilar aircraft 2060-T8 and 2099-T83 Al–Li alloys. *The International Journal of Advanced Manufacturing Technology*, 94(1-4):1253–1261, 2018.

[72] Katsuhiko Urushino och Katsuhisa Sugimoto. Stress-corrosion cracking of aged al□ cu□ mg alloys in nacl solution. *Corrosion Science*, 19(4):225–236, 1979.

[73] N Wint, ZS Barrett, G Williams och HN McMurray. The study of AA2024 de-alloying using luminol electrogenerated chemiluminescence imaging. *Journal of The Electrochemical Society*, 166(11):C3417–C3430, 2019.

[74] Jannik Entringer, Martina Meisnar, Martin Reimann, Carsten Blawert, Mikhail Zheludkevich och Jorge F dos Santos. The effect of grain boundary precipitates on stress corrosion cracking in a bobbin tool friction stir welded Al-Cu-Li alloy. *Materials Letters: X*, 2:100014, 2019.

[75] ML Zheludkevich, I Miranda Salvado och MGS Ferreira. Sol–gel coatings for corrosion protection of metals. *Journal of Materials Chemistry*, 15(48):5099–5111, 2005.

[76] Uyime Donatus, George E Thompson och Xiaorong Zhou. Anodizing behavior of friction stir welded dissimilar aluminum alloys. *Journal of The Electrochemical Society*, 162(12):C657–C665, 2015.

[77] Pedro Atz Dick, Gerhard H Knörnschild och Luís FP Dick. Anodising and corrosion resistance of aa 7050 friction stir welds. *Corrosion Science*, 114:28–36, 2017.

[78] XF Yang, DE Tallman, VJ Gelling, GP Bierwagen, LS Kasten och J Berg. Use of a sol–gel conversion coating for aluminum corrosion protection. *Surface and Coatings Technology*, 140(1):44–50, 2001.